8-2014

ELECTROSTATIC AND ELECTRICAL TRANSPORT ANALYSIS OF NANOMATERIALS AND NUMERICAL METHODS DEVELOPMENT

Hua Li
Clemson University, hual@clemson.edu

ELECTROSTATIC AND ELECTRICAL TRANSPORT ANALYSIS OF NANOMATERIALS AND NUMERICAL METHODS DEVELOPMENT

A Thesis
Presented to
the Graduate School of
Clemson University

In Partial Fulfillment
of the Requirements for the Degree
Doctor of Philosophy
Mechanical Engineering

---

by
Hua Li
August 2014

Accepted by
Dr. Gang Li, Committee Chair
Dr. Lonny Thompson
Dr. Mohammed Daqaq
Dr. Pingshan Wang
Dr. Jian He

ABSTRACT

The nanotechnology today is continuously boosting the application of nanostructured materials in the development and innovation of electronic devices, such as Nano-Electromechanical Systems (NEMS), electrical transistors, thermoelectric devices, and solar cells. Due to the size miniaturization, quantum mechanical effects play important roles in the performance of such devices. To correctly capture the quantum mechanical effects and understand how these effects influence the electrostatic and electrical transport properties of nanomaterials, efficient and accurate computational models are highly desirable. Currently, the commonly used model for electrostatic analysis of nanoscale devices is based on self-consistent solution of the effective-mass Schrödinger equation coupled with the Poisson equation. However, a major drawback of this model is its inefficiency to simulate systems with large Degrees of Freedom (DOFs). To reduce the computational cost, in this thesis, two Component Mode Synthesis (CMS) approaches, namely the fixed-interface CMS and the free-interface CMS, are incorporated into the Schrödinger-Poisson model to speed up the electrostatic analysis in nanostructures. The new model is employed to analyze the quantum electrostatics in both nanowires and FinFETs. Numerical results demonstrate the superior computational performance in terms of efficiency and accuracy.

In addition to the electrostatic analysis, carrier transport in nanostructures

with perturbation from quantum effects also merits careful consideration. Among the computational models developed for quantum mechanical carrier transport analysis, the Non-Equilibrium Green's Function (NEGF) coupled with Poisson equation has gained vast application in both ballistic and diffusive transport analysis of nanodevices. In this thesis, the NEGF model is expanded to include mechanical strain and carrier scattering effects. Two important multiphysics systems are investigated in this work. We first study the effect of mechanical strain on the electrical conductivity of $Si/Si_{1-x}Ge_x$ nanocomposite thin films. The strain effect on the bandstructures of nano-thin films is modeled by a degenerate two-band $k \cdot p$ theory. The strain induced bandstructure variation is then incorporated in the NEGF-Poisson model. The results introduce new perspectives on electrical transport in strained nano-thin films, which provides useful guidance in the design of flexible electronics. Secondly, nanoporous Si as an efficient thermoelectric material is studied. The Seebeck coefficient and electrical conductivity of nanoporous Si are computed by using the NEGF-Poisson model with scatterings modeled by Büttiker probes. The phonon thermal conductivity is obtained by using a Boltzmann Transport Equation (BTE) model while the electron thermal conductivity is captured by the Wiedemann-Franz law. The thermoelectric figure of merit of nanoporous Si is computed for different doping density, porosities, temperature and pore size. An optimal combination of the material design parameters is explored and the result proves that nanoporous Si has better thermoelectric properties than its bulk counterpart.

In the electrical transport analysis of nanomaterials, we found that the standard NEGF-Poisson model using the Finite Difference (FD) method has a high computational cost, and is inapplicable to devices with irregular geometries. To overcome these difficulties, an accelerated Finite Element Contact Block Reduction

(FECBR) method is developed in this thesis. The performance of the accelerated FECBR is evaluated through the simulation of two types of electronic devices: taper-shaped DG-MOSFETs and DG-MOSFETs with Si/SiO_2 interface roughness. Numerical results show that the accelerated FECBR can be applied to model ballistic carrier transport in devices with multiple leads, arbitrary geometry and complex potential profile. The accelerated FECBR significantly improves the flexibility and efficiency of electrical transport analysis of nanomaterials and nanodevices.

ACKNOWLEDGMENTS

I would like to express my sincere gratitude to my advisor, professor Gang Li, for his invaluable advices and continuous support for my research, without his help, this thesis would not be possible. During my Ph.D study and research here at Clemson, he has been always a great mentor. The discussions with him about the research have been always helpful and enlightening. His insight on modeling and simulations brings me into this interesting and exciting area, his golden guidance and encouragement helps me build a deep understanding of this area and his strict attitude in research teaches me how to be a professional and good researcher. For me, he is not only a great advisor and teacher, he is also an outstanding research leader. I deeply acknowledge his supervision in the past few years and undoubtedly, the skills I've learned and mastered during my Ph.D are going to be beneficial in my entire career.

I would also like to extend my true appreciation to professor Lonny Thompson, professor Mohammed Daqaq, professor Pingshan Wang and professor Jian He for serving on my dissertation committee, reading my thesis and commenting on my work. Furthermore, I would like to thank my colleagues, Ying Yu and Yaoyao Xu, for their cooperation and discussions in some of the work I've finished during my Ph.D, I also want to thank other group members here at Clemson for their assistance both in my research and my life. Moreover, I want to thank my friends, Litao Liang, Jun Lan, Peng Wu, Changxue Xu, Shuaishuai Liu, Wei Li and Zhiyuan Ma, for their friendship

and making my life here happy and unforgettable. In addition, I am grateful for the financial support from CMMI and NSF.

My special acknowledgment goes to my family. I want to thank my American host family, Larry Edwards and Sarah Alice Edwards, for taking care of me here. Their kindness and generosity make me feel being at home here. Most importantly, words can not describe how grateful I am for my parents and sisters. They are always supportive and thoughtful.

TABLE OF CONTENTS

LIST OF TABLES

Table **Page**

LIST OF FIGURES

Figure **Page**

CHAPTER 1

INTRODUCTION

Due to the advancement in nanotechnology, nanomaterials have opened many new possibilities in different areas, such as Nano-Electromechanical Systems (NEMS) [1–4], electrical transistors [5, 6], flexible electronics [7, 8], thermoelectrics [9,10] and solar cells [11,12]. The unique properties of nanomaterials are as a result of quantum effects. Within nanometer regime, those quantum effects play a dominant role in shaping material properties. Many nanostructured materials have been proposed in the past few decades for different state-of-the-art devices. Compared with Micro-Electromechanical Systems (MEMS), NEMS typically integrate transistor-like nanoelectronics with mechanical actuators, pumps, or motors, and may thereby form physical, biological, and chemical sensors. The miniaturization of the systems leads to low mass, high mechanical resonance frequencies, potentially large quantum mechanical effects such as zero point motion, and a high surface-to-volume ratio useful for surface-based sensing mechanisms [13]. Those advantages are being explored massively. Silicon nanostructures [2, 3] have been applied in NEMS, such as actuators, biological and chemical sensors, moreover, the carbon nanotubes [4] are also proposed to be used in RF-NEMS. In

microelectronics industry, the development of the Complimentary Metal-Oxide-Semiconductor (CMOS) device scaling [14, 15] in the past few decades has led to the limit of the Moore's law [16], which states that the transistor density on a single microprocessor doubles every three years. Such device scaling causes contemporary electronic devices to enter into nanometer regime. At nanoscale, device performance becomes increasingly complicated as new physical phenomena at short dimensions comes into play, and material properties are close to their limits. Different approaches have been proposed to improve the device performance to overcome the the current difficulties. Among them, nanomaterials and nanostructures have attracted much attention. New nano-structures such as FinFETs [5] and nanowires [6] have been developed and investigated concretely in terms of their operational performance. Meanwhile, new alternative channel materials have been explored, such as Ge-thin film [17], carbon nanotubes [18] and so on. Another important application of nanomaterials is thermoelectric energy conversion. Thermoelectric materials have the ability to directly convert heat energy into electricity. More importantly, they have the advantages of being clean, economical and sustainable. They have great potentials to be used in power generation, cooling systems and waste heat recovery [19–21]. However, the current difficulty in massive application of thermoelectric materials lies in their relatively low conversion efficiency [22, 23]. To overcome the difficulty, a significant increase of their efficiency is required. The efficiency of thermoelectric materials is evaluated by the dimensionless figure of merit $ZT = S^2\sigma T/k$, where σ is the electrical conductivity, S is the Seebeck coefficient, k is the thermal conductivity contributed from both electrons and phonons, and T is the temperature. The product of $S^2\sigma$ is called the power factor. To increase ZT, thermoelectric materials with lower and higher power factor are preferred. One of the key challenges to increase ZT is that

optimizing one parameter in ZT often causes sacrifice of another. Many approaches have been proposed to increase in ZT. Quantum well and quantum dot superlattice structures which are poor thermal conductors due to quantum effects are proposed and investigated. Bi_2Te_3/Sb_2Te_2 [24] thin film superlattices show a high ZT up to 2 and the ZT of embedded $PbSeTe$ quantum dots [25] has been reported to be larger than 1. The obstacles of massive application of those thermoelectric materials are their limited resources and expensive fabrication process. One-dimensional nanowire structures are also considered. It's indicated that Si nanowires [10] and Bi nanowires [26] have great thermoelectric capabilities. Si nanowires with diameter ranging from $10nm$ to $20nm$ show a high ZT up to 1.0. The increase of ZT in nanowires is also due to the large reduction in their thermal conductivity, which could be as a result of surface roughness and phonon drag effect. Meanwhile, carbon nanotubes [27] and carbon nanoribbons [28] are explored to improve thermoelectric performance. From manufacturing perspective, the fabrication process of those newly emerged nano-structures becomes much more complicated and time-consuming [29], consequently, the performance optimization cannot merely depend on the experimental trial-and-error approaches. To better understand the properties of those contemporary devices, computational simulations can be used as an economical and efficient tool to provide a fundamental understanding of the physics involved in those structures before engaging in experiments. The massive application of nano-structures in different fields requires an accurate and efficient understanding of the material properties, including mechanical, thermal, electrical properties, etc. The conventional simulations of electrostatic and electrical properties are based on classical or semiclassical models, in which the charge carriers are treated as semiclassical particles. With contemporary nanoscale structures, those models lose their validity due to their incapability to accurately describe the

quantum effect which is pronounced in those structures. To properly capture those effects, quantum-based simulation models are required. Below is a short summary of the current models which are widely used and some of their limitations.

1. To model the electrostatics in nano-structures, the Poisson equation needs to be solved. The Poisson equation describes the space charge effect on the electrostatics in the systems. To obtain the charge distribution in the domain of simulation interest, proper models have to be chosen at different length scales, when it comes to nanoscale structures, the effective-mass Schrödinger equation with closed boundary condition coupled with Poisson has been widely adopted [30–32] to simulate the electrostatics. It can be used for quantum mechanical electrostatic analysis of nano-structures such as quantum well, quantum dots, nanoelectromechanical systems (NEMS), etc. The model is attractive due to its simplicity and straightforward implementation by using standard Finite Difference Method (FDM) or Finite Element Method (FEM). However, as it is required to solve a generalized eigenvalue problem generated from the discretization of the Schrödinger equation with closed boundary conditions, the computational cost of the analysis increases quickly when the system's degrees of freedom (DOFs) increases. Furthermore, the newly emerged MOSFETs with multiple gates [30, 33], such as Trigates, FinFETs and Pi-gates, imply that multi-dimensional analysis is necessary to gain a full understanding of the electronic properties in those devices. To deal with simulations with large number of DOFs, current numerical methods become inefficient. For this reason, techniques that enable efficient solution of discretized Schrödinger equations in multidimensional domains with large DOFs are desirable.

2. The electrical transport analysis in nanostructures can provide the electrical properties of those structures, such as charge distribution, potential profiles, current density, etc. The development of nanostructured materials, such as particulate, layered and fibrous nanocomposites, has opened the possibilities of tailoring material electrical properties in a controlled manner [34, 35], for example, nanocomposite thin-films have been fabricated to produce high-mobility MOS thin-film transistors (TFT) for displays, active RF tags and thin-film sensors [36], moreover, nanowires have been proposed to be an efficient thermoelectric alternatives in the future. The current modeling and analysis of electrical transport properties has been mainly based on the Boltzmann Transport Equation (BTE) under the relaxation-time approximation [37–39], the model is not accurate within nano-scale. To solve for carrier transport in the nano-structures, the electrostatics has to be solved self-consistently with governing equations which describe the carrier flow due to all sources of driving forces. One of the well-developed formalism to calculate the carrier transport in a nanoscale structure is Landauer-Büttiker formalism [40, 41], which calculates the current flow by transmission function. The transmission function in the nanostructures can be obtained by solving Schrödinger equation directly [42] or by using non-equilibrium Green's function (NEGF). A well-developed approach to solve the Schrödinger equation directly is the transfer matrix method [43], which proves to be unstable when the DOFs in a system becomes large. To overcome the limitation, the Quantum Transmitting Boundary Method (QTBM) [42, 44] has been developed. The implementation of this approach involves repeated solutions of a linear system of equations whose size is proportional to the DOFs in the entire simulation domain. It's been used to simulate ballistic

transport in electronic systems from $1D$ [45] to $3D$ [46]. Instead of directly solving for the electron eigenstates within the device through Schrödinger equation, NEGF [47], within which a self-energy function has been introduced to denote the interaction between the active device region and the large carrier reservoirs, is also widely adopted. Its capability to account for different scattering scenarios in the electron transport within different systems largely favors its popularity. The scatterings are usually denoted by the Büttiker probes model [48], more accurate treatment can be also derived rigorously in NEGF formalism [49]. However, the computational cost caused by directly inverting a matrix repeatedly whose size resting on the number of mesh grids in the simulation domain impedes its application in 2D and 3D simulations. Once the DOFs increases high enough, the computation cost becomes intractable with a single PC, under this circumstance, parallel computing is required to solve for the direct Green's function [50]. Meanwhile, to ease the computational burden, instead of inverting the matrix directly, recursive Green's function method [51] and mode-space Green's function method [52] have been developed. The former has been used to $2D$ devices [53] and nanowires [6], the latter has been incorporated in the simulator NanoMOS [52]. However, the recursive Green's function is limited to be used in the device simulations with no more than two ohmic contacts since it relies on the tri-diagonality of system Hamiltonian. The mode-space Green's function method is only applicable when the device domain is of high symmetry where the Schrödinger equation is separable in different directions. To deal with the foregoing limitations, a new approach which is named Contact Block Reduction (CBR) [29, 54] has been developed to simulate ballistic transport in nanoscale devices with any geometry, potential profile

and the number of leads. By using the CBR, the Green's function can be obtained by a one-time solution of the eigen-pairs for a closed system (the entire simulation domain without perturbations from external sources) and repeated inversion of a small matrix of size dependent on the DOFs along the boundaries connecting the active domain to the carrier reservoirs. Unfortunately, the current available numerical algorithm for implementing this approach is limited to FDM. To deal with irregular geometries, FEM serves as a better and proper approach which allows for non-uniform mesh of the device domain. However, finite element formulation for CBR is currently not available. Whether this model could remain its efficiency with FEM is not clear. In addition, when the number of DOFs involved in the device simulation increases, the computational time consumed by solving for the electron eigenstates is increased significantly, therefore, more efficient algorithm to solve for the eigenstates is needed to maintain its feasibility to accurately and efficiently model the ballistic transport in 2D and 3D electronic devices.

To address these issues, the objectives of this research are: 1) to develop a new efficient TCAD (technology computer aided design) model for quantum mechanical electrostatic analysis in nano-structures which can deal with systems with large DOFs. 2) to numerically investigate the electrical transport properties of newly proposed nanostructures, such as nanocomposite thin films, nanoscale thermoelectric materials, etc. 3) to develop a new efficient finite element formalism model for quantum transport analysis which enables efficient simulations of 2D and 3D simulations of modern nano-structures and nanodevices with rational accuracy. The research work can be summarized into the following four parts.

1. Development of a robust and efficient model to simulate the electrostatics in

the nanoscale structures. In this part, we propose a component mode synthesis (CMS) approach to accelerate the numerical solution of the Schrödinger equations. As a model order reduction method, the CMS was originally developed for dynamic analysis of large mechanical systems. Here the CMS approaches are extended in the quantum mechanical electrostatic analysis. In CMS, the whole simulation domain is divided into a set of small components, in each component, an eigenvalue problem of size equal to the DOFs in the local component (much smaller than the total DOFs) is solved to obtain the eigen-pairs in it. A small set of component eigen-pairs is retained along with some other modes (either constraint modes or attachment/rigid body modes) to construct the Ritz basis vectors which could be used to approximate the wavefunctions in each component. By assembling those vectors from all the components, a global transformation matrix composed of a complete and orthogonal basis could be obtained and the Hamiltonian could be projected into this vector space, usually, the size of Hamiltonian could be largely reduced and approximate results for global eigen-pairs could be solved. The two most commonly used CMS approaches are the fixed-interface CMS and the free-interface CMS. While the former composes Ritz basis vector by using fixed interface wave functions and constraint modes, the latter makes use of free interface wave functions, attachment modes and rigid body modes. The performance of both approaches is illustrated to solve for the electrostatics in different electronic devices.

2. Computational modeling and computational analysis of strain effect on electronic properties of devices and materials. Crystal strains and external applied strains can induce band structure changes in semiconductor materials.

The band structure variation is commonly composed of band splitting and band wrapping [55, 56]. Band splitting may cause electron redistribution in the band valleys while band warping can result in conductivity effective mass change. Strain can be also used to tailor the band offsets between different semiconductor materials. In this part, we propose a modeling approach for investigating the effects of mechanical strain on electrical conductivity of semiconductor nanocomposite thin films, and analyze the effect of uniaxial and biaxial strains on the electrical conductivity of $Si/Si_{1-x}Ge_x$ nanocomposite thin films with $Si_{1-x}Ge_x$ nanowires embedded in Si host. We utilize a degenerate two-band $k \cdot p$ theory to calculate the variation of the electronic band structures in deformed crystal lattices of Si and $Si_{1-x}Ge_x$. To calculate the electrical conductivity, we adopt a real-space NEGF for the analysis of electron transport in the nanocomposite thin films. The NEGF can reliably capture the quantum effect which may play a key role in the performance of these nanoscale systems. In addition, by coupling with the Poisson equation, the space charge effect can be properly considered. In this part, by solving the NEGF and Poisson equations self-consistently, we explicitly calculate the energy band profile, electron density and current density within the nanocomposite material. The IV curve can then be obtained by applying different voltages across the material. Finally, the electrical conductance of the material can be calculated from the slope of the IV curve when the applied voltage is small. By including the strain-induced band structure change in the NEGF, a set of IV curves under different strains are calculated. The electrical conductance of the nanocomposite material as a function of the applied strains is computed from these IV curves.

3. Computational analysis of electrical transport in nanoporous thermoelectric materials. Nano-porous Si [57] has been proposed to be an efficient thermoelectric material ever since it is found to have very low thermal conductivity. To analyze and better understand the thermoelectric properties of nanoporous Si, in this part, a numerical model combining (NEGF) and Poisson equations and phonon Boltzmann Transport Equation (BTE) is used. To our knowledge, this is the first time that a numerical model is proposed and applied to investigate the thermoelectric performance of nanoporous Si. The NEGF-Poisson model is solved self-consistently with FDM to numerically calculate the electrical conductivity and Seebeck coefficient of the material while the phonon BTE is solved by Finite Volume Method (FVM) to obtain its phononic thermal conductivity. Meanwhile, the electronic thermal conductivity is well considered by the Wiedemann-Franz Law [58]. The numerical procedures of the computation for the electrical conductivity and Seebeck coefficient mimic experiments. The scattering in the material is modeled by Büttiker probes. The electronic thermal conductivity is obtained with a simple relation to the electrical conductivity of the material through Wiedemann-Franz Law. Finally, after the electrical conductivity, the Seebeck coefficient and the thermal conductivity are obtained, the figure of merit is easily obtained. By using the model, the effect of porosity, the size of unit cell, the temperature and the doping density on the thermoelectric properties of nanoporous silicon is investigated. To optimize the thermoelectric efficiency of nanoporous silicon, the best combination of those parameters is also studied.

4. Finite element formulation and efficient numerical analysis of ballistic quantum transport in contemporary electronic nanostructures with efficiency

and accuracy. As discussed, the mostly common used model, i.e., NEGF-Poisson is inefficient when it comes to electronic devices of more than two leads and arbitrary potentials. Moreover, although the CBR-Poisson model seems to be able to handle those limitations, current FDM implementation cannot be used when the electronic devices have irregular geometries. As a result, in this part, we develop a Finite Element Contact Block Reduction (FECBR)-Poisson model and test its performance by using different devices with irregular geometries. The percentage of kept eigenstates to ensure the accuracy of the final results is investigated and the computational efficiency of the model is ensured. Furthermore, since the computation of the CBR-Poisson model is dependent on the eigenstates obtained by solving the Schödinger equation with closed boundary conditions, when the number of DOFs in the device gets large, the available solver becomes very inefficient, consequently, we incorporate the CMS approaches into CBR-Poisson model to resolve this issue. Simulations for devices with large DOFSs are implemented with the new model, which make it possible to simulate large 2D and 3D electronic devices with the least computational resource.

The rest of this thesis is arranged as follows, in Chapter 2, CMS approaches for quantum mechanical electrostatic analysis of nanoscale devices have been developed. The results showed that the CMS can produce a large computational cost saving. The work of developing numerical models to simulate the effect of strains on the nanocomposite thin films has been presented in Chapter 3. With the numerical analysis, the strain proves to be a very useful technique to tune electrical properties of nanocomposite thin films. In Chapter 4, the thermoelectric properties

of nanoporous Si is investigated with a newly proposed numerical method, the results demonstrated that the nanoporous Si could be considered as an efficient thermoelectric materials. With the understanding and development of methods used in computational electronics within quantum regime, we proposed a new accelerated model, namely, the accelerated Finite Element Contact Block Reduction (FECBR) approach, to facilitate the modeling and simulations of ballistic transport in devices and materials in Chapter 5, finally, the conclusions are shown in Chapter 6.

CHAPTER 2

COMPONENT MODE SYNTHESIS APPROACHES FOR QUANTUM MECHANICAL ELECTROSTATIC ANALYSIS OF NANOSCALE DEVICES

2.1 Introduction

As the dimensions of commonly used semiconductor devices have shrunk into nanometer regime [59–62], it is recognized that the influence of quantum effects on their electrical properties cannot be ignored [63–66]. Various computational models and approaches [2, 3, 5, 30–32, 47, 52, 67, 68] have been developed to analyze these properties including the quantum effects in nanostructures and devices in the past few decades. Among these computational models, the Schrödinger-Poisson

model [2, 5, 30–32] has been widely adopted for quantum mechanical electrostatic analysis of nanostructures and devices such as quantum wires, MOSFETs and nanoelectromechanical systems (NEMS). The numerical results allow for evaluations of the electrical properties such as charge concentration and potential profile in these structures. The emerge of MOSFETs with multiple gates, such as Trigates, FinFETs and Pi-gates, offers a superior electrostatic control of devices by the gates, which can be therefore used to reduce the short channel effects within those devices. A full $2D$ electrostatic analysis [69, 70] in the cross-section perpendicular to the transport direction in those nanodevices can be used to better understand the scalability of devices, moreover, many simulations and studies [33, 71–75] focusing on the corner effects, the properties of inversion layers, current oscillations due to the applied gate voltages, and threshold voltages of multiple-gate MOSFETs have been carried out by applying the Schrödinger-Poisson model. This model is also used in the quantum simulation of silicon nanowire transistors by NEGF recently [6], an application of this model to obtain the electron sub-bands and wave functions in the devices is necessary to analyze transport characteristics of the transistors. It is reported [76, 77] that solving Schrödinger equation to obtain the electron sub-bands and wave functions within the cross-section perpendicular to the transport direction consumes most of the CPU time in the whole simulation. The Schrödinger-Poisson model is attractive due to its simplicity and straightforward implementation by using standard finite difference or finite element methods. However, as it is required to solve a generalized eigenvalue problem generated from the discretization of the Schrödinger equation, the computational cost of the analysis increases quickly when the system's degrees of freedom (DOFs) increase. For this reason, techniques that enable an efficient solution of discretized Schrödinger equation in multidimensional domains are desirable. In this chapter, we seek to accelerate the numerical solution

of the Schrödinger equation by using component mode synthesis (CMS) approaches [77–88]. As a model order reduction method, the CMS was originally developed for dynamic analysis of large mechanical systems. In the mechanical analysis using CMS approaches, a large structure is discretized into substructures or components. The component vibrational modes are computed for each substructure. Only a small set of component modes are retained to construct a set of Ritz basis vectors [85]. The basis vectors are used to approximate the displacement of the substructure. The approximations of the substructures are then assembled to obtain a global approximation of the entire structure's displacement. In this chapter, the CMS approaches are extended in the quantum mechanical electrostatic analysis where a set of basis vectors are constructed to approximate the wave functions in each component. The global energy levels and wave functions are then recovered by the synthesis of these component wave functions. Different from mechanical analysis where only a few vibrational modes are sufficient to model the dynamic response, in some cases, it is necessary to calculate many energy levels and wave functions in order to compute the charge concentrations accurately. In our analysis, it is observed that the construction of the basis vectors plays a critical role in the accuracy of the final results. We investigate the performance of two CMS approaches with different ways of constructing basis vectors, namely, the fixed interface CMS approach and the free interface CMS approach. The fixed interface CMS approach computes fixed interface wave functions and constraint modes [38] to form the basis vectors while the free interface CMS approach employs a set of free interface wave functions, attachment modes and rigid body modes [85, 86] to form the basis vectors. The two CMS approaches are applied to compute the charge concentrations and potential profiles of several $2D$ semiconductor devices including quantum wire, and multiple-gate MOSFETs. It is shown that both approaches greatly reduce the

computational cost while the free interface CMS approach gives significantly more accurate results of the energy levels and wave functions. However, when large degrees of freedom are included in the simulation, the fixed interface CMS approach is more efficient than the free interface CMS approach. The rest of the chapter is organized as follows. First of all, the self-consistent numerical solution of Schrödinger-Poisson equations is described in Section 2.2, then the CMS approaches for solving the Schrödinger equation are presented in Section 2.3 and numerical examples are presented in Section 2.4, finally, a summary is shown in Section 2.5.

2.2 Quantum Mechanical Electrostatic Analysis

2.2.1 Governing equations of the Schrödinger-Poisson model

In the $2D$ quantum mechanical electrostatic analysis using Schrödinger-Poisson model, the two dimensional effective mass Schrödinger equation is given by [69],

$$\mathbf{H}\psi_n = -\frac{\hbar^2}{2m_x^*}\frac{\partial^2\psi_n}{\partial x^2} - \frac{\hbar^2}{2m_y^*}\frac{\partial^2\psi_n}{\partial y^2} + U\psi_n + \Delta E\psi_n = E_n\psi_n \tag{2.1}$$

where H is the Hamiltonian, U is the potential energy, and m_x^* and m_y^* are the effective masses of electrons or holes in x and y directions, respectively, ψ_n is the wave function corresponding to the energy level E_n , and ΔE is the pseudo-potential energy due to the band offset at the heterostructure interface. By solving the Schrödinger equation, Eq. (2.1), the energy levels E_n and the corresponding wave functions ψ_n can be obtained for electrons and holes. The Schrödinger equation is coupled with

the Poisson equation through the quantum electron and hole concentrations,

$$n = \frac{N_{nd}}{\pi}\left(\frac{2m^*_{nz}k_BT}{\hbar^2}\right)^{1/2} \times \sum_{n=1}^{\infty}\psi_n^2 F_{-1/2}\left(\frac{E_F - E_n}{k_BT}\right) \tag{2.2}$$

$$p = \frac{N_{pd}}{\pi}\left(\frac{2m^*_{pz}k_BT}{\hbar^2}\right)^{1/2} \times \sum_{n=1}^{\infty}\psi_n^2 F_{-1/2}\left(\frac{E_n - E_F}{k_BT}\right) \tag{2.3}$$

where N_{nd} and N_{pd} are the band degeneracy of electrons and holes, respectively, m^*_{nz} and m^*_{pz} are the effective masses of electrons and holes in z-direction, respectively, k_B is the Boltzmann constant, T is the temperature, E_F is the Fermi energy, and $F_{-1/2}$ is the complete Fermi-Dirac integral of order $-1/2$. The electron and hole concentrations can then be substituted into Poisson equation to obtain potential profile in semiconductor devices. The Poisson equation is expressed as,

$$\nabla \cdot [\varepsilon_r \nabla U] = e^2[-n + p + N_d^+ - N_a^-] \tag{2.4}$$

where ε_r is the dielectric constant, e is the unit electric charge, n and p are electron and hole concentrations given in Eq. (2.2) and Eq. (2.3), N_d^+ and N_a^- are ionized donor and acceptor concentrations. To obtain a self-consistent solution of the coupled Schrödinger-Poisson equations, one needs to iterate between the Schrödinger and Poisson equations. By solving the Schrödinger equation with a trial potential energy $U_{initial}$, the eigenvalues and eigenvectors are obtained. The electron and hole concentrations are then computed based on these eigen-pairs. Substituting the computed electron and hole concentrations into the Poisson equation, a new potential profile U can be calculated. The new potential profile is then used to solve the Schrödinger equation again to obtain new eigenvalues E_n and corresponding eigenvectors. By following this iteration procedure, with a number of iterations, a

final solution of charge concentration and potential profile satisfying given convergence criteria can be obtained. While this relaxation scheme is straightforward, it has been shown that its convergence property is poor [32, 69, 70]. In this chapter, instead of solving the linear Poisson equation shown in Eq. (2.4), we employ a predictor-corrector approach proposed by Trellakis, et al. [69] to obtain improved convergence. In the predictor-corrector approach, assuming an electron dominant case, $n[U]$ in the Poisson equation is replaced by a modified quantum electron concentration,

$$\nabla \cdot [\varepsilon_r \nabla U] = e^2[-\tilde{n} + p + N_d^+ - N_a^-] \tag{2.5}$$

where

$$\tilde{n} = \frac{N_{nd}}{\pi} \left(\frac{2m_{nz}^* k_B T}{\hbar^2} \right)^{1/2} \times \sum_{n=1}^{\infty} \psi_n^2 F_{-1/2} \left(\frac{E_F - E_n^k + e(U - U^k)}{k_B T} \right) \tag{2.6}$$

The superscript k denotes the quantities obtained from the previous Schrödinger-Poisson iteration. Note that the Poisson equation becomes nonlinear due to the modified quantum electron concentration.

2.2.2 Finite element solution of coupled Schrödinger-Poisson equations

The governing equations given in Eq. (2.1) and Eq. (2.5) are solved by using the Finite Element Method (FEM). The governing PDE of the Schrödinger equation can be converted to its weak form by using Galerkin weighted residual method. Multiplying both sides of Eq. (2.1) by the variation of the wave functions, $\delta\psi_n$, and

integrating the product over the $2D$ domain, we obtain,

$$\sum_i -\frac{\hbar^2}{2}\int_{\Gamma_i}\delta\psi\frac{1}{m^*_{\overrightarrow{n_i}}}\left(\nabla\psi\cdot\overrightarrow{n_i}\right)\mathrm{d}\Gamma_i+\frac{\hbar^2}{2}\int_\Omega(\nabla\delta\psi)^T\mathbf{M}^*\nabla\psi\mathrm{d}\Omega+\int_\Omega U\delta\psi\psi\mathrm{d}\Omega=E\int_\Omega\delta\psi\psi\mathrm{d}\Omega \tag{2.7}$$

where Ω is the simulation domain, $\overrightarrow{n_i}$ is the normal vector to the boundary Γ_i, $m^*_{\overrightarrow{n_i}}$ is the electron effective mass in $\overrightarrow{n_i}$ direction, $\mathbf{M}^*$ is a 2×2 diagonal matrix with $1/m^*_x$ and $1/m^*_y$ as its diagonal elements. In this chapter, the Dirichlet boundary condition $\psi_n = 0$ for the wave functions along the boundaries of the simulation domain Ω is applied. In FEM, such boundary conditions can be automatically applied by dropping the first term in Eq. (2.7). Therefore, Eq. (2.7) for closed system can be obtained as,

$$\frac{\hbar^2}{2}\int_\Omega(\nabla\delta\psi)^T\mathbf{M}^*\nabla\psi\mathrm{d}\Omega+\int_\Omega U\delta\psi\psi\mathrm{d}\Omega=E\int_\Omega\delta\psi\psi\mathrm{d}\Omega \tag{2.8}$$

After meshing the simulation domain into a series of small elements, in each element, the unknown wavefunction $\psi(x,y)$ can be expanded in the basis of $2D$ shape functions N^{2D} as,

$$\psi^e=\sum_{s=1}^{n_s}N_s^{2D}\psi_s^e=\begin{pmatrix}N_1^{2D} & N_2^{2D} & \dots & N_{n_s}^{2D}\end{pmatrix}\begin{pmatrix}\psi_1^e\\ \psi_2^e\\ \dots\\ \psi_{n_s}^e\end{pmatrix}=\mathbf{N}^{2D}\boldsymbol{\psi}^e \tag{2.9}$$

where n_s is the total number of nodes in a single element, ψ_s^e is the nodal value of ψ at s_{th} node in the element and $\mathbf{N}^{2D}$ is a $1\times n_s$ vector. Based on Eq.(2.9), the gradient

of the wave function can be written as,

$$\nabla\psi^e = \begin{pmatrix} \frac{\partial\psi^e}{\partial x} \\ \frac{\partial\psi^e}{\partial y} \end{pmatrix} = \begin{pmatrix} \frac{\partial N_1^{2D}}{\partial x} & \frac{\partial N_2^{2D}}{\partial x} & \cdots & \frac{\partial N_{n_s}^{2D}}{\partial x} \\ \frac{\partial N_1^{2D}}{\partial y} & \frac{\partial N_2^{2D}}{\partial y} & \cdots & \frac{\partial N_{n_s}^{2D}}{\partial y} \end{pmatrix} \cdot \begin{pmatrix} \psi_1^e \\ \psi_2^e \\ \cdots \\ \psi_{n_s}^e \end{pmatrix} = \nabla\mathbf{N}^{2D} \cdot \boldsymbol{\psi}^e \tag{2.10}$$

Similar approximation can be made to the test function $\delta\psi$, substituting Eqs. (2.9) and (2.10) into Eq. (2.8), the results for each element can be assembled into the following generalized eigenvalue problem,

$$\mathbf{H}^0\psi = (\mathbf{K} + \mathbf{U})\,\psi = E\mathbf{M}\psi \tag{2.11}$$

where $\boldsymbol{\psi}$ is the global nodal wavefunction vector, $\mathbf{K}$, $\mathbf{U}$ and $\mathbf{M}$ are assembled from the element matrices which are given by

$$\mathbf{K}^e = \frac{\hbar^2}{2}\int_{\Omega^e} (\nabla\mathbf{N}^{2D})^T\mathbf{M}^*\nabla\mathbf{N}^{2D}\mathrm{d}\Omega^e \tag{2.12}$$

$$\mathbf{M}^e = \int_{\Omega^e} (\mathbf{N}^{2D})^T\mathbf{N}^{2D}\mathrm{d}\Omega^e \tag{2.13}$$

$$\mathbf{U}^e = \int_{\Omega^e} (\mathbf{N}^{2D})^T U\mathbf{N}^{2D}\mathrm{d}\Omega^e \tag{2.14}$$

Eq. (2.11) shows an eigenvalue problem and it is used to solve for the eigen-pairs in the closed system. By solving the generalized eigenvalue problem, Eq. (2.11), a set of energy levels E_n and wave functions ψ_n can be obtained. Substituting the eigen-pairs into Eq. (2.2) and Eq. (2.3), the electron and hole concentrations can be computed. The Poisson equation is solved over the same domain Ω to obtain the potential profile. By using the Galerkin weighted residual method, the weak form of

the Poisson equation is obtained as,

$$\sum_i \int_{\Gamma_i} \varepsilon_r \frac{\partial U}{\partial n_i} \delta U \mathrm{d}\Gamma_i + \int_\Omega \varepsilon_r \nabla U \cdot \nabla \delta U \mathrm{d}\Omega = \int_\Omega e^2[-\tilde{n} + p + N_d^+ - N_a^-]\delta U \mathrm{d}\Omega \quad (2.15)$$

where δU is the variation of the potential. Note that when there is no voltage applied on the boundaries of simulation domains, the Dirichlet boundary conditions are applied on the boundaries, otherwise, the Neumann boundary conditions are applied. In either of the cases, the first term in Eq. (2.15) can be eliminated. Then the Poisson equation is solved by using the Newton-Raphson method. The system equations can be written as,

$$\mathbf{J\Delta u} = -\mathbf{R} \quad (2.16)$$

where J is the Jacobian matrix, Δu is the potential increment and R is the residual vector. Note that in the calculation of the Jacobian matrix, the derivative of the modified quantum electron concentration with respect to U is computed by [69],

$$\frac{\partial \tilde{n}}{\partial U} = \frac{eN_{nd}}{\pi\hbar}\left(\frac{2m_{nz}^*}{k_BT}\right)^{1/2} \times \sum_{n=1}^{\infty}(\psi_n^k)^2 F_{-3/2}\left(\frac{E_F - E_n^k + e(U-U^k)}{k_BT}\right) \quad (2.17)$$

2.3 CMS Approaches for Solving Schrödinger Equation

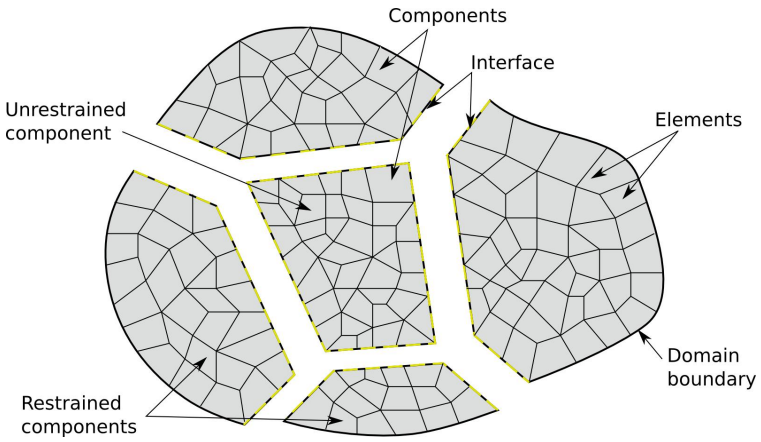

Figure 2.1: Domain decomposition in CMS approaches.

The general CMS framework is comprised of four basic steps: the division of the domain Ω into a set of components, the definition of component basis vectors, the coupling of the components to form a reduced-order global system, and the recovery of the global wave functions. Fig. (2.1) shows an example of domain decomposition in the CMS approaches. A meshed domain is discretized into a set of components. When a component boundary edge is on the global domain boundary with a homogeneous Dirichlet boundary condition, the component is referred to as a restrained component. Otherwise it is referred to as an unrestrained component. A component boundary edge that is shared by another component is referred to as an interface edge. After the domain decomposition, depending on the methods of defining the component basis vectors, there are two major variants of the CMS: the fixed-interface CMS approach [77] and the free interface CMS approach [82]. In this section, we describe the procedures of solving the effective mass Schrödinger equation (Eq. (2.1)) by using each of the approaches.

2.3.1 Fixed-interface CMS

For each component obtained from the domain decomposition as shown in Fig. (2.1), the eigenvalue problem can be denoted as,

$$\left(\mathbf{H}^{0j} - E^j \mathbf{M}^j\right) \psi^j = 0, \qquad j = 1, 2, 3, \cdots, m \tag{2.18}$$

where j denotes the component number, m is the total number of components. In an electrostatic analysis, the wave functions are zero on the domain boundary. Therefore, the degrees of freedom (DOFs) on the global boundary can be discarded. In fixed interface CMS approach, the wave function ψ^j, is partitioned into two parts which are referred to as the *attachment* part and *interior* part. The attachment part contains the wave function DOFs at nodes on interface edges which are shared by different components, and interior part contains the DOFs associated with the interior nodes of the component. The attachment and interior parts of ψ^j are denoted by subscripts a and i, respectively. With respect to the attachment and interior DOFs, Eq. (2.18) can be partitioned as,

$$\left(\begin{bmatrix} \mathbf{H}^{0j}_{ii} & \mathbf{H}^{0j}_{ia} \\ \mathbf{H}^{0j}_{ai} & \mathbf{H}^{0j}_{aa} \end{bmatrix} - E^j \begin{bmatrix} \mathbf{M}^j_{ii} & \mathbf{M}^j_{ia} \\ \mathbf{M}^j_{ai} & \mathbf{M}^j_{aa} \end{bmatrix} \right) \begin{pmatrix} \psi^j_i \\ \psi^j_a \end{pmatrix} = \begin{pmatrix} \mathbf{0} \\ \mathbf{0} \end{pmatrix} \tag{2.19}$$

In fixed interface CMS approach, the attachment DOFs are set to be fixed, i.e., $\psi^j_a = 0$, we obtain from Eq. (2.19),

$$\left(\mathbf{H}^{0j}_{ii} - E^j \mathbf{M}^j_{ii}\right) \psi^j_i = \mathbf{0} \tag{2.20}$$

The eigen-pairs (E^j,ψ^j_i) can be thus computed from Eq. (2.20) for a component j. In CMS, a small set of corresponding to a few lowest energy levels obtained from Eq.

(2.20) are retained and assembled column-wisely into the component modal matrix $\bar{D}_i^j$, i.e.,

$$\bar{\mathbf{D}}_i^j = \begin{bmatrix} \psi_{i1}^j & \psi_{i2}^j & \psi_{i3}^j \cdots \psi_{ik}^j \end{bmatrix} \tag{2.21}$$

where k is the number of kept wavefunctions and $k \ll interior\ DOFs$. Next, a constraint modal matrix is obtained by applying $E^j = 0$ in the component and enforcing a unit wave function on the attachment DOFs in Eq. (2.19),

$$\begin{bmatrix} \mathbf{H}_{ii}^{0j} & \mathbf{H}_{ia}^{0j} \\ \mathbf{H}_{ai}^{0j} & \mathbf{H}_{aa}^{0j} \end{bmatrix} \begin{pmatrix} \mathbf{X}_i^j \\ \mathbf{I}_a \end{pmatrix} = \begin{pmatrix} \mathbf{0} \\ \mathbf{R}_a^j \end{pmatrix} \tag{2.22}$$

where each column of the identity matrix I_a is used to enforce a unit magnitude of the wave function on one attachment DOFs with the wave functions on other attachment DOFs fixed to zeros, R_a^j is the resultant boundary reaction at the attachment DOFs. The expression of the constraint modal matrix for the interior DOFs can be obtained from Eq. (2.22) explicitly as,

$$\mathbf{X}_i^j = -\left(\mathbf{H}_{ii}^{0j}\right)^{-1} \mathbf{H}_{ia}^{0j} \tag{2.23}$$

Having obtained $\bar{D}_i^j$ and X_i^j, the component wave functions are then approximated by,

$$\psi^j = \begin{pmatrix} \psi_i^j \\ \psi_a^j \end{pmatrix}_{n\times 1} = \begin{bmatrix} \bar{\mathbf{D}}_i^j & \mathbf{X}_i^j \\ \mathbf{0}_a & \mathbf{I}_a \end{bmatrix}_{n\times r} \begin{pmatrix} z_i^j \\ \Psi_a^j \end{pmatrix}_{r\times 1} \tag{2.24}$$

where n is the total component DOFs, $r = k + a$ is the sum of retained component ψ_i^j and the attachment DOFs, I_a and 0_a are identity and zero matrix associated with attachment DOFs, the vector, $\begin{pmatrix} z_i^j \\ \psi_a^j \end{pmatrix}$, is a generalized coordinate vector. Equation

(2.24) can be rewritten in short form as,

$$\psi^j = \mathbf{T}^j \mathbf{z}^j \tag{2.25}$$

where T is referred to as the transformation matrix of component j. Equation (2.25) shows that the wave functions of a component can be approximated as a linear combination of the column vectors of T^j with elements of the vector z^j acting as the coefficients, i.e., the column vectors of T^j are the basis vectors of component j. Note that, since $k \ll interiorDOFs$, $r \ll n$. This property enables CMS to reduce the computational cost of calculating both component and global wave functions, on the other side, introduces an approximation error. Substituting Eq. (2.25) into Eq. (2.18), we obtain,

$$(\mathbf{H}^{0j} - E^j \mathbf{M}^j)\mathbf{T}^j \mathbf{z}^j = \mathbf{0} \tag{2.26}$$

Multiplying the transpose of T^j to both sides,

$$(\mathbf{T}^j)^T (\mathbf{H}^{0j} - E^j \mathbf{M}^j)\mathbf{T}^j \mathbf{z}^j = \mathbf{0} \tag{2.27}$$

Eq. (2.27) can be rewritten in the short form as,

$$(\bar{\mathbf{H}}^{0j} - E^j \bar{\mathbf{M}}^j)\mathbf{z}^j = \mathbf{0} \tag{2.28}$$

where

$$\bar{\mathbf{H}}^{0j} = (\mathbf{T}^j)^T \mathbf{H}^{0j} \mathbf{T}^j \tag{2.29}$$

$$\bar{\mathbf{M}}^j = (\mathbf{T}^j)^T \mathbf{M}^j \mathbf{T}^j \tag{2.30}$$

are the reduced matrices for the j_{th} component. Following the standard finite element assembly procedure, one can assemble Eq. (2.28) of the connected components into a global modal system, i.e.,

$$(\hat{\mathbf{H}}^0 - E\hat{\mathbf{M}})\hat{\mathbf{z}} = \mathbf{0} \tag{2.31}$$

where,

$$\hat{\mathbf{H}}^0 = assemble\left(\bar{\mathbf{H}}^{01},\ \ \bar{\mathbf{H}}^{02},\ \ \bar{\mathbf{H}}^{03}, \cdots, \bar{\mathbf{H}}^{0m}\right) \tag{2.32}$$

$$\hat{\mathbf{M}} = assemble\left(\bar{\mathbf{M}}^{1},\ \ \bar{\mathbf{M}}^{2},\ \ \bar{\mathbf{M}}^{3}, \cdots, \bar{\mathbf{M}}^{m}\right) \tag{2.33}$$

By solving Eq. (2.31), the z eigenvectors can be obtained. The global wavefunctions ψ can be restored by,

$$\psi = \hat{\mathbf{T}}\hat{\mathbf{z}} \tag{2.34}$$

where,

$$\hat{\mathbf{T}} = assemble\left(\mathbf{T}^{1},\ \ \mathbf{T}^{2},\ \ \mathbf{T}^{3}, \cdots, \mathbf{T}^{m}\right) \tag{2.35}$$

Note that, since the number of the component basis vectors is much less than the component DOFs, the dimension of Eq. (2.31) is much less than the total DOFs of the system. Consequently, the computational cost of solving the Schrödinger equation is largely reduced. The fixed interface CMS approach has several advantages including: (1) its simple procedures for computing the basis vectors in the transformation matrix, (2) the straightforward implementation of coupling the components to form the global modal system, and (3) its high accuracy in computing the low eigenvalues and their corresponding eigenvectors. For these reasons, the fixed interface CMS approach has been widely adopted for large scale structural dynamic problems.

2.3.2 Free-interface CMS

In the free interface CMS approach, the eigenvalue problem for the components is also given by Eq. (2.18). However, while the component basis vectors are obtained by fixing the wave functions at the component interfaces in the fixed interface CMS approach, the free interface CMS makes use of a set of pre-selected free interface wave functions along with a set of attachment modes and rigid body modes [85, 86]. In solving Eq. (2.18), the free interface CMS does not set the component wave functions on the component interfaces to be zeros. Instead, the wave functions on the interfaces are free. Therefore, Eq. (2.18) is solved directly without being converted to Eq. (2.20). In addition, the free interface CMS approach treats the restrained and unrestrained components separately.

2.3.2.1 Restrained components

For the restrained components as shown in Fig. (2.1), the free interface CMS approximation of the component wave functions is in the form of,

$$\psi^j = \begin{pmatrix} \psi_i^j \\ \psi_a^j \end{pmatrix}_{n\times 1} = \begin{bmatrix} \bar{\mathbf{D}}_i^j & \mathbf{X}_i^j \\ \bar{\mathbf{D}}_a^j & \mathbf{X}_a^j \end{bmatrix}_{n\times r} \begin{pmatrix} \mathbf{p}_i^j \\ \mathbf{p}_a^j \end{pmatrix}_{r\times 1} \tag{2.36}$$

where $\bar{D}^j$ is the matrix of retained free interface component wave functions, X^j is the attachment modal matrix, and p^j is the vector of generalized coordinates. Once again, $\bar{D}^j$, X^j and p^j are partitioned into the interior (subscript i) and attachment (subscript a) parts for each component. The set of basis vectors included in $\bar{D}^j$ represents the intrinsic wave functions of the component, while the attachment modal matrix X^j contains the wave functions excited by the adjacent components. It has been shown that, without X^j , the component basis set is incomplete, which

will lead to unacceptable results [85]. $\bar{D}^j$ is assembled column-wisely by a small set of ψ^j corresponding to the lowest energy levels obtained from Eq. (2.18), i.e.,

$$\bar{\mathbf{D}}_i^j = \begin{bmatrix} \Psi_{i1}^j & \Psi_{i2}^j & \Psi_{i3}^j \cdots \Psi_{ik}^j \end{bmatrix}_{n \times k} \tag{2.37}$$

where k denotes the number of the component wave functions kept in $\bar{D}^j$. Note that, in the solution of Eq. (2.18), the wave functions ψ^j should be mass normalized. This condition is assumed throughout the paper. Like Eq. (2.25), Eq. (2.36) can be rewritten in a short form as,

$$\psi^j = \mathbf{T}^j \mathbf{p}^j \tag{2.38}$$

where T^j is the transformation matrix containing all the component basis vectors. We apply an analogy to structural dynamics analysis, the attachment modal matrix X^j for restrained components are obtained by applying unit forces on the interface coordinates and setting $E^j = 0$ for Eq. (2.19), i.e.,

$$\begin{bmatrix} \mathbf{H}^{0j}_{ii} & \mathbf{H}^{0j}_{ia} \\ \mathbf{H}^{0j}_{ai} & \mathbf{H}^{0j}_{aa} \end{bmatrix}_{n \times n} \begin{pmatrix} \bar{\psi}_i^j \\ \bar{\psi}_b^j \end{pmatrix}_{n \times a} = \begin{pmatrix} \mathbf{0} \\ \mathbf{I}_a^j \end{pmatrix}_{n \times a} \tag{2.39}$$

where $\begin{pmatrix} \bar{\psi}_i^j \\ \bar{\psi}_b^j \end{pmatrix}$ represents the wave function response to the right hand excitation. The portion of the wave function response contributed by the retained component wave functions (i.e. the k basis vectors retained in $\bar{D}^j$ as shown in Eq. (2.37)) should be deducted to ensure the obtained attachment modes to be Hamiltonian orthogonal to the retained component wave functions [85]. The attachment modal matrix can then

be obtained as,

$$\mathbf{X}^j = \begin{pmatrix} \bar{\psi}_i^j \\ \bar{\psi}_a^j \end{pmatrix}_{n\times a} - \left(\bar{\mathbf{D}}^j\right)_{n\times k} \left(\mathbf{E}^j\right)^{-1}_{k\times k} \left(\bar{\mathbf{D}}^j\right)^T_{k\times n} \begin{pmatrix} \mathbf{0}_i^j \\ \mathbf{I}_a^j \end{pmatrix}_{n\times a} \tag{2.40}$$

where the second term on the right hand side is the wave function response contributed by $\bar{D}^j$.

2.3.2.2 Unrestrained components

For the unrestrained components (those with rigid body modes), the free interface CMS approximation has the same form of Eq. (2.36),

$$\psi^j = \begin{pmatrix} \psi_i^j \\ \psi_a^j \end{pmatrix}_{n\times 1} = \begin{bmatrix} \bar{\mathbf{D}}_i^j & \mathbf{X}_i^j \\ \bar{\mathbf{D}}_a^j & \mathbf{X}_a^j \end{bmatrix}_{n\times r} \begin{pmatrix} \mathbf{p}_i^j \\ \mathbf{p}_a^j \end{pmatrix}_{r\times 1} \tag{2.41}$$

As the wave functions of unrestrained components are not constrained, there is a rigid body mode corresponding to the zero energy level in the solution of Eq. (2.18). While there are 3 rigid body modes for $2D$ structural analysis, there is only one rigid body mode for each unrestrained component in the solution of the Schrödinger equation. Thus $\bar{D}^j$ contains an additional column vector in Eq. (2.41) compared to in Eq. (2.36). Due to the existence of the rigid body mode, the attachment modes X^j in Eq. (2.41) are computed differently to exclude the influence of the rigid body mode which is already included in $\bar{D}^j$. To obtain X^j, the Hamiltonian matrix in Eq. (2.18) is first partitioned as,

$$\mathbf{H}^{0j} = \begin{bmatrix} \mathbf{H}^{0j}_{ii} & \mathbf{H}^{0j}_{if} & \mathbf{H}^{0j}_{ir} \\ \mathbf{H}^{0j}_{fi} & \mathbf{H}^{0j}_{ff} & \mathbf{H}^{0j}_{fr} \\ \mathbf{H}^{0j}_{ri} & \mathbf{H}^{0j}_{rf} & \mathbf{H}^{0j}_{rr} \end{bmatrix}_{n\times n} \tag{2.42}$$

where i denotes the number of interior nodes, r denotes the number of rigid body coordinates (r=1 for the $2D$ Schrödinger equation) and $f = a - r$ denotes the number of interface coordinates excluding the rigid body coordinate. Note that the rigid body coordinate can be assigned on any boundary node of the component. Similar to the restrained component case, we apply an analogy to structural dynamics analysis, the attachment modes for the wave functions can be written as,

$$\mathbf{X}^j = \mathbf{F}^j_{n\times n} \begin{pmatrix} \mathbf{0}^j_i \\ \mathbf{I}^j_a \end{pmatrix}_{n\times a} - \left(\bar{\mathbf{D}}^j\right)_{n\times k} \left(\mathbf{E}^j\right)^{-1}_{k\times k} \left(\bar{\mathbf{D}}^j\right)^T_{k\times n} \begin{pmatrix} \mathbf{0}^j_i \\ \mathbf{I}^j_a \end{pmatrix}_{n\times a} \tag{2.43}$$

where the first term on the right hand side is the wave function response to the unit excitation at the interface coordinates excluding the contribution of the rigid body mode, the second term is the wave function response contribution from the retained wave functions same as in Eq. (2.40). The effect of the rigid body mode is excluded from X^j through the matrix F^j which is obtained as,

$$\mathbf{F}^j = \left(\mathbf{P}^j_r\right)^T \mathbf{F}^j_c \mathbf{P}^j_r \tag{2.44}$$

where P^j_r is the inertia-relief projection matrix defined by,

$$\mathbf{P}^j_r = \mathbf{I} - \mathbf{M}^j \left(\mathbf{D}^j_R\right)_{n\times r} \left(\mathbf{D}^j_R\right)^T_{r\times n} \tag{2.45}$$

with D_R^j being the constant rigid body mode vector, and F_c^j being the constrained flexibility matrix given by,

$$\mathbf{F}_c^j = \begin{bmatrix} \begin{bmatrix} \mathbf{H}_{ii}^{0j} & \mathbf{H}_{if}^{0j} \\ \mathbf{H}_{fi}^{0j} & \mathbf{H}_{ff}^{0j} \end{bmatrix}^{-1} & \mathbf{0} \\ \mathbf{0} & \mathbf{0} \end{bmatrix}_{n\times n} \tag{2.46}$$

Detailed derivation F^j, P_r^j and F_c^j can be found in [85]. For the sake of brevity, it is not repeated here. To this end, the transformation matrix T^j of both restrained and unrestrained components are obtained. To simplify the coupling and assembly procedure, we can rewrite the transformation matrices given in Eq. (2.36) and Eq. (2.41) in the same form as that in the fixed interface CMS approach given in Eq. (2.24) [86]. By using the lower part of Eq. (2.36) or Eq. (2.41), the generalized coordinate vector p_a^j can be expressed in terms of ψ_a^j, and the result is applied back into the upper part of Eq. (2.36) or Eq. (2.41). As a result, they can be rewritten in terms of the modal generalized coordinate vector p_i^j and the interface physical vector ψ_a^j, which leads to,

$$\psi^j = \begin{pmatrix} \psi_i^j \\ \psi_a^j \end{pmatrix}_{n\times 1} = \begin{bmatrix} \bar{\mathbf{D}}_i^j - \mathbf{X}_i^j(\mathbf{X}_a^j)^{-1}\bar{\mathbf{D}}_a^j & \mathbf{X}_i^j(\mathbf{X}_a^j)^{-1} \\ \mathbf{0}_a^j & \mathbf{I}_a^j \end{bmatrix}_{n\times r} \begin{pmatrix} \mathbf{p}_i^j \\ \psi_a^j \end{pmatrix}_{r\times 1} = \check{\mathbf{T}}^j \check{\mathbf{z}}^j \tag{2.47}$$

With the free interface component wave function approximation shown in Eq. (2.47) and the transformation matrix computed, the component model reduction, assembly of the components and the recovery of the global wave functions are carried out by using the same procedure described in Eq. (2.27) to Eq. (2.35) which is not repeated here.

2.4 Results

2.4.1 Quantum wires

To demonstrate the validity and the efficiency of the CMS approaches for quantum mechanical electrostatic analysis of nanostructures and devices, in the first example, we consider a simple $2D$ $GaAs/AlGaAs$ quantum wire as shown in Fig. (2.2a). The effective electron masses of $GaAs$ and $AlGaAs$ are set to be $m^*_{GaAs} = 0.0665m_e$ and $m^*_{AlGaAs} = 0.0858m_e$, respectively, where m_e is the vacuum electron mass. The relative dielectric constants for the silicon substrate and oxide are set to be $\varepsilon_{GaAs} = 13.18\varepsilon_0$ and $\varepsilon_{AlGaAs} = 12.3064\varepsilon_0$, respectively, where ε_0 is the vacuum dielectric constant. The cross-sectional dimensions of the quantum wire are $150\mathring{A} \times 150\mathring{A}$ for the outer boundary and $100\mathring{A} \times 100\mathring{A}$ for the GaAs core. The heterojunction step potential between GaAs and AlGaAs is set to be $0.276eV$. The $AlGaAs$ region is n-typed with a donor concentration of $10^{18}cm^{-3}$. As electrons dominate, we ignore the hole concentration in our simulation. The Dirichlet boundary condition is applied along the external boundary when solving the Schrödinger equation while the Neumann boundary condition is used for Poisson equation. In the calculation by the CMS approaches, we decompose the entire domain into a set of components as shown in Fig. (2.2b). Both the fixed and free interface CMS approaches are applied to solve the Schrödinger equation with the same number of components to obtain the energy levels and corresponding wave functions in the structure.

Fig. (2.3) and Fig. (2.4) show the electron concentrations and potential profiles obtained from the two CMS approaches on a 120×120 mesh domain with 5×5 equal-size components (576 elements in each component). For each component, 5 component wave functions are retained in each component for the construction of

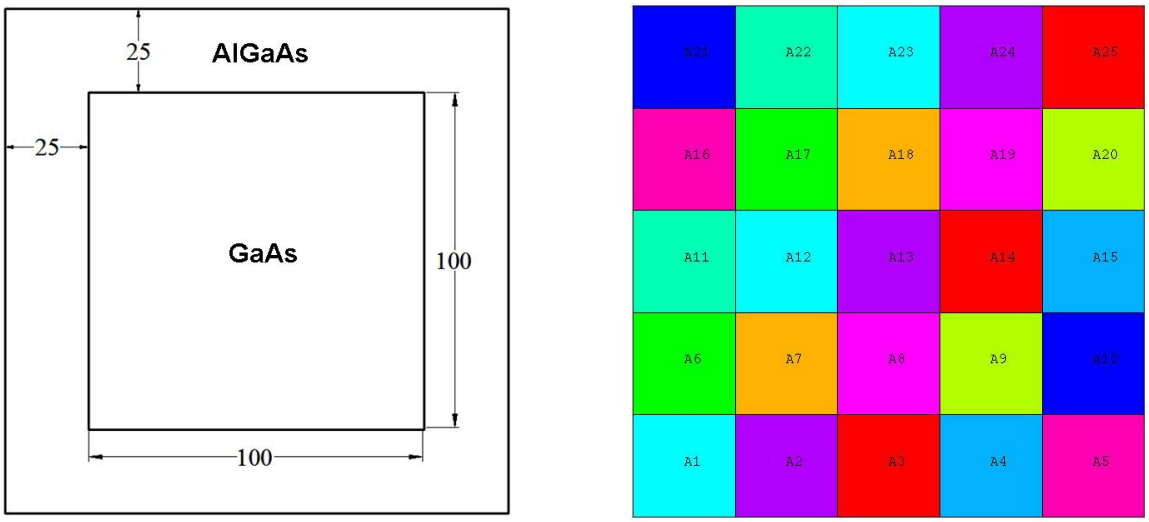

(a) (b)

Figure 2.2: (a)Quantum wire geometry (unit: $\mathring{A}$), and (b) Domain decomposition.

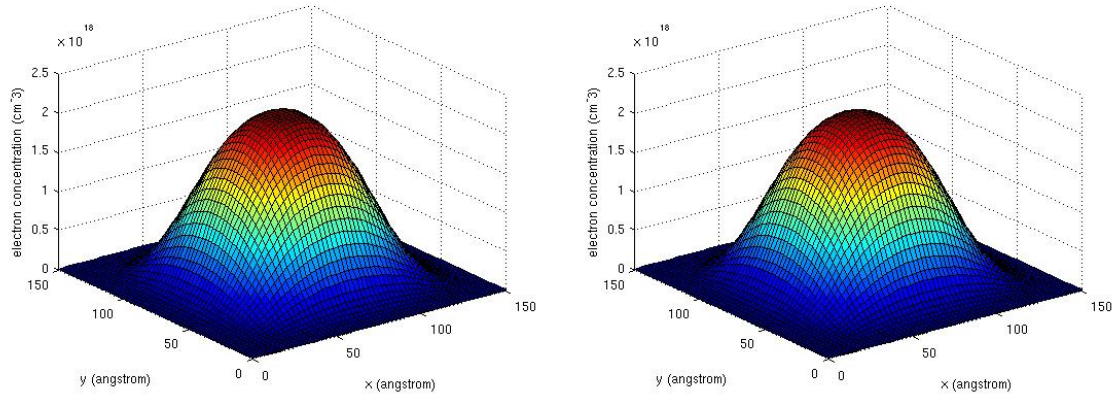

(a) (b)

Figure 2.3: Electron concentration computed using (a)fixed interface CMS and (b) free interface CMS.

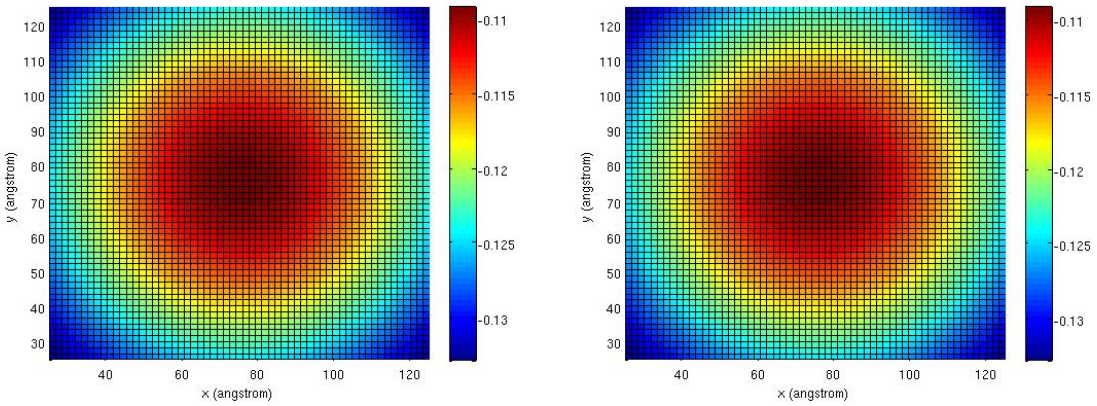

(a) (b)

Figure 2.4: Potential profiles computed using (a)fixed interface CMS and (b) free interface CMS.

the basis vectors in both approaches. In calculation of the electron concentration, 10 eigen-pairs computed by the Schrödinger equation are used, which proved to be sufficient to provide a an accurate solution for the electron concentration. The results obtained from two CMS approaches are almost identical to the results obtained from the direct finite element solution (not shown). To compare the computational cost of the two CMS approaches and direct method, the total number of elements within the domain is varied from 30×30 to 240×240 while the number of components is kept fixed, which is 25. Fig. (2.5) shows CPU time comparison of those three approaches. It is shown that, for a coarse mesh, the CPU time of the direct FEM and the CMS approaches is similar. However, when the DOFs increases, the CMS approaches reduce the computational cost significantly. As shown in the figure, when the domain is meshed with 240×240 elements, the CPU time used by direct FEM is nearly 60 times and 17 times of those used by the fixed interface CMS approach and the free interface CMS approach, respectively. Between the CMS approaches, the free interface CMS is more expensive than the fixed interface CMS due to the extra matrix manipulations required in the method as described in Section 2.3. To further

investigate the accuracy of the CMS approaches, we vary the number of components as well as the number of retained component wave functions in each component. The error between the results computed with CMS and that computed with direct FEM is measured by using a global error measure with respect to the direct FEM solution [89],

$$\epsilon = \frac{1}{|u^e|_{max}} \sqrt{\frac{1}{N_t} \sum_{i=1}^{N_t} [u_i^e - u_i^c]^2} \tag{2.48}$$

where ϵ is the error in the solution and the superscripts (e) and (c) denote the direct FEM and CMS results, respectively, N_t denotes the total DOFs. Fig. (2.6) shows the final electron concentration errors between the FEM and the CMS approaches as a function of the number of components and retained component wave functions. It is shown that the error decreases in both CMS approaches as the number of components and retained component wave functions increases. However, the error of the free interface CMS is significantly smaller than that of the fixed interface CMS. The convergence rate of the free interface CMS is consistently larger than that of the fixed interface CMS. To achieve the same accuracy, the free interface CMS requires much less retained component wave functions in each component as shown in the figure.

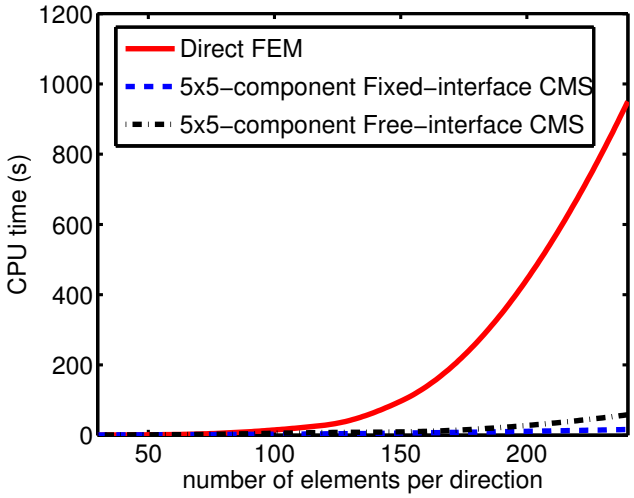

Figure 2.5: CPU time comparison of the three methods.

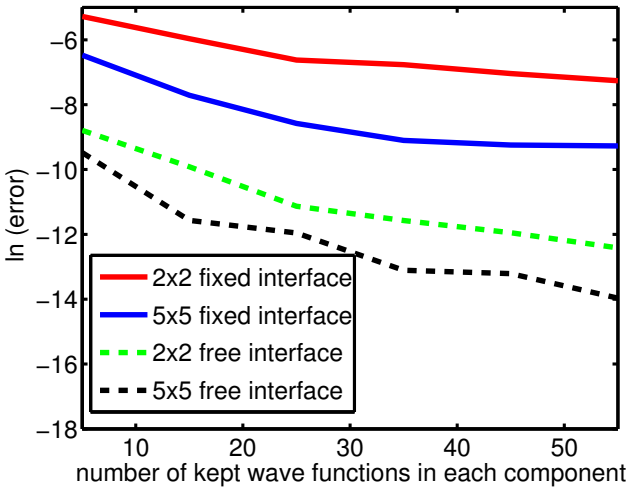

Figure 2.6: Error in electron concentration for the fixed and free interface CMS.

2.4.2 Gate-All-Around (GAA) MOSFET

In the second example, we simulate a GAA MOSFET and compute the electron concentration and potential profile in the cross section perpendicular to the transport direction within the device. The cross section of GAA MOSFET is depicted in Fig. (2.7). The size of the device is $240\mathring{A} \times 240\mathring{A}$. The central part of the MOSFET is intrinsic Si with a dimension of $200\mathring{A} \times 200\mathring{A}$. The thickness of the surrounding SiO_2 layer is $20\mathring{A}$. The metal gate work function is assumed to be $4.05eV$. A voltage of $0.5V$ is applied on the gates. The effective mass of SiO_2 is $0.5m_e$. The conduction band of Si has six equivalent valleys, with three different pairs of conduction band minima. The transverse and longitudinal electron masses are defined as $m_t^* = 0.19m_e$ and $m_l^* = 0.91m_e$, respectively. The Schrödinger equation is solved three times for each pair of the conduction band minima. Then three different sets of eigen-pairs can be obtained. The heterojunction step potential between silicon substrate and the oxide is $3.34eV$. The relative dielectric constants for the silicon substrate and oxide

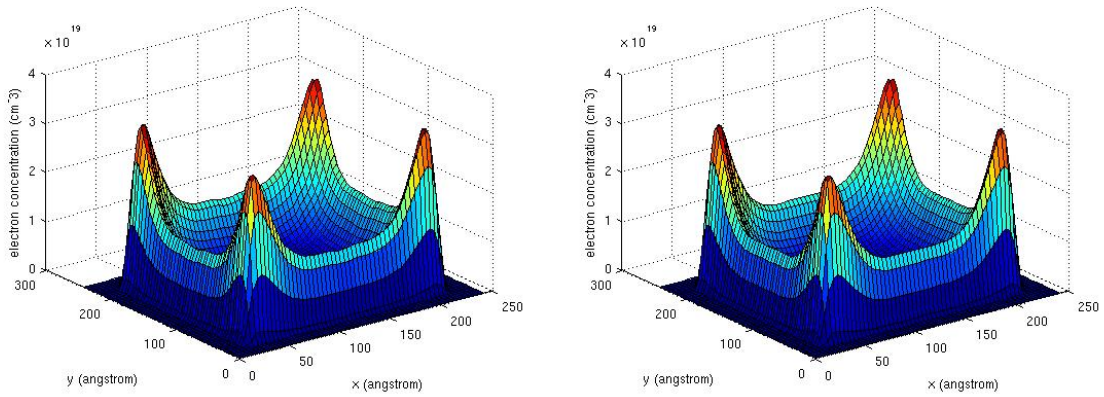

(a) (b)

Figure 2.8: Electron concentration computed using (a)fixed interface CMS and (b) free interface CMS.

are set to be $\varepsilon_{Si} = 11.7\varepsilon_0$ and $\varepsilon_{SiO_2} = 3.9\varepsilon_0$, respectively. The first 30 eigen-pairs are used to obtain an accurate description of electron concentration within the device.

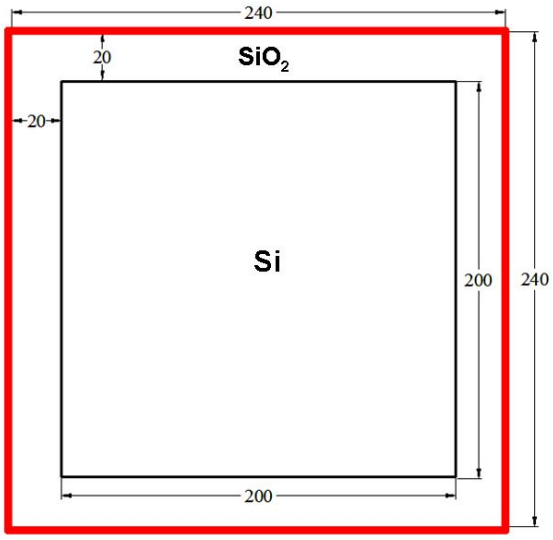

Figure 2.7: GAA MOSFET transverse cross-section (unit: $\mathring{A}$).

Fig. (2.8) and Fig. (2.9) show the electron concentration and electrostatic potential obtained with the fixed and free interface CMS approaches, respectively. In both simulations, 16 components of the same size and 5 retained component wave

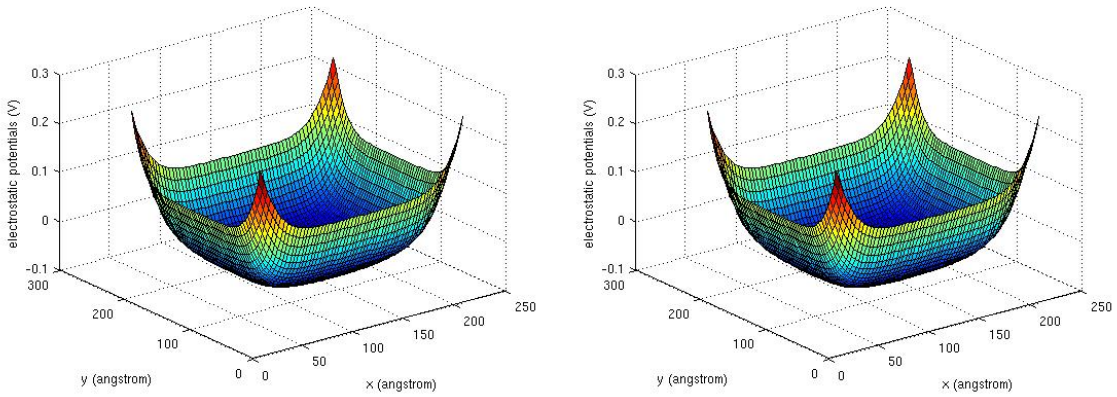

(a) (b)

Figure 2.9: Potential profiles computed using (a)fixed interface CMS and (b) free interface CMS.

functions in each component are used. The mesh size is 96×96. It is observed that the results obtained by both CMS approaches are consistent with the results obtained by the direct FEM (not shown). The CPU time for the GAA MOSFET simulations by using the direct FEM, the fixed and free interface CMS approaches with 5 retained component wave functions per component is compared in Fig. 10. In the computation, the whole domain is decomposed into 16 equal-sized components. The mesh size is ranging from 48×48 to 192×192. It is shown that with more elements (finer mesh), the computational cost reduction through the CMS approaches becomes more significant. In this example, when the domain is meshed with 192×192 elements, the fixed and free interface CMS approaches are about 28 times and 11 times faster than the direct approach, respectively.

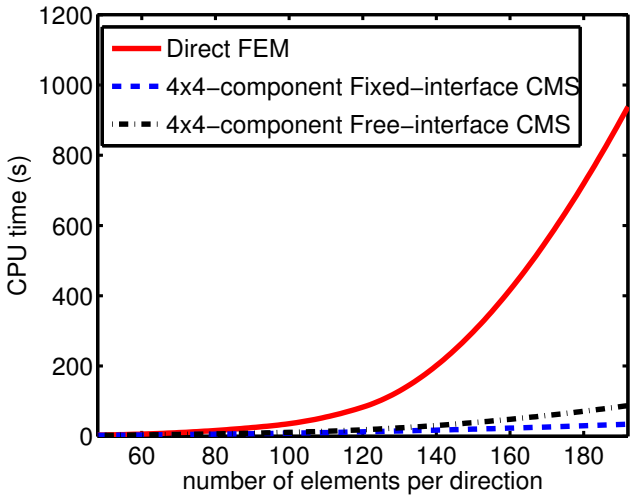

Figure 2.10: CPU time comparison of the three methods.

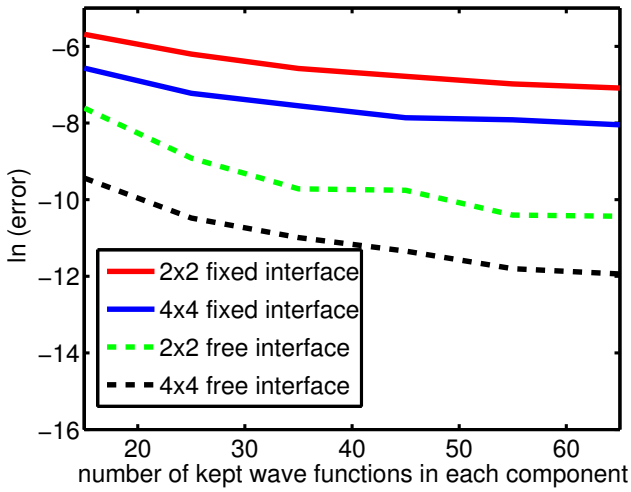

Figure 2.11: Error in electron concentration for the fixed and free interface CMS.

By using the error measure given in Eq. (2.48), the electron concentration error of the CMS approaches as a function of the number of components and retained component wave functions in each component is calculated and shown in Fig. (2.11). The convergence behavior is similar to that shown in Fig. (2.6). While the result improves as the number of retained component wave functions increases, error of the free interface CMS is significantly lower compared to the fixed interface CMS. As

shown in the first two examples, with the same number of component wave functions kept in each component, the results obtained with the free interface CMS approach are more accurate than those by the fixed interface CMS approach. To investigate the reasons, the eigenvalues computed by both methods are compared with those obtained by direct approach. Fig. (2.12) shows the relative error of eigenvalues of the CMS solutions compared to the direct solution. The results are obtained by keeping 10 wave functions in each component, and the first 30 eigen-pairs are calculated. It is shown that the relative error introduced by the free interface CMS approach is much smaller than that from the fixed interface CMS approach. Since the accuracy of the electron concentration obtained in every Schrödinger-Poisson iteration directly depends on the accuracy of the calculated eigen-pairs, the free interface CMS can therefore offer more accurate final results of electron concentration and potential.

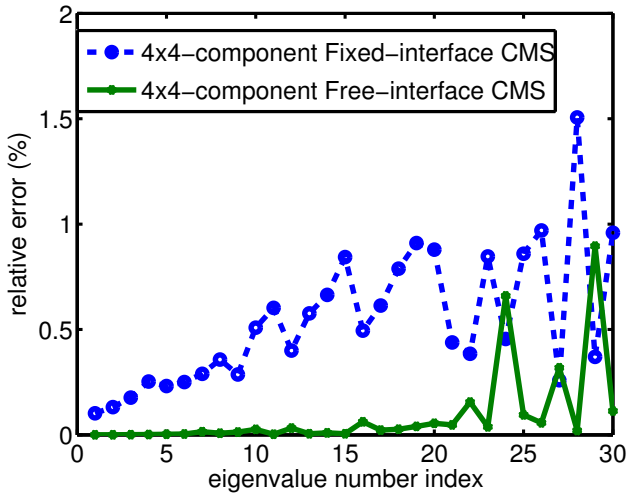

Figure 2.12: Error of computed eigenvalues from both CMS approaches.

2.4.3 Trigate MOSFET with rounded corners

In the third example, we simulate a trigate MOSFET with rounded corners as shown in Fig. (2.13a). The dimensions of the device are shown in the figure. The

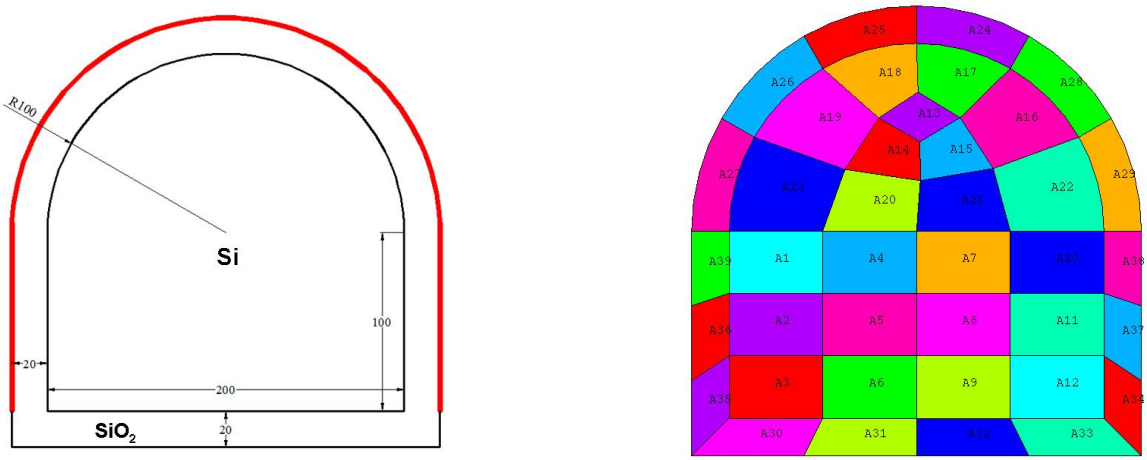

(a) (b)

Figure 2.13: (a)Trigate MOSFET with rounded corners(unit: $\mathring{A}$), and (b) Domain decomposition.

central part of the MOSFET is intrinsic Si. The remaining part is the SiO_2 layer. All the parameters for the Si and SiO_2 are the same as given in the second example. In this case, the gates are attached to the boundary of the device above $y = 20\mathring{A}$ (depicted by the red line in Fig. (2.13a)). A voltage of $0.5V$ is applied on the gates. In the CMS calculations, the domain is decomposed into 39 components (shown in Fig. (2.13b)). To correctly describe the electron concentration in the cross-section perpendicular to the carrier transport direction, 40 eigen-pairs are retained in computing the electron concentration using Eq. (2.21). In this example, the performance of two CMS approaches is similar to that in the second example. The electron concentration and electrostatic potential obtained with both CMS approaches match the results by the direct approach well. Fig. (2.14) and Fig. (2.15) show the final results obtained by both CMS approaches with a mesh of 15600 elements. In the calculation, five component wave functions are retained in each component to solve for the 40 eigen-pairs that are used to compute the electron concentration.

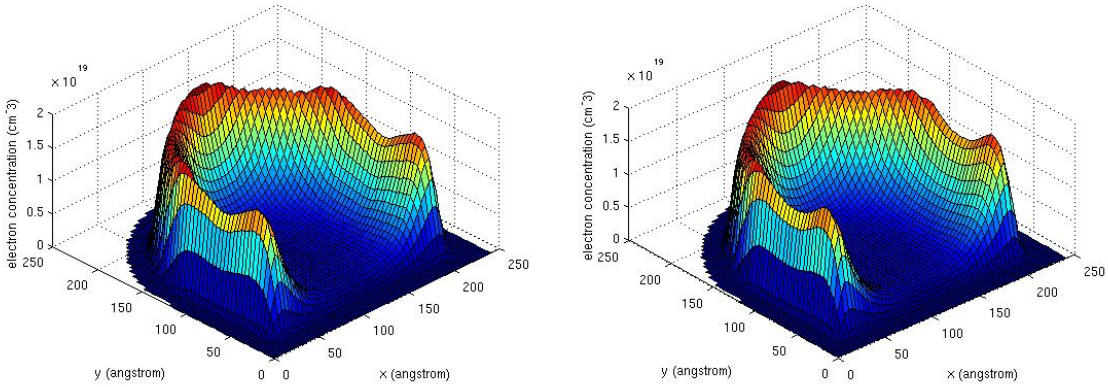

(a) (b)

Figure 2.14: Electron concentration computed using (a)fixed interface CMS and (b) free interface CMS.

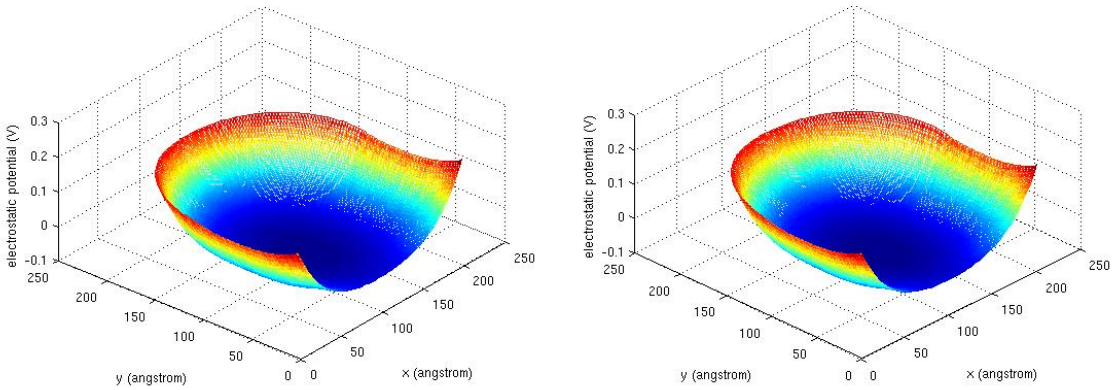

(a) (b)

Figure 2.15: Potential profiles computed using (a)fixed interface CMS and (b) free interface CMS.

The CPU time comparison for the MOSFET simulations is shown in Fig. (2.16). The CPU time for the trigate MOSFET simulations by using the direct approach, the fixed and free interface CMS approaches with 5 retained wave functions per component is compared. It is shown that for the fine mesh with 47775 elements in total, the fixed and free interface CMS approaches are about 13 times and 7 times faster than the direct FEM, respectively. The error comparison for the CMS approaches is shown in Fig. (2.17). Once again, the free interface CMS approach shows a superior performance in the solution accuracy as well as the convergence rate.

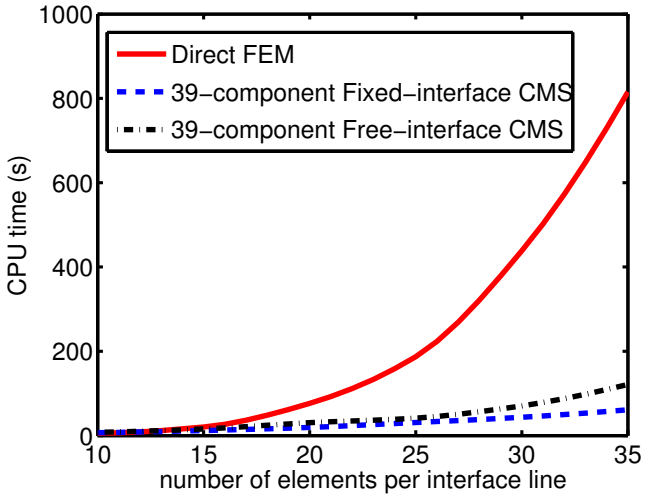

Figure 2.16: CPU time comparison of the three methods.

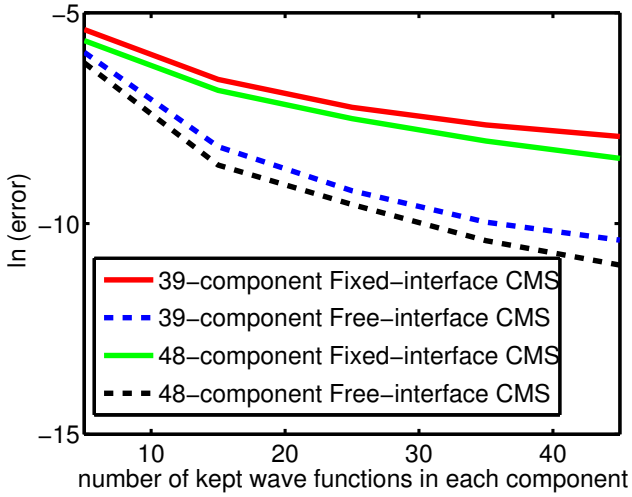

Figure 2.17: Error in electron concentration for the fixed and free interface CMS.

2.5 Summary

In this chapter, two component mode synthesis (CMS) approaches, namely, the fixed interface CMS approach and the free interface CMS approach, are presented and compared for $2D$ quantum mechanical electrostatic analysis of nanoscale structures and devices with arbitrary geometries. The CMS approaches are employed to compute the charge concentrations and potential profiles of several nanoscale structures and devices, including a quantum wire, a GAA MOSFET and a trigate MOSFET. The results obtained from the CMS approaches are compared with those obtained from the direct FEM. It is shown that both CMS approaches can yield accurate results with much less computational cost compared to the direct finite element analysis. To achieve the same accuracy, the number of component wave functions required to be retained in the free interface CMS approach is much less than that in the fixed interface CMS approach. The reduction of computational cost becomes more significant as the total degrees of freedom of the system increase.

In general, the fixed interface CMS approach is more efficient than the free interface CMS approach due to its simpler matrix operations in the computational process.

CHAPTER 3

STRAIN EFFECT ANALYSIS ON THE ELECTRICAL CONDUCTIVITY OF $Si/Si_{1-x}Ge_x$ NANOCOMPOSITE THIN FILMS

3.1 Introduction

The development of nanostructured materials, such as particulate, layered and fibrous nanocomposites, has opened the possibilities of tailoring material thermal and electrical properties in a controlled manner [9, 34–36, 90–92]. $Si/Si_{1-x}Ge_x$ nanocomposite thin-films have been fabricated to produce high-mobility MOS thin-film transistors (TFT) for displays, active RF tags and thin-film sensors, etc. [36]. Bulk or thin film Si/Ge nanocomposite thermoelectric materials, where

$Si_{1-x}Ge_x$ nanowires, nanolayers or nanoparticles are embedded in Si host, have also been proposed recently [9, 35, 90–92]. It has been reported that the thermoelectric energy conversion efficiency can be significantly improved in nanocomposites because of their largely increased material interfaces, which strongly scatter phonons but only slightly influence the charge carrier (electron or hole) transport, leading to significantly reduced phonon thermal conductivity and a maintained or improved power factor. While modeling and analysis of both thermal and electrical conductivities in nanocomposite materials has been investigated by different groups [37–39] mainly based on the Boltzmann transport equation under the relaxation-time approximation, the effect of strain on electrical transport, which plays an important role in single crystal semiconductor materials, has not yet been addressed for nanocomposite materials. Strain has been serving as an important tool in enhancing the performance of modern CMOS devices [93–95]. Crystal lattice deformation can induce band structure changes in semiconductor materials. The band structure variation is commonly composed of band splitting and band wrapping [55, 56]. Band splitting may cause electron redistribution in the band valleys while band warping can result in conductivity effective mass change. For example, there are six degenerate conduction band valleys in unstrained single crystal silicon. A uniaxial $\langle 100 \rangle$ strain can destroy the degeneracy and split the six equivalent valleys into a two-fold and a four-fold valleys. The band splitting can reduce the inter-valley scattering and increase electron occupancy in the valleys with lower energies, and consequently influence the electron transport in the material. Strain effect on the lineup band offsets of different semiconductor materials has been studied extensively in the literature [96–100]. It has been shown that strain can be used to tune the band structure of a single material or tailor the band offsets between different semiconductor materials. While most of the existing

strain effect analysis has been focused on the strains at hetero-junctions due to lattice mismatch of dissimilar crystalline semiconductor materials, variation of electron transport properties due to externally applied mechanical strains has not been studied in details. As there has been increasing effort in developing flexible electronic materials for various applications [101–103], the effect of externally applied mechanical strains on the electron transport properties of thin-film semiconductor materials becomes important. However, in nano-sized semiconductor thin films where electron transport is ballistic and quantum effect plays an important role, it is not yet clear how externally applied strains will affect the electron transport, especially when there are different materials in the system. A better understanding on this matter will benefit the design and control of the electron transport in flexible electronic devices.

In this chapter, we propose a modeling approach for investigating the effects of mechanical strain on electrical conductivity of semiconductor nanocomposite thin films, and analyze the effect of uniaxial and biaxial strains on the electrical conductivity of $Si/Si_{1-x}Ge_x$ nanocomposite thin films with $Si_{1-x}Ge_x$ nanowires embedded in Si host. To the best of our knowledge, this is the first computational study of strain effects on electrical conductivity of nanocomposite materials. We utilize a degenerate two-band k $\cdot$ p theory [104–106] to calculate the variation of the electronic band structures in deformed crystal lattices of Si and $Si_{1-x}Ge_x$. To calculate the electrical conductivity, we adopt a real-space non-equilibrium Green's function (NEGF) approach [49, 52] for the analysis of electron transport in the nanocomposite thin films. The NEGF can reliably capture the quantum effect which may play a key role in the performance of these nanoscale systems. In addition, by coupling with the Poisson equation, the space charge effect can be properly considered. The NEGF method has been successfully applied in the calculation of

electrical transport properties of superlattices [107], nanotubes [27], nanowires [6] and molecular electronics [108]. In this chapter, by solving the NEGF and Poisson equations self-consistently, we explicitly calculate the energy band profile, electron density and current density within the nanocomposite material. The IV curve can then be obtained by applying different voltages across the material. Finally, the electrical conductivity of the material can be calculated from the slope of the IV curve. By including the strain-induced band structure change in the NEGF, a set of IV curves under different strains are calculated. The electrical conductivity of the nanocomposite material as a function of the applied strains is computed from these IV curves. The rest of the chapter is organized as follows. Section 3.2 describes the theoretical model and computational procedures for the calculation of strain-dependent electrical conductivity of the $Si/Si_{1-x}Ge_x$ nanocomposite thin films, numerical results and discussions are presented in Section 3.3, and Section 3.4 presents the summary.

3.2 Theoretical Model and Computational Procedures

3.2.1 $Si/Si_{1-x}Ge_x$ nanocomposite thin films

Fig. (3.1) shows a $Si/Si_{1-x}Ge_x$ nanocomposite thin film considered in this chapter. In the thin film, a layer of $Si_{1-x}Ge_x$ nanowires are uniformly embedded in the Si host material. The distance between the nanowires is denoted as s in the figure. Note that, when $s = 0$ the nanowires merge into a $Si_{1-x}Ge_x$ layer and the thin-film structure becomes a superlattice. The Cartesian x, y and z directions are assumed to align with the [100], [010] and [001] directions of the crystal lattice,

respectively. The thin film's dimensions in the y and z directions are much larger than the thickness. The through-thickness electrical conductivity (x-direction) of the thin film is to be calculated. Due to the translational symmetry of the thin film in the y-direction ([010] direction) and invariant material properties in the z-direction, a two-dimensional unit cell with periodic boundary conditions on the top and bottom edges is taken as our simulation target, as shown in Fig. (3.1). A positive voltage, V_d, is then applied to two semi-infinite electrode contacts attached to the unit cell. In the computational analysis, the electrode contacts are modeled as the source and drain regions with different electrochemical potentials, namely, μ_1 and μ_2, and the electrochemical potentials are separated by the positive voltage with a relation $\mu_2 = \mu_1 - eV_d$, where e is the unit charge. Equilibrium condition is assumed within the ideal contacts. By applying different voltages on the contacts, a set of current densities can be calculated, which can be used to produce the IV curve of the material. Due to the small thickness of the thin film, the through thickness electron transport is assumed to be ballistic. In addition, the crystal lattice constants of Si and $Si_{1-x}Ge_x$ are assumed to be preserved across the material interface. Therefore, interface strains due to lattice mismatch and grain boundary scattering are not considered. In this chapter, we consider a n-type nanocomposite thin film with a doping density of $5 \times 10^{17} \sim 10^{19} cm^{-3}$. The doping density is set to be the same in Si and $Si_{1-x}Ge_x$ regions. The contribution of hole transport to the current is neglected. Under unstrained condition, the conduction band edge discontinuity between Si and $Si_{1-x}Ge_x$ included in the Hamiltonian, ΔE, is calculated with electron affinity model by $0.05 \times x$, where x is the Ge content in $Si_{1-x}Ge_x$ alloy [109]. The doping density of source and drain regions is set to be $10^{20} cm^{-3}$. Note that, the size of the source and drain regions is taken to be sufficiently large such that charge neutrality within the computational domain is

ensured [52].

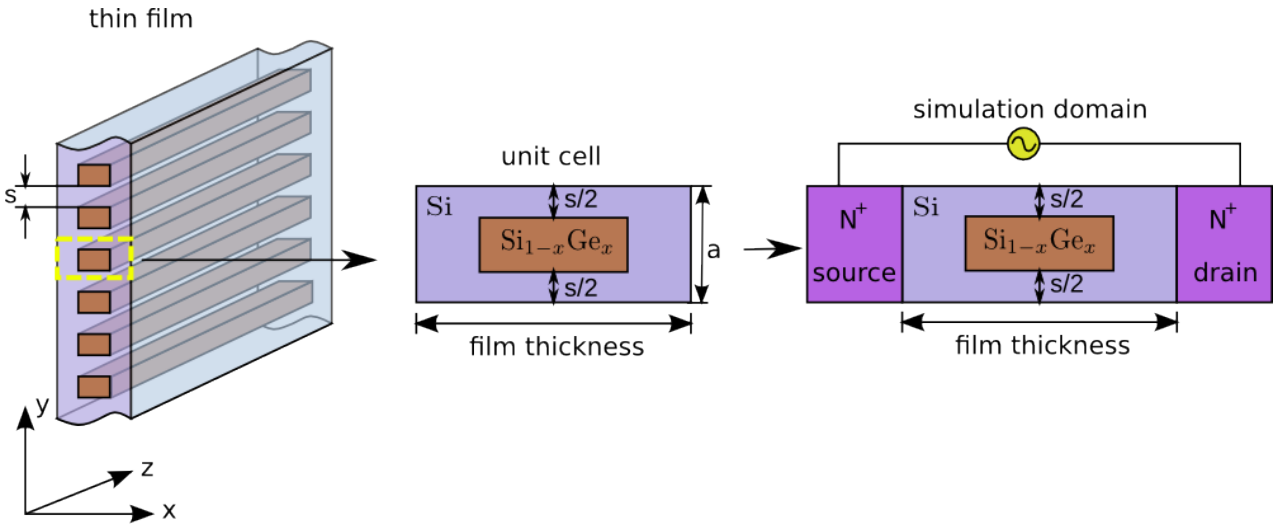

Figure 3.1: $Si_{1-x}Ge_x$ nanocomposite thin film and corresponding simulation domain.

3.2.2 Strain effect on band structures of Si and $Si_{1-x}Ge_x$

To calculate the electrical conductivity of the nanocomposite films under different strain conditions, it is necessary to study strain effect on band structures of Si and $Si_{1-x}Ge_x$ individually. For a Si crystal under no strain, there are six degenerate valleys with the same energy minima and the population of electrons in each distinct valley can be considered equivalent. However, advantageous strain reduces the symmetry of those valleys, causing band energy splitting and warping, resulting in a variation of the conduction band minima and the effective mass [55, 56, 95, 110]. Fig. (3.2) shows a diagram of band structure change under uniaxial stress for bulk n-type Si. The longitudinal tensile strain in [100] direction splits the six originally equivalent subbands, causing the Δ_4 subbands, i.e., valleys perpendicular to [100] direction, to shift down and the Δ_2 subbands, i.e., valleys along [100] direction, to shift up and leading to electron re-population from the Δ_2

valleys to the Δ_4 valleys. If the current transports in [100] direction, since the valleys in [010] and [001] directions with lower conductivity effective mass have relatively higher electron mobility compared to the other two valleys in [100] direction, with more electrons distributed in the four-fold valleys, the conductivity will be increased. For $Si_{1-x}Ge_x$ alloys, generally the band structure and electronic properties can be modeled as Si-like with the lowest conduction minima near the **X**-point in the Brillouin zone for $x < 0.85$ and as Ge-like with conduction band minima at the **L**-point for $x > 0.85$ [109]. Here we assume that the lowest conduction band of $Si_{1-x}Ge_x$ lies at the 0.85X points of Δ valleys, the same as that in Si.

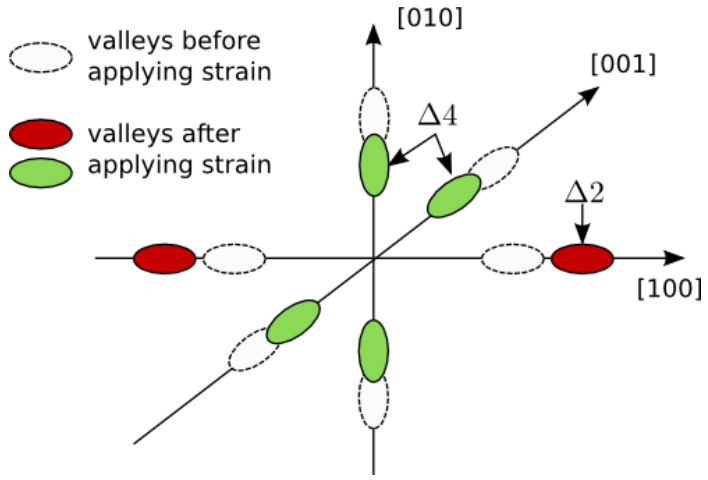

Figure 3.2: Simplified band structure change under uniaxial strain for bulk n-type Si.

A degenerate two-band k · p theory [104–106] is adopted here to quantitatively calculate the energy subband shift due to an applied strain. For Si and $Si_{1-x}Ge_x$ conduction band edges, the energy shift of a given conduction band valley can be described by,

$$\Delta E_C = \Xi_d \cdot (\epsilon_{xx} + \epsilon_{yy} + \epsilon_{zz}) + \Xi_u \cdot (\hat{k} \cdot \epsilon_{ij} \cdot \hat{k}) \tag{3.1}$$

where ϵ is the strain, Ξ_d and Ξ_u are the dilation and uniaxial-shear deformation potentials at the conduction band edges, respectively, which can be obtained from

electronic structure calculations [111]. In Eq. (3.1), i and j represent x, y or z and k is the unit vector along the valley in the reciprocal space. Note that Eq. (3.1) holds for arbitrary strain conditions. However, since shear strain is not considered in this chapter, the band shift obtained from Eq. (3.1) is only due to the normal (uniaxial and biaxial) strains. Based on the degenerate two-band k $\cdot$ p theory, since the band warping and effective mass changes are due to the shear strains, without shear strain, the effective masses of Si and $Si_{1-x}Ge_x$ remain unchanged. Table 3.1 summarizes the parameters we use for the calculation of band shift of Si and $Si_{1-x}Ge_x$. Note that the band offset $\Delta E = E_C(Si_{1-x}Ge_x) - E_C(Si)$. As a test of the parameters shown in Table 3.1, we calculate the band splitting of silicon with $\langle 100 \rangle$ uniaxial strain and compare our results with the results from Ref. [55, 56]. For 1% $\langle 100 \rangle$ uniaxial strain, the conduction band edge splitting between two-fold and four-fold conduction bands is 0.15 eV measured from experiments in Ref. [55], 0.11eV obtained from first principles calculation in Ref. [55]and 0.1344eV from our calculation, respectively. The results are in reasonable agreement.

Table 3.1: Parameters used to calculate the band structure of Si and $Si_{1-x}Ge_x$.

Material parameters	Symbols	Values	Ref.
electron longitudinal/transverse effective mass of Si	m_l^*/m_t^*	$0.92m_e/0.19m_e$	[109]
electron longitudinal/transverse effective mass of $Si_{1-x}Ge_x$	m_l^*/m_t^*	$0.92m_e/0.19m_e$	[109]
Dilation/uniaxial-shear deformation potentials of Si	Ξ_d/Ξ_u	$1.1eV/10.5eV$	[112]
Dilation/uniaxial-shear deformation potentials of $Si_{1-x}Ge_x$	Ξ_d/Ξ_u	$(1.1+3.4x)eV$ $(10.5-0.75x)eV$	[112]
Band offset between Si and $Si_{1-x}Ge_x$ conduction band edges	ΔE	$0.05xeV$	[109]

3.2.3 Electrical transport analysis of strained nanocomposite thin films

After obtaining the variation of the electronic band structures induced by external strains, the current due to a given applied voltage across the thin films is solved by using a $2D$ real-space Non-equilibrium Green's Function (NEGF) formulation coupled self-consistently with the Poisson equation [49, 52]. Considering the periodicity of the unit cell in y-direction, the $2D$ wave function in the thin film can be written in the Bloch form as $\psi(x, y \pm na) = \psi(x, y)e^{\pm ik_y na}$ where $\psi(x, y)$ is the wave function in the unit cell, k_y is the reciprocal space wave vector in y direction, a is the unit cell size in y direction, and $n = 0, 1, 2, \cdots$, are integers. The Hamiltonian of the unit cell can be obtained as,

$$\tilde{\mathbf{H}}(x, y) = \mathbf{H}(x, y) + \mathbf{H}'_c(x, y)e^{-ik_y a} + \mathbf{H}_c(x, y)e^{ik_y a} \tag{3.2}$$

In this chapter, 9 k_y points within the first Brillouin Zone are used to obtain a correct description of energy bands in y direction. The $2D$ representative unit cell is discretized into a uniform grid with $N_x \times N_y$ nodes. By using the effective mass approximate and a finite difference (FD) scheme, the Hamiltonian on the right hand side of Eq. (3.2) can be written in matrix form as,

$$\mathbf{H}(x, y) = \begin{bmatrix} \alpha & \beta & 0 & \cdots & 0 \\ \beta & \alpha & \beta & \cdots & 0 \\ \cdots & \cdots & \cdots & \cdots & \cdots \\ 0 & \cdots & \cdots & \cdots & \beta \\ 0 & 0 & \cdots & \beta & \alpha \end{bmatrix}_{N_x N_y \times N_x N_y} \tag{3.3}$$

and

$$\mathbf{H}_c(x,y) = \begin{bmatrix} \gamma & 0 & 0 & \cdots & 0 \\ 0 & \gamma & 0 & \cdots & 0 \\ \cdots & \cdots & \cdots & \cdots & \cdots \\ 0 & \cdots & \cdots & \cdots & 0 \\ 0 & 0 & \cdots & 0 & \gamma \end{bmatrix}_{N_xN_y \times N_xN_y} \tag{3.4}$$

where the blocks α, β and γ can be written as,

$$\alpha(x) = \begin{bmatrix} 2t_x + 2t_y + V_1(x) & -t_y & 0 & \cdots & 0 \\ -t_y & 2t_x + 2t_y + V_2(x) & -t_y & \cdots & 0 \\ 0 & \cdots & \cdots & \cdots & \cdots \\ 0 & 0 & \cdots & -t_y & 2t_x + 2t_y + V_{N_y}(x) \end{bmatrix}_{N_y \times N_y} \tag{3.5}$$

$$\beta = \begin{bmatrix} -t_x & 0 & \cdots & 0 \\ 0 & -t_x & \cdots & \cdots \\ \cdots & \cdots & \cdots & \cdots \\ 0 & \cdots & \cdots & -t_x \end{bmatrix}_{N_y \times N_y} \tag{3.6}$$

$$\gamma = \begin{bmatrix} 0 & 0 & \cdots & 0 \\ 0 & 0 & \cdots & \cdots \\ \cdots & \cdots & \cdots & \cdots \\ -t_y & \cdots & \cdots & 0 \end{bmatrix}_{N_y \times N_y} \tag{3.7}$$

where $t_x = \hbar^2/2m_x^{*v}(\Delta x)^2$, $t_y = \hbar^2/2m_y^{*v}(\Delta y)^2$, Δx and Δy are the mesh sizes in the x- and y-directions, respectively, m_x^{*v} and m_x^{*v} are the effective masses of electrons of v-th valley in x- and y-directions, respectively. In block α,

$$\mathbf{V}_i = \mathbf{U}_i + \Delta E_i^v + \Delta E_{Ci}^v \qquad\qquad i = 1, 2, 3, \cdots \tag{3.8}$$

where U is the potential energy obtained by solving the Poisson equation, ΔE^v is the band offset between different material regions for valley v, and ΔE_c^v is strain-induced energy shift of v-th conduction band edge calculated from Eq. (3.1). By definition, the retarded real-space NEGF can be expressed as [49, 52],

$$\mathbf{G}(E) = [(E + j\gamma)\mathbf{I} - \tilde{\mathbf{H}}(x, y)]^{-1} \tag{3.9}$$

where j is the imaginary unit, γ is a very small positive number and $\tilde{\mathbf{H}}(x, y)$ has infinite dimensions due to the semi-infinite contacts the unit cell is attached to. To truncate it into finite dimensions, a self-energy function, which describes the interactions between the contacts and the active conductive region is introduced. The retarded real-space NEGF can then be rewritten as,

$$\mathbf{G}(E) = [(E + j\gamma)\mathbf{I} - \hat{\mathbf{H}}(x, y) - \Sigma_S - \Sigma_D]^{-1} \tag{3.10}$$

where $\hat{H}(x, y)$ is the Hamiltonian with reduced dimensions, Σ_S and Σ_D are the source and drain contact self-energy matrix, respectively. According to Ref. [113], for any contact which the simulation domain is attached to, since it is assumed to be semi-infinite, before the self-energy matrix is introduced into NEGF, by using Finite Difference (FD) method, the entire system Hamiltonian can be written as,

$$\mathbf{H}(x, y) = \begin{bmatrix} \hat{\mathbf{H}}(x, y) & \mathbf{U}_c \\ \mathbf{U}_c^\dagger & \mathbf{H}_{cont}(x, y) \end{bmatrix} \tag{3.11}$$

where $\hat{\mathbf{H}}$ is the Hamiltonian for the central simulation domain, $\mathbf{H}_{cont}$ is the Hamiltonian for any single semi-infinite contact region which the device attaches to

and $\mathbf{U}_c$ is the coupling block matrix which could be written as,

$$\mathbf{U}_c = \begin{bmatrix} 0 & 0 & ... & 0 \\ ... & ... & ... & ... \\ \beta & ... & ... & 0 \end{bmatrix} \tag{3.12}$$

where the block β is defined in Eq. (3.6). By definition, the retarded Green's function for the whole domain can be partitioned as,

$$\begin{bmatrix} \mathbf{G}(x,y) & \mathbf{G}_{d,cont}(x,y) \\ \mathbf{G}_{cont,d}(x,y) & \mathbf{G}_{cont}(x,y) \end{bmatrix} = \begin{bmatrix} E\mathbf{I} - \hat{\mathbf{H}}(x,y) & -\mathbf{U}_c \\ -\mathbf{U}_c^{\dagger} & E\mathbf{I} - \mathbf{H}_{cont}(x,y) \end{bmatrix}^{-1} \tag{3.13}$$

The only matrix block of our interest is $\mathbf{G}(x,y)$, using simple algebra for the inversion, it can be written as,

$$\mathbf{G}(x,y) = \left[E\mathbf{I} - \hat{\mathbf{H}}(x,y) - \mathbf{\Sigma}_{cont} \right]^{-1} \tag{3.14}$$

where the self-energy matrix could be written as,

$$\mathbf{\Sigma}_{cont} = \begin{bmatrix} 0 & 0 & ... & 0 \\ ... & ... & ... & ... \\ \beta & ... & ... & 0 \end{bmatrix} \left[\begin{array}{c|cccc} E\mathbf{I} - \tilde{\alpha} & \beta & ... & ... & ... \\ \hline \beta & E\mathbf{I} - \tilde{\alpha} & \beta & ... & ... \\ ... & ... & ... & ... & ... \\ ... & ... & ... & \beta & E\mathbf{I} - \tilde{\alpha} \end{array}\right]^{-1} \begin{bmatrix} 0 & ... & ... & \beta \\ ... & ... & ... & ... \\ ... & ... & ... & 0 \end{bmatrix} \tag{3.15}$$

where $\tilde{\alpha}$ can be written as,

$$\tilde{\alpha} = \begin{bmatrix} 2t_x + 2t_y + U_1(x) & -t_y & 0 & ... & 0 \\ -t_y & 2t_x + 2t_y + U_2(x) & -t_y & ... & 0 \\ 0 & ... & ... & ... & ... \\ 0 & ... & ... & -t_y & 2t_x + 2t_y + U_{N_y}(x) \end{bmatrix}_{N_y \times N_y} \tag{3.16}$$

U_i denotes the potentials on the nodes connecting the central simulation domain to the contact. As can be seen in Eq. (3.15), we only need to obtained the first block of the matrix inverse in the middle. Dividing the matrix into four blocks as shown, note that the diagonal blocks in it are invariant based on the assumption of translational invariance of the contacts, additionally, the contacts are assumed to be semi-infinite, combining those properties, the following expression for calculating the first block of the matrix inverse could be obtained,

$$\mathbf{I} = \mathbf{g}_{cont} \left[E\mathbf{I} - \tilde{\alpha} - \beta \mathbf{g}_{cont} \beta \right] \tag{3.17}$$

where $\mathbf{g}_{cont}$ denotes the first block of the matrix inverse. Once $\mathbf{g}_{cont}$ is obtained, the self-energy matrix could be calculated as,

$$\mathbf{\Sigma}_{cont} = \begin{bmatrix} 0 & ... & ... & 0 \\ ... & ... & ... & ... \\ 0 & ... & ... & \beta \mathbf{g}_{cont} \beta \end{bmatrix} \tag{3.18}$$

By using Eq. (3.11) to Eq. (3.18), Σ_S and Σ_D can be obtained straightforwardly. Note that, for the small thickness of the nanocomposite thin films considered in this chapter (a few nanometers), ballistic electron transport is assumed. This assumption is

appropriate when the thickness of the thin films is less or comparable to the electron mean free path in the material. For a thin film with a thickness larger than the electron mean free path (larger than 10 nm in our case), carrier scattering effects can be considered by including a scattering term in Eq. (3.8) [48]. In this chapter, for an efficient calculation of the retarded NEGF, a recursive algorithm is adopted [51]. The self-energy matrices can be used to obtain the broadening functions for the source and drain contacts, which are used to account for the electron exchange rates between the source and drain reservoirs and the active conductive region. The broadening functions are given by [49, 52],

$$\mathbf{\Gamma}_S = j[\mathbf{\Sigma}_S - \mathbf{\Sigma}_S^\dagger], \qquad \mathbf{\Gamma}_D = j[\mathbf{\Sigma}_D - \mathbf{\Sigma}_D^\dagger] \tag{3.19}$$

where † denotes the Hermitian conjugate. With the retarded NEGF (Eq. (3.10)) and the broadening matrices (Eq. (3.19)), the spectral functions for the reservoirs can be computed as,

$$\mathbf{A}_S = \mathbf{G}\mathbf{\Gamma}_S\mathbf{G}^\dagger, \qquad \mathbf{A}_D = \mathbf{G}\mathbf{\Gamma}_D\mathbf{G}^\dagger \tag{3.20}$$

The correlation function $\mathbf{G^n}(E)$ measuring the contribution from the reservoirs can then be calculated by,

$$\mathbf{G^n}(E) = \mathbf{A}_S(E)F(E, E_{fS}) + \mathbf{A}_D(E)F(E, E_{fD}) \tag{3.21}$$

where the Fermi function $F(E, E_f)$ is given by,

$$F(E, E_f) = \sqrt{\frac{2m_z^* k_B T}{\pi\hbar^2}} F_{-1/2}\left(\frac{E_f - E}{k_B T}\right) \tag{3.22}$$

where $F_{-1/2}$ is the complete Fermi-Dirac integral of order $-1/2$, m_z^* is the electron

effective mass in the z direction. Finally, the local electron density is obtained by,

$$\mathbf{n}(E) = \frac{1}{2\pi\Delta x\Delta y} diag(\mathbf{G^n}(E)) \tag{3.23}$$

Note that an integration of $\mathbf{n}(E)$ over the in-plane energy E is required to obtain the total electron density within the simulation domain. When there are multiple conduction valleys, contributions from all the valleys should be included.

After the electron density is obtained by using Eq. (3.23), the $2D$ Poisson equation is solved to obtain the potential energy in the domain. Based on Eq. (2.4), in an electron dominant case, the Poisson equation can simplified as,

$$\nabla \cdot (\varepsilon_r \nabla U) = e^2(N_d^+ - n) \tag{3.24}$$

For a better convergence and stability of the numerical solution, in this chapter, we employ a predictor-corrector approach for solving the Poisson equation [52, 114],

$$\nabla \cdot (\varepsilon_r \nabla U) = e^2(N_d^+ - N_c F_{1/2}\left(\frac{F_n - U}{k_B T}\right)) \tag{3.25}$$

where N_c is the effective density of states in the conduction band and F_n is defined as a quasi-Fermi level which is given by,

$$F_n = \tilde{U} + \frac{k_B T}{e} F_{1/2}^{-1}\left(\frac{n}{N_c}\right) \tag{3.26}$$

where $\tilde{U}$ is the potential energy obtained from the previous NEGF-Poisson iteration and $F_{1/2}^{-1}$ is the inverse of the complete Fermi-Dirac integral of order $1/2$. The nonlinear Eq. (3.25) is solved by using the Newton-Raphson method as that in Eq. (2.16). A self-consistent solution of the electron density and potential profile is obtained by

iterating between the NEGF and Poisson equations. Upon convergence of the solution, the current density from source to drain can be calculated by [49, 52],

$$I = \frac{e}{2\pi\hbar} \int T_{SD}(E)[F(E, E_{fS}) - F(E, E_{fD})]dE \tag{3.27}$$

where T_{SD} is the transmission function and it is defined as,

$$T_{SD} = Trace[\mathbf{\Gamma_S G \Gamma_D G^{\dagger}}] \tag{3.28}$$

Note that, the contributions from all the valleys need to be included in Eq. (3.27) to compute the final current density in the material. The IV curve can be obtained by applying a set of voltages on the source and drain contacts. Finally, the electrical conductivity of the material is calculated from the slope of the IV curve in its linear regime.

3.3 Results and Discussions

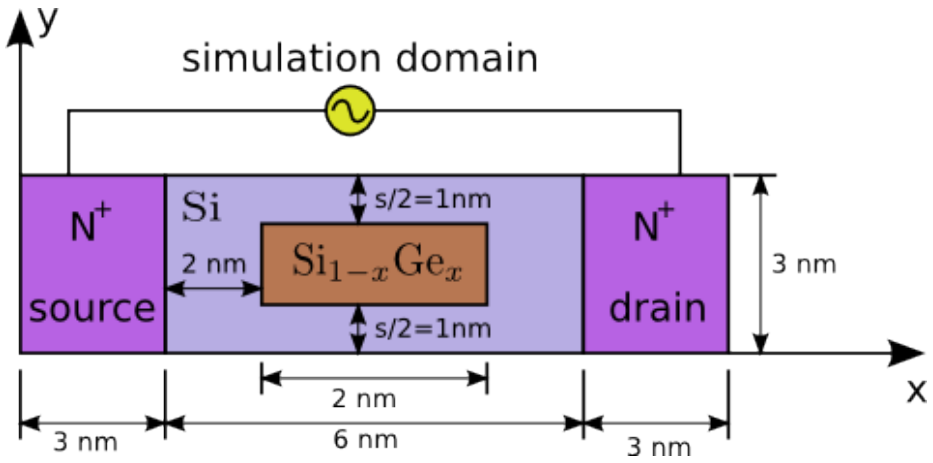

Figure 3.3: The simulation domain for $Si/Si_{1-x}Ge_x$ nanocomposite thin film.

In this part, we first calculate the electron transport properties of the $Si_{1-x}Ge_x$

nanocomposite thin-films under unstrained condition. We start with a $Si_{1-x}Ge_x$ nanowire composite thin-film with dimensions shown in Fig. (3.3), and then increase the height of the nanowire (i.e. reduce the distance s between the nanowires) to reach the limiting case in which the nanocomposite thin film becomes a superlattice. Note that, although the particular composition and geometry of the thin film is chosen here to demonstrate the effect of strain on the electrical transport in thin-film nanocomposites, the analysis approach is general. It is straightforward to apply this approach to study other types of nanocomposite materials with different dimensions. As an example of the computed solutions of the conduction band edge and electron density in the thin films, Fig. (3.4a) shows the results for a $Si_{0.2}Ge_{0.8}$ thin film with a doping density of $10^{18}cm^{-3}$ and $V_d = 0.01$V . Note that, for the clarity of the plots, the electron density is shown in Fig. (3.4b) for the $Si_{0.2}Ge_{0.8}$ region (in the range $x = 5\text{nm} \sim 7\text{nm}$). Fig.(3.5) shows the conduction band edge of the nanocomposite thin film along line $y = 1.5$ nm as a function of applied voltage. It is shown in Fig. (3.4a) and Fig. (3.4b) that the quantum tunneling effect plays an important role in the electron transport. A potential barrier is initially built along the interfaces of the thin film and the source and drain contacts due to the difference in the doping density. Within the thin film, another potential barrier is built due to the conduction band discontinuity between Si and $Si_{0.2}Ge_{0.8}$, as shown in Fig. (3.5). Since the transport within the material is ballistic, the resistance of the material comes from both the source and drain contact interfaces [28] and the potential barriers standing in the path of electron transport. Fig. (3.5) shows that when the applied voltage increases, the downward shifting Fermi level in the drain contact leads to an increasing slope of the conduction band edge toward to the drain.

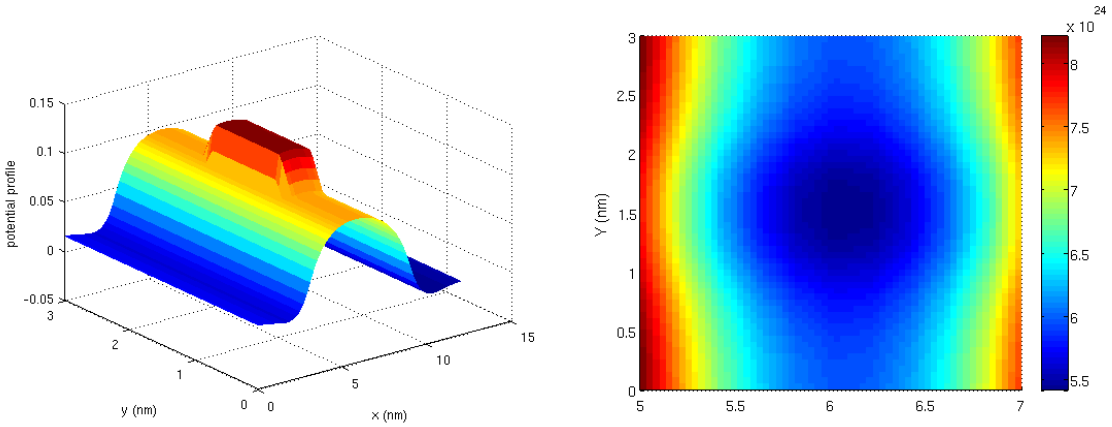

(a) (b)

Figure 3.4: (a)The conduction band edge in the thin film, and (b)the electron density within $Si_{0.2}Ge_{0.8}$ region.

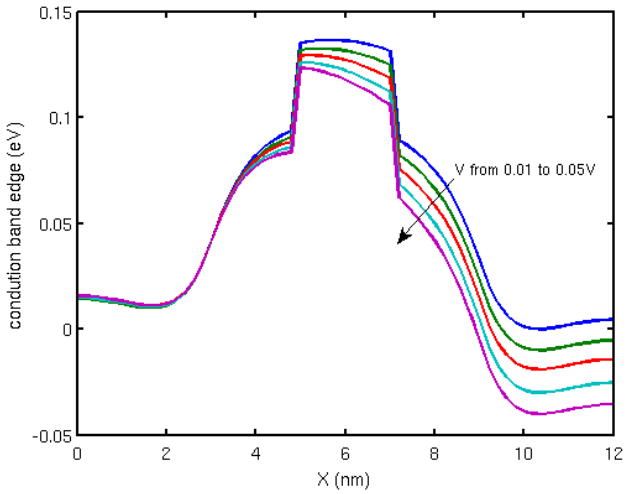

Figure 3.5: Conduction band edges along y = 1.5nm.

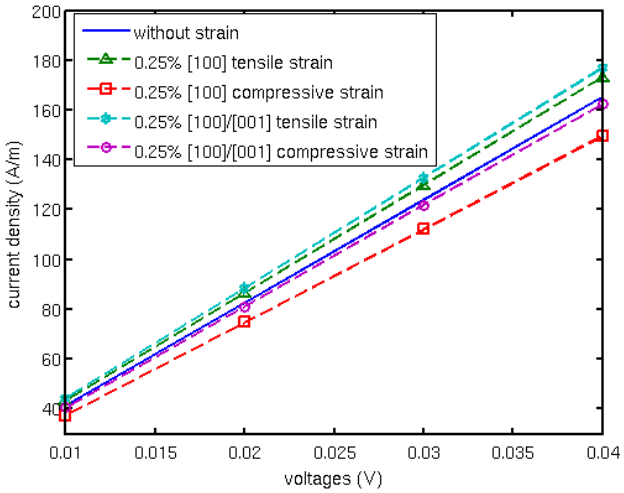

Figure 3.6: IV curve variation due to applied strains.

Next, three types of strains are applied to the thin film: (1) uniaxial strains in [100] direction (x-direction), (2) biaxial strains in [100]/[001] directions (x/z-directions) and (3) biaxial strains in [100]/[010] directions (x/y-directions). Note that, although the thickness of thin films is only several nanometers, it is technologically feasible to apply strains in the thickness direction [40]. Fig. (3.6) shows the variation of the IV curve due to uniaxial and biaxial strains. Fig. (3.7) and Fig. (3.8) show the variation of the conduction band edges in [100], [010] and [001] directions along the line $y = 1.5$nm in the thin film subjected to uniaxial (Fig. (3.7)) and biaxial (Fig. (3.8)) strains for $Si/Si_{0.2}Ge_{0.8}$, note that the same trend can be observed in other $Si/Si_{1-x}Ge_x$ systems with different Ge content. In the figures, E_{cx}, E_{cy} and E_{cz} denote the conduction band edges in [100], [010] and [001] directions, respectively. As the variation of conduction band edges under [100]/[001] strains is similar to that under [100]/[010] biaxial strains, only the former is presented. It is shown that there are two simultaneous changes of the electronic band structure. First, the band degeneracy of both Si and $Si_{0.2}Ge_{0.8}$ in $\langle 100 \rangle$ directions is broken by applied strains. When a uniaxial tensile strain is applied in [100] direction, the conduction band edges in [010]

and [001] directions shift down while the conduction band edge in [100] direction shifts up. The originally degenerate conduction band is split into Δ_2 and Δ_4 bands. When a [100]/[001] biaxial tensile strain is applied, the conduction band edge in [010] direction shifts down and the band edges in [100] and [001] direction shift up. Similarly, a [100]/[010] biaxial tensile strain lowers the conduction band edges in [001] and lifts the ones in [100] and [010] directions. Since electrons are more easily populated in the valleys with lower conduction band edges, and the electron mobility in [010] and [001] valleys is higher due to its relatively lower conductivity effective mass in the x-direction, higher electron occupancy in lowered [010] or [001] valleys enhances electron transport in x-direction. Second, due to the band shift difference in Si and $Si_{0.2}Ge_{0.8}$ regions, the band offset at Si and $Si_{0.2}Ge_{0.8}$ interfaces also varies with applied strain. As shown in Fig. (3.7) and Fig. (3.8), the band offset is reduced with compressive uniaxial and biaxial strains while it is increased with tensile strains. For example, under 1% [100]/[001] biaxial compressive strain, the band offset in [100] and [001] directions becomes quite small, effectively removing the potential barrier induced by the nanowire.

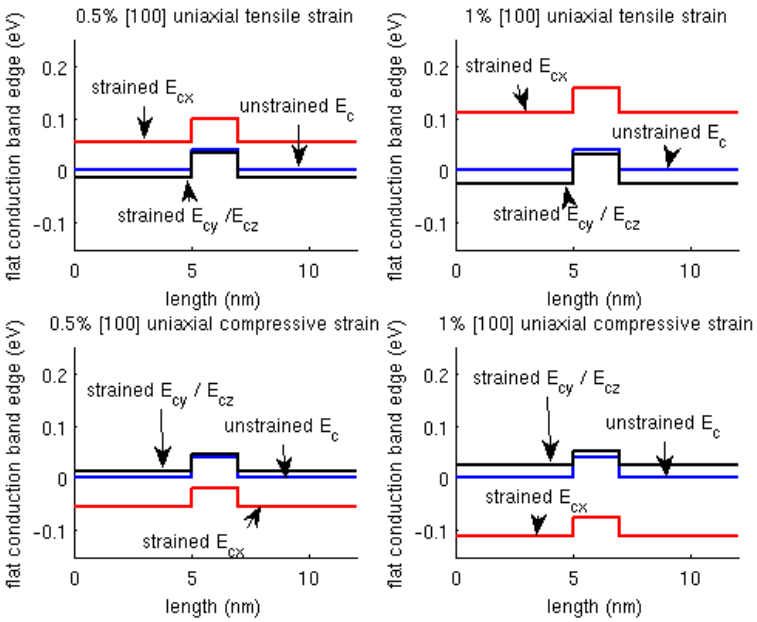

Figure 3.7: Electronic band structure variation in the nanocomposite thin film under uniaxial strains. The flat band edges are the strain-induced initial band shift in Si (left), $Si_{0.2}Ge_{0.8}$ (middle) and Si(right) regions. E_{cx}, E_{cy} and E_{cz} denote the conduction bands in x, y and z directions after the shift.

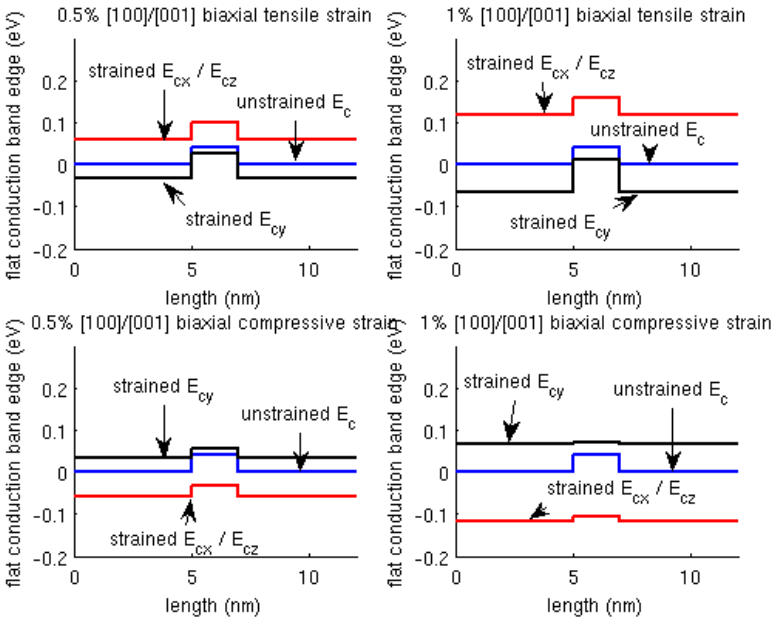

Figure 3.8: Electronic band structure variation in the nanocomposite thin film under biaxial strains.

The new locations of the conduction band edges and band offsets are then used in the self-consistent solution of NEGF and Poisson equations. The shift of energy bands and change of band offsets is included in the Hamiltonian as shown in Eq. (3.2). Fig. (3.9) shows the computed electrical conductivities of a set of $Si/Si_{1-x}Ge_x$ nanocomposite thin films with [100] uniaxial, [100]/[001] biaxial and [100]/[010] biaxial strains. As shown in the figures, with different Ge content in $Si_{1-x}Ge_x$ alloys, the electrical conductivities decrease as Ge content increases. This is due to the increase of band offset built between Si and $Si_{1-x}Ge_x$. The band offset increase lifts the energy levels within the nanowire region. Therefore, the electron density in this region is reduced. Because of the decrease in the number of carrier densities for the current transport, the current density is decreased, resulting in a lower electrical conductivity. It is also observed that while the value of electrical conductivity depends on the Ge content, the variation of the electrical conductivity with the applied strains shows similar patterns for different Ge content. Fig. (3.10) shows the effect of doping density on the electrical conductivity of $Si/Si_{0.2}Ge_{0.8}$ thin films with uniaxial and biaxial strains. The doping density is varied from $5 \times 10^{17} cm^{-3}$ to $10^{19} cm^{-3}$. It is shown that the electrical conductivity increases significantly with increasing doping density. However, similar variations of the electrical conductivity with the applied strains are observed for different doping densities.

To better understand the mechanisms leading to the variation of electrical conductivity with different strains, we take Ge content $x = 0.8$ and a doping density of $10^{18} cm^{-3}$ as a specific case to analyze the strain effects in details. Fig. (3.11) shows the electrical conductivity of a $Si/Si_{0.2}Ge_{0.8}$ nanocomposite thin film with the dimensions shown in Fig. (3.3) as a function of externally applied strains. Note that the [010]/ $\pm$ 0.5%[100] biaxial strains shown in the figure denote a 0.5% tensile or compressive [100] strain combined with a varying [010] strain. A significant effect

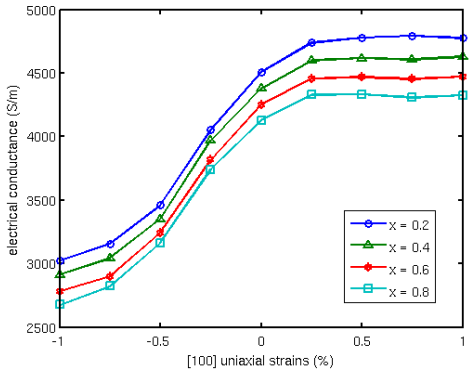

(a)

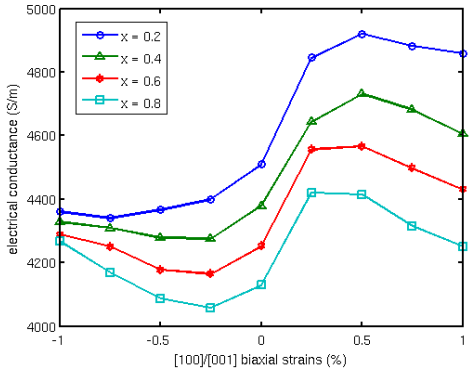

(b)

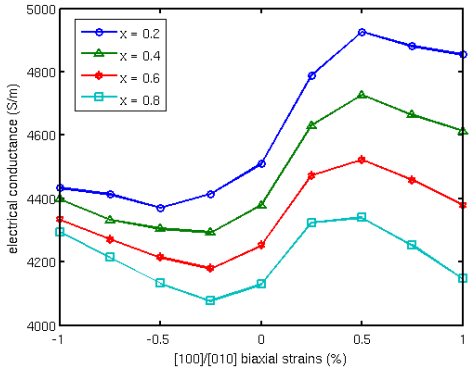

(c)

Figure 3.9: Effect of Ge content on the electrical conductivity of $Si/Si_{1-x}Ge_x$ nanocomposite thin films under (a) [100] uniaxial strains, (b) [100]/[001] biaxial strains, and (c) [100]/[010] biaxial strains.

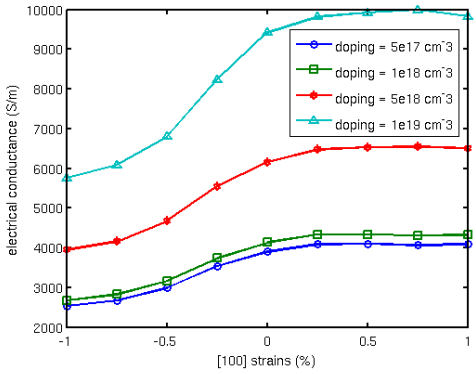

(a)

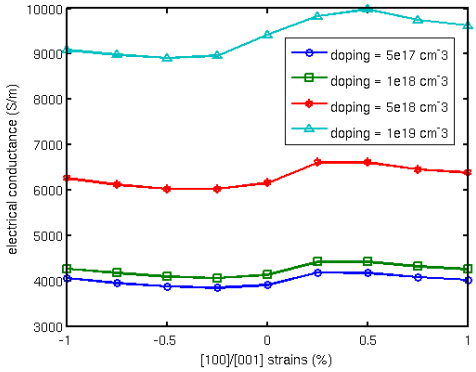

(b)

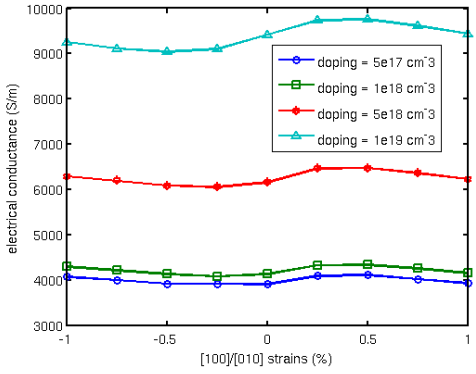

(c)

Figure 3.10: Effect of doping density on the electrical conductivity of $Si/Si_{1-x}Ge_x$ nanocomposite thin films under (a) [100] uniaxial strains, (b) [100]/[001] biaxial strains, and (c) [100]/[010] biaxial strains.

of the strains on the electrical conductivity is observed for the nanocomposite thin film. With [100] uniaxial, [100]/[001] and [100]/[010] biaxial tensile strains, the electrical conductivity of the $Si_{0.2}Ge_{0.8}$ nanocomposite is improved, but in a nonlinear fashion. The increasing rate of the electrical conductivity of the thin film reduces when the tensile strains increase. A significant decrease in electrical conductivity is observed for compressive [100] strain while the trend of $[010]/-0.5\%[100]$ strain is the opposite. Next, we investigate the effect of the nanowire size. The height of the $Si_{0.2}Ge_{0.8}$ nanowire shown in Fig. (3.3) is increased and the strain effect on the electrical conductivity is calculated for the different nanowire sizes. Fig. (3.12) shows the limiting case when the height of the nanowire is approaching $3nm$, i,e, the space between the nanowires in the thin film reducing to zero and the thin film is becoming a superlattice. It is shown that, while the electrical conductivity variation characteristics are similar as the height of the $Si_{0.2}Ge_{0.8}$ nanowire increases, the rate of variation becomes more significant. In addition, the overall electrical conductivity of the thin film becomes smaller due to the increase in nanowire size.

The exhibited characteristics of the electrical conductivity variation can be attributed to the combined effects of (1) the strain-induced band splitting of the conduction band edges, (2) the strain-induced change of band offset, (3) electron quantum effect due to the $Si_{0.2}Ge_{0.8}$ nanowire and (4) the size of the $Si_{0.2}Ge_{0.8}$ nanowire. To better understand the behavior of the electrical conductivity of the nanocomposite thin film under the external strains, the variation of electron population in the thin film is studied in detail. Percentages of electron contribution to the total electron density from different valleys are obtained under different strain conditions, as shown in Fig. (3.13). We first observed that, in the unstrained case, the electron contributions from [100], [010] and [001] valleys are quite close.

This is due to the fact that the thin film is connected to the source and drain in the x-direction (thickness direction), and its dimensions are large in both y- and z-directions. Electrons are not tightly confined in all three directions. The $3D$ density of states in [100], [010] and [001] valleys are quite similar when no strain is applied. Second, when [100] uniaxial tensile strains are applied, the conduction band edges of [010] and [001] valleys shift down as shown in Fig. (3.7), leading to more electrons populated in those valleys. It is shown in Fig. (3.13a) that the electron contributions from [010] and [001] valleys increase to 49.5% and 45.8%, respectively. Meanwhile, the electron contribution from [100] valleys decreases to 4.7%. Since, as discussed in Section 3.2.2, higher electron density in [010] and [001] valleys is advantageous for the electrical conductivity of the thin film, the electrical conductivity increases with [100] uniaxial tensile strain. For the [100]/[001] and [100]/[010] biaxial tensile strains, the increase of electrical conductivity comes from the large downward shift of band edges of high-mobility [010] and [001] valleys, respectively. Nevertheless, the [100]/[001] biaxial tensile strain gives a little larger electrical conductivity increase than the [100]/[010] biaxial tensile strain, as shown in Fig. (3.11). This is due to the quantum confinement effect introduced by the band offset produced by the $Si_{0.2}Ge_{0.8}$ nanowire. It should be kept in mind that the difference is small as the potential barrier height in our case is relatively small ($<$0.1 eV). This can be shown in the superlattice case where the material structure becomes equivalent in y- and z-directions. In this case, valleys in [010] and [001] are degenerate, and the [100]/[010] and [100]/[001] biaxial strains work the same. Another observed effect is that the electrical conductivity of the $Si/Si_{0.2}Ge_{0.8}$ thin film does not improve further when the [100]/[010] biaxial tensile strain reaches beyond 0.25%. As shown in Fig. (3.13b) and Fig. (3.13c), with 0.5% [100]/[001] and [100]/[010] biaxial tensile strains, more than 93% and 92% of the electrons are

already located in [001] and [010] valleys, respectively. When the biaxial strains increase, further increase in [001] or [010] valley electron occupancy is limited. However, as shown in Fig. (3.8), the band offset between Si and $Si_{0.2}Ge_{0.8}$ continues to increase linearly with the strain, impairing the electrical conductivity improvement from the increase of occupancy in [001] and [010] valleys.

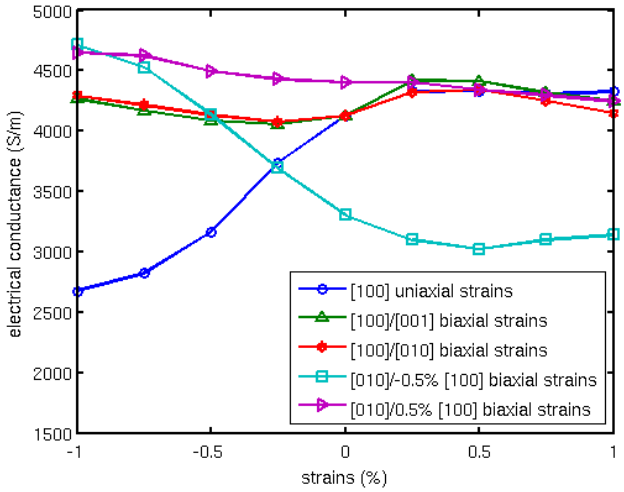

Figure 3.11: Electrical conductivity variation of the nanocomposite thin film due to externally applied strains.

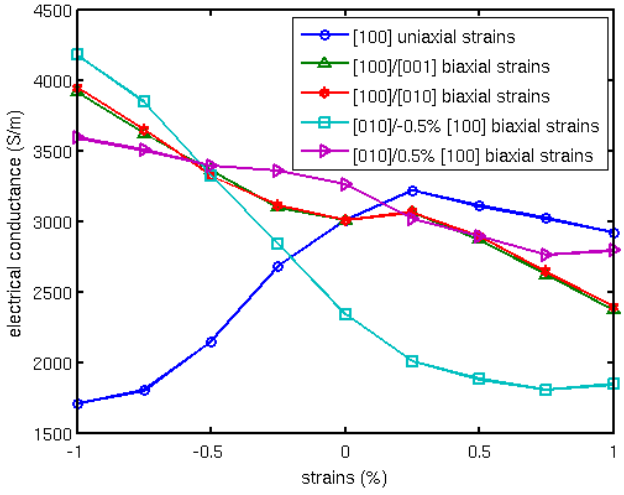

Figure 3.12: Electrical conductivity variation: the limiting case of superlattice.

The combined effect of band-splitting and band-offset on the electrical conductivity is

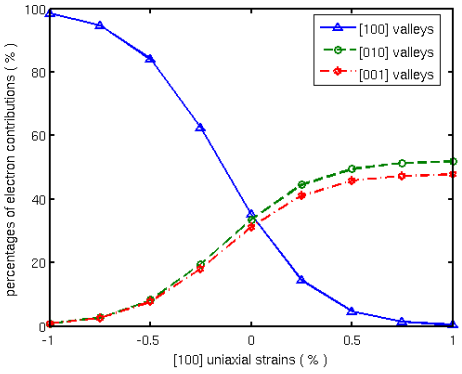

(a)

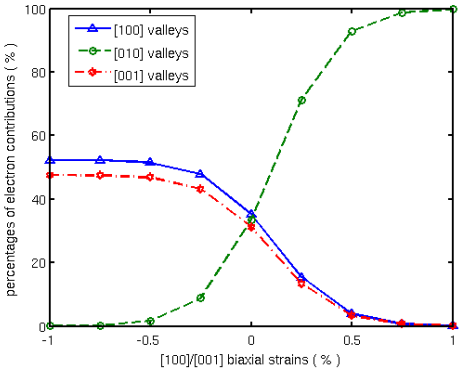

(b)

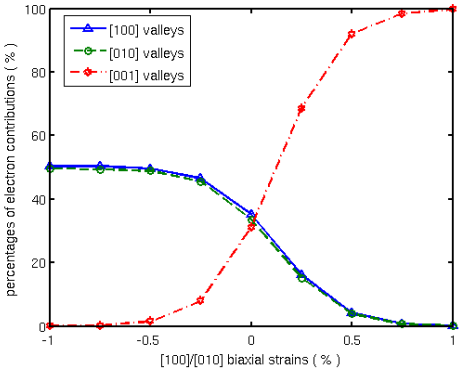

(c)

Figure 3.13: Percentage of electron contribution from the different valleys under (a) [100] uniaxial strains, (b) [100]/[001] biaxial strains, and (c) [100]/[010] biaxial strains.

also evident for compressive strains. When [100] uniaxial compressive strain is applied, the conduction band edge of [100] valleys shifts down while the conduction band edges of the other two valleys shift up (Fig. (3.7)), resulting in less electrons in [010] and [001] valleys (Fig. (3.13a)) and lower electrical conductivity in the thin film (Fig. (3.11)). For the [100] uniaxial compressive strain, the band-splitting effect is more significant than that of the band offset decrease. When the [100]/[001] biaxial compressive strain is applied, the electrical conductivity first decreases then increases. This behavior can be attributed to the simultaneous decrease of band offsets and the increase of electron density in [001] and [100] valleys due to band splitting. When the compressive stain is small, the increased electron contribution in [100] and [001] valleys leads to a reduction in electrical conductivity. As the compressive strain increases, the increase of electron contribution in [001] and [100] valleys becomes limited (Fig. (3.13b)) while the band offset height keeps lowering, leading to an increase of electrical conductivity in the thin film. Similar behavior is observed in [100]/[010] biaxial compressive strain case.

3.4 Summary

In this chapter, a computational approach for calculating the electrical conductivity of strained semiconductor nanocomposite thin films is proposed. The effect of uniaxial and biaxial strains on the electrical conductivity of $Si/Si_{1-x}Ge_x$ nanocomposite thin films is computed. The effect of strains on the band structures of the nanocomposite thin films is calculated with a degenerate two-band $k \cdot p$ theory. The electrical conductivity of the thin films is computed by using a $2D$ real-space Non-Equilibrium Green's Function approach coupled with the Poisson Equation. Numerical results demonstrate that the external strains have a significant influence on the electrical conductivity of the nanocomposite thin films. The

electrical conductivity can be increased by as much as 40% in the superlattice case. The electrical conductivity variation of the nanocomposite thin films can be attributed to combined effects of strain-induced splitting of the conduction band edges and change of band offsets, electron quantum confinement, and size of the $Si_{1-x}Ge_x$ nanowires. Evidently, externally applied strain should be included as a design parameter and, possibly, a control mechanism of electron transport in the development of flexible electronic devices.

CHAPTER 4

COMPUTATIONAL MODELING AND ANALYSIS OF THERMOELECTRIC PROPERTIES OF NANOPOROUS SILICON

4.1 Introduction

Thermoelectric materials enables direct conversion of heat energy into electricity in a clean, economical and sustainable fashion. They offer great potential in applications such as power generation, cooling systems and waste heat recovery [19–21]. However, the current difficulty in massive application of thermoelectric materials lies in their relatively low conversion efficiency [22, 23]. The efficiency of thermoelectric materials is evaluated by the dimensionless figure of

merit $ZT = S^2\sigma T/k$, where σ is the electrical conductivity, S is the Seebeck coefficient, k is the thermal conductivity contributed from both electrons k_e and phonons k_p, and T is the temperature. The product of $S^2\sigma$ is called the power factor. To increase ZT, thermoelectric materials with lower k and higher power factor are preferred. Many approaches have been proposed to increase ZT in the literature. It has been demonstrated that the ZT of compound semiconductors such as Bi_2Te_3 can reach 1.0 [115]. The relatively high ZT of Bi_2Te_3 is attributed to the large atomic masses of Bi and Te, which lead to a low thermal conductivity. Another option to increase ZT is to reduce the dimensions of the thermoelectric materials. With the help of quantum confinement effects, superlattices and quantum dots have demonstrated superior performance in experiments. For example, Bi_2Te_3/Sb_2Te_2 thin film superlattices have ZT up to 2.0 [24]. ZT of embedded $PbSeTe$ quantum dots was reported to be larger than 1.0 [25]. One-dimensional semiconductor materials such as Si and Bi nanowires have also been investigated extensively [26, 116]. It was reported that Si nanowires with diameter ranging from $10nm$ to $20nm$ show a high ZT up to 1.0 [10]. The increase of ZT in nanowires is a result of the large reduction in their thermal conductivity, which is considered due to surface roughness and phonon drag effect. More recently, it has been shown that nanostructured materials such as $SiGe$ nanocomposites have a good thermoelectric performance with ZT reaching 1.5 [9, 117]. The mechanism driving the improvement of ZT in those materials mainly lies in the large reduction of their thermal conductivity due to significant grain boundary phonon scattering. While the potential is promising, the obstacles of large scale application of those thermoelectric materials are the limited resources and high-cost fabrication processes. Porous Si has been proposed to be an efficient thermoelectric material ever since it is found to have very low thermal conductivity [57]. As nano-sized

pores become achievable in fabrication of porous Si, it has been shown experimentally that the ZT of p-type porous silicon with 35% porosity can reach up to 0.4 [118] at room temperature. Moreover, it is predicted theoretically by using molecular dynamics and ab initio density functional theory that the ZT of n-type nanoporous silicon with pore size of $1nm \times 1nm$ can reach around 1.0 [119]. Compared with other thermoelectric materials, nanoporous silicon has two major advantages: first, Si is an abundant resource on earth and has simple and economical fabrication processes; and second, from device fabrication perspective, connecting nanoporous Si to electrical leads is more straightforward than attaching low-dimensional materials such as nanowires to the external leads. While the design, optimization, and fabrication of nanoporous Si for thermoelectric applications can be accelerated through computational analysis of the material, numerical study on the thermoelectric properties of nanoporous silicon is still quite limited. How the thermoelectric performance is influenced by factors such as the porosity, temperature, doping density and pore size remains unclear.

In this chapter, for computational analysis of thermoelectric properties of nanoporous silicon, we present a comprehensive computational approach combining non-equilibrium Green's function (NEGF)-Poisson equation [49, 120] for electrical transport calculation and phonon Boltzmann transport equation (BTE) [39] for phonon thermal transport calculation. To the authors' best knowledge, this is the first time that a complete continuum-level computational approach is proposed and applied in the investigation of the thermoelectric performance of nanoporous Si. The NEGF-Poisson model is solved self-consistently by using the finite difference method (FDM) to numerically calculate the electrical conductivity and Seebeck coefficient of the material while the phonon BTE is solved by using the finite volume method (FVM) to obtain the phonon thermal conductivity. Meanwhile, the

electronic thermal conductivity is obtained by using the Wiedemann-Franz law [58]. The NEGF-Poisson model used in this chapter has been successfully applied in electrical transport analysis of various nanodevices and nanomaterials [27, 120, 121]. Results in the literature show that it can well capture the quantum effects including tunneling and quantum confinement in nanoscale semiconductor materials and devices. It is also demonstrated in this chapter that the numerical results for the electrical conductivity and Seebeck coefficient match well with the published experimental results [121]. The phonon BTE has been applied to phonon thermal transport analysis for many nanostructured materials with demonstrated accuracy and efficiency [122–124]. Once the electrical conductivity, the Seebeck coefficient and the thermal conductivity are obtained, the figure of merit, ZT, is obtained straightforwardly. By using the model, the effects of porosity, size of nanopores, temperature and doping density on the thermoelectric properties of nanoporous silicon are investigated. Optimal combination of the parameters for a better thermoelectric ZT of nanoporous Si is also studied. The rest of the chapter is organized as follows. The computational models and their implementations are described in Section 4.2. In Section 4.3, simulation results and parametric studies are presented for the thermoelectric properties of nanoporous Si. Finally, the summary is given in Section 4.4.

4.2 Theoretical Model and Computational Procedures

4.2.1 Nanoporous Silicon

Fig. (4.1) shows the nanoporous silicon material used in our study. The nanoscale pores are assumed uniformly distributed in the silicon host material. Due to the uniform arrangement of the pores, a unit cell is taken from the material as the computational domain. As shown in the figure, L, W, pl and pw denote the length and the width of the unit cell and the pore, respectively. The porosity is calculated by the ratio between the porous area and the unit cell area, that is, $P = (pl \times pw)/(L \times W)$. The Cartesian x and y directions are assumed to be aligned with the [100] and [010] directions of the crystal lattice, respectively. In this chapter, the in-plane (x-y plane) thermoelectric properties (electrical conductivity, Seebeck coefficient, thermal conductivity and figure of merit) are investigated. The periodic property of the unit cell is used in solving both NEGF and phonon BTE. Details of the thermoelectric analysis are presented in the following sections.

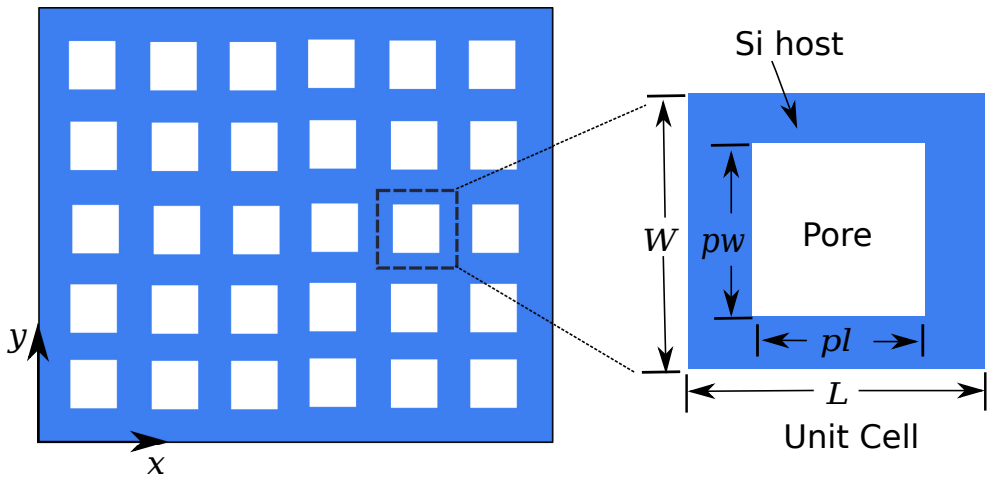

Figure 4.1: Left: nanoporous silicon; right: the unit cell taken for computational analysis.

4.2.2 Electrical Conductivity

To numerically measure the current flow in the unit cell, two semi-infinite electron reservoirs, namely, source and drain, are attached to the unit cell. The current flow in the simulation domain due to an applied voltage or a temperature difference between the left and right ends is solved by using a $2D$ real-space NEGF formulation coupled self-consistently with the Poisson equation. The basic material parameters for Si used in the calculations are as follows: the permittivity of silicon is taken as $11.7\varepsilon_0$, where ε_0 is the permittivity of free space. The longitudinal and transverse effective masses for silicon are $m_l = 0.92m_e$ and $m_t = 0.19m_e$, respectively, where m_e is the free electron effective mass. All the three different pairs of valleys in silicon are considered. N-doped Si is considered in this chapter, hole transport is not included. The real space NEGF formulation is obtained from the two dimensional effective mass Schrödinger equation which is given by Eq. (2.1). By discretizing the domain into a uniform grid, through the finite difference method, the Schrödinger equation can be expressed in a matrix form as,

$$\mathbf{H}(x, y)\boldsymbol{\psi} = E\boldsymbol{\psi} \tag{4.1}$$

where E is the energy in the x-y plane. In the z direction, the depth of the material is assumed to be very large, the plane wave condition can therefore be applied. The total energy of the system is expressed as $E_{total} = E+E_z$, where E_z is the continuous energy in the z direction. In addition, periodic boundary condition is applied on the top and bottom edges of the $2D$ domain in obtaining the Hamiltonian matrix in Eq. (4.1). By definition, the retarded $2D$ real-space NEGF can be expressed as Eq. (3.9), with the introduction of self-energy functions for source and drain contacts, the retarded real-space NEGF can be rewritten as Eq. (3.10). Note that, the tunneling through

the pores is not included in our calculation. In this chapter, we apply a hard-wall boundary condition on the interface between the pore and silicon host material when composing the system Hamiltonian. In other words, an infinite potential barrier is assumed within the pore region. When the electron transport is ballistic, $\hat{\mathbf{H}}(x, y)$ can be easily obtained without considering any other perturbation sources in addition to source and drain contacts. However, if the scattering within the simulation domain can not be ignored, Eq. (3.10) must be modified to include the scattering effects. In this chapter, to account for electron scattering, the Büttiker probes, which have been successfully used to model dissipative electron transport in electrical transistors [120], are adopted. In the scattering model, a set of probes are introduced to model the scattering effects on the charge carrier transport within the material. The probes are treated like source and drain contacts but with fundamental differences on how they perturb the Hamiltonian. The source and drain contacts inject or extract electrons from the channel materials, resulting in a current flow in the channel. However, the Büttiker probes only change the energy/momentum of the electrons without changing the number of electrons in the channel material. The probes' perturbation to the Hamiltonian is also introduced by self-energy matrices. The modified retarded real-space NEGF in Eq. (3.10) can be written as,

$$\mathbf{G}(E) = [(E + j\gamma)\mathbf{I} - \hat{\mathbf{H}}(x, y) - \mathbf{\Sigma}]^{-1} \tag{4.2}$$

where $\mathbf{\Sigma}$ is the sum of self-energy matrices from the source and drain contacts and the Büttiker probes. Assuming the simulation domain is discretized into $N_x \times N_y$ grid points and the x direction is the transport direction, the first and last column of the grid points are the source and drain contacts, respectively, and each of the remaining $(N_x - 2)$ grid-point columns is attached to a Büttiker probe. The strength of the

scattering perturbation depends on the coupling strength associated with the probes. The electrons are perturbed more as the coupling strength increases. In this chapter, a model presented in Ref. [125] relating the electron mobility in the material to the coupling strength is exploited. The relation between the electron mean free path and the coupling strength of probes is given by

$$\lambda = 2\Delta x \frac{t_x^2}{t_i^2} \tag{4.3}$$

where λ is the mean free path of electrons and t_i is the coupling strength of for the i-th probe. To calculate the electron mean free path, the relation between the low field mobility and the mean free path is [120, 125],

$$\xi = \lambda \sqrt{\left(\frac{e^2}{2\pi k_B T m_x^*}\right)} \frac{F_{1/2}(E_{fi} - U_i) F_{-1}(E_{fi} - U_i)}{F_0^2(E_{fi} - U_i)} \tag{4.4}$$

where e is elementary charge, T is the temperature, ξ is the low field mobility of the material which can be obtained from experimental data, E_{fi} is the Fermi level of a certain probe i and k_B is the Boltzmann constant. F_0, F_{-1} and $F_{1/2}$ are the Fermi Dirac integrals of order 0, -1 and $1/2$, respectively. Once the coupling strength t_i is obtained (note that t_i needs to replace t_x in the coupling matrix in Eq. (3.12) with Büttiker probes), the self-energy matrices for source, drain and Büttiker probes can be calculated following the procedures described from Eq. (3.11) to Eq. (3.18). The self-energy matrices are also used to obtain the broadening functions for all the reservoirs (i.e. source, drain and Büttiker probes). The broadening function for i-th reservoir is

$$\mathbf{\Gamma}_i = j[\mathbf{\Sigma}_i - \mathbf{\Sigma}_i^\dagger] \tag{4.5}$$

where † denotes the Hermitian conjugate and j is the imaginary unit. With the retarded NEGF (Eq. (4.2)) and the broadening matrices (Eq. (4.5)), the spectral functions for the reservoirs can be computed as

$$\mathbf{A}_i = \mathbf{G}\mathbf{\Gamma}_i\mathbf{G}^\dagger \tag{4.6}$$

The correlation function $\mathbf{G^n}(E)$ measuring the contribution from the reservoirs can then be calculated by

$$\mathbf{G^n}(E) = \sum_i \mathbf{A}_i(E)F(E, E_{fi}) \tag{4.7}$$

where the Fermi function $F(E, E_{fi})$ is given by Eq. (3.22). Finally, the local electron density is obtained by Eq. (3.23).

As indicated in Eq. (4.7), to calculate the charge density in the simulation domain, Fermi levels in all the reservoirs have to be obtained. While the Fermi levels of source and drain contacts can be easily defined by the external voltages applied, the Fermi levels in the Büttiker probes have to be calculated numerically. Note that the probes only perturb the electrons' energy/momentum without changing their numbers. Therefore, the net current flow in each probe must be zero, i.e., the current continuity within the simulation domain must be maintained. To relate the current flow to the Fermi levels within each probe, the net current density in a certain reservoir can be written as

$$I^p = \frac{e}{2\pi\hbar}\sum_q \int T^{pq}(E)[F(E, E_{fp}) - F(E, E_{fq})]dE, \tag{4.8}$$

where I^p is the net current density in reservoir p, T^{pq} is the transmission function from reservoir p to reservoir q. Note that q runs over all the reservoirs including the

source and drain contacts. The transmission T^{pq} is defined as

$$T^{pq} = Trace[\mathbf{\Gamma_p G \Gamma_q G}^{\dagger}] \tag{4.9}$$

To ensure the current continuity, the net current density in each probe must satisfy,

$$I^p = 0, \qquad p = 2, 3, ..., N_x - 1 \tag{4.10}$$

The above equation imposes a set of nonlinear constraints on the Fermi levels in the Büttiker probes. In this chapter, the probe Fermi levels are obtained iteratively by using Newton's method. After obtaining the Fermi levels for all the probes, the correlation function can be directly calculated from Eq.(4.7) and the electron density can be obtained by using Eq.(3.23).

After the electron density is obtained, the $2D$ Poisson equation, i.e., Eq. (3.25), is solved to obtain the potential energy in the domain. A self-consistent solution of the electron density and potential profile is obtained by iterating between the NEGF and Poisson equations. Upon convergence of the solution, the current density I from source to drain can be calculated with Eq. (4.8). The flow chart illustrating the solution procedure for the Büttiker probe treatment of scattering is shown in Fig. (4.2). Finally, the electrical conductance of the material is calculated as $G = I/\Delta V$ and the electrical conductivity can be obtained as $\sigma = GL/W$, where L and W are the length and width of simulation domain.

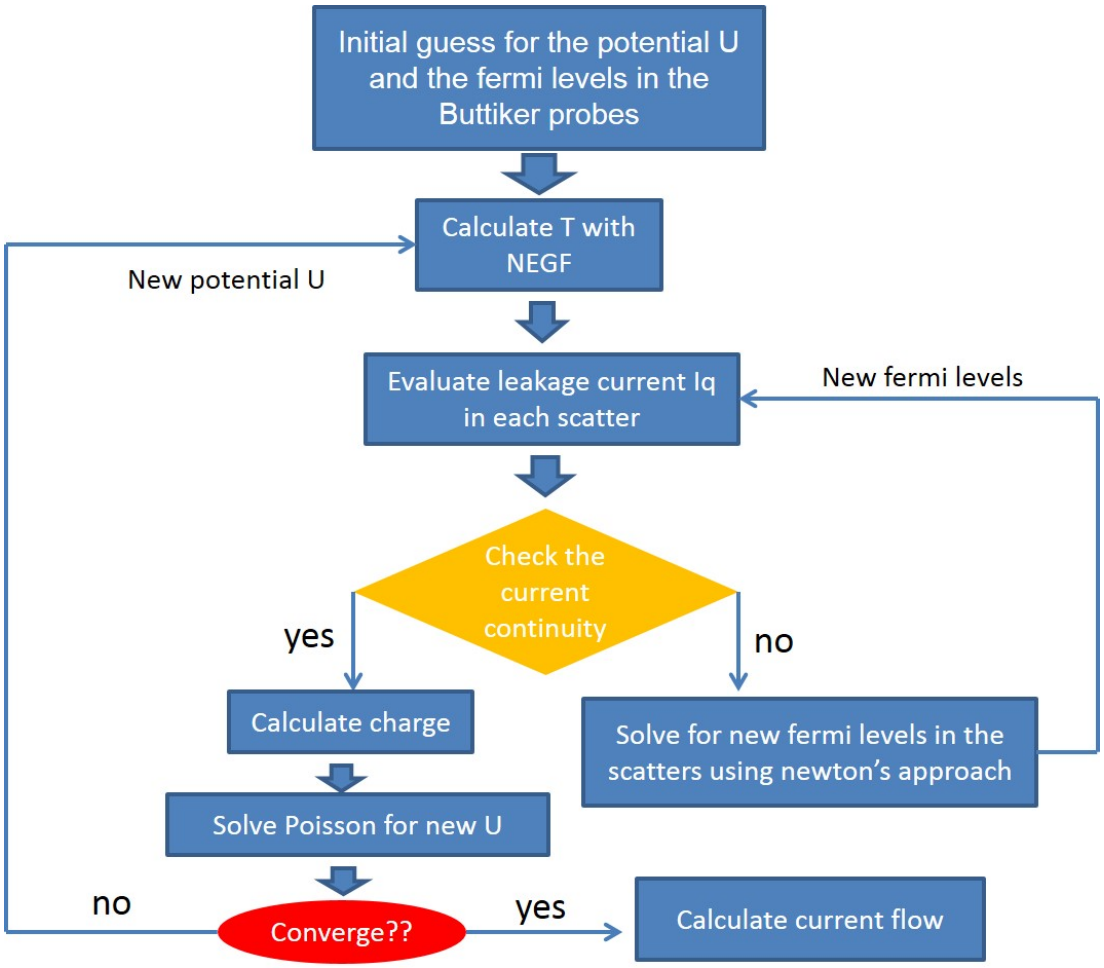

Figure 4.2: Schematic of NEGF algorithm flow.

In the implementation of the computational process described above, a source and drain regions (i.e., reservoirs) need to be attached to the unit cell in order to apply a voltage difference and obtain the current density. In addition, extra silicon regions are added to remove the artificial effect of depletion region caused by the doping difference between the reservoirs and unit cell. To obtain the electrical conductivity of the unit cell, we first attach a source of length (L_s) and a drain of length (L_d) to a silicon region of length ($2 \times L_{Si}$), as shown in the left part of Fig. (4.3). A small voltage difference (ΔV) is applied between source and drain contacts, the current density (I_1) in the domain, denoted as R_1, is calculated by using the NEGF-Poisson

model. The electrical conductance of R_1 is obtained by $G_1 = I_1/\Delta V$. Next the unit cell is inserted in the middle of R_1 and the same voltage difference ΔV is applied between the source and drain, as shown in the right part of Fig. (4.3). The current density (I) and electrical conductance $G = I/\Delta V$ are then calculated for the entire material region. Since $G = G_1G_2/(G_2+G_1)$, the electrical conductance for the unit cell can be obtained as $G_2 = G_1G/(G_1 - G)$. The electrical conductivity of the unit cell is then $\sigma = G_2L/W$. By using the scheme described above, the contact resistances related to the source and drain regions and effects of depletion regions can be effectively eliminated.

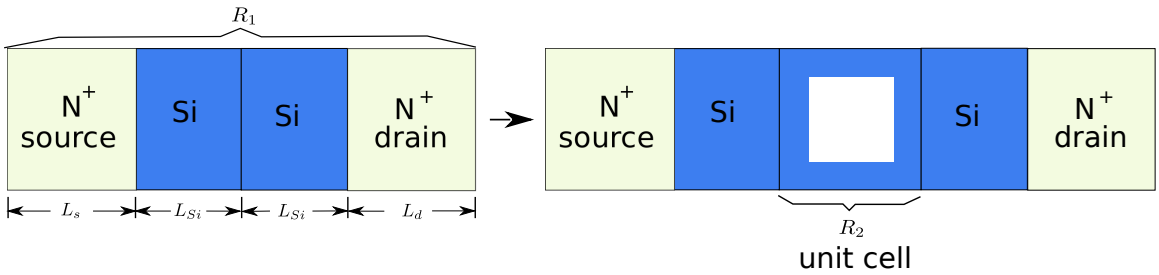

Figure 4.3: Schematic of electrical conductivity calculation of the unit cell.

Fig. (4.4) shows an example of the self-consistent solution of the electron density within the unit cell. In this case, the doping of the unit cell is $10^{19}cm^{-3}$ and the porosity of the unit cell is 6.25%. It is clear that the quantum effect induced by the infinite barrier in the pore region is properly captured. It is important to note that, when the pore size becomes very small, to remove the non-physical quantum effect caused by the small unit cell size in y direction, we include multiple unit cells in y direction to obtain accurate results [126].

4.2.3 Seebeck Coefficient

When a temperature difference is applied between the two ends of a thermoelectric material, different electron energy distributions in the reservoirs

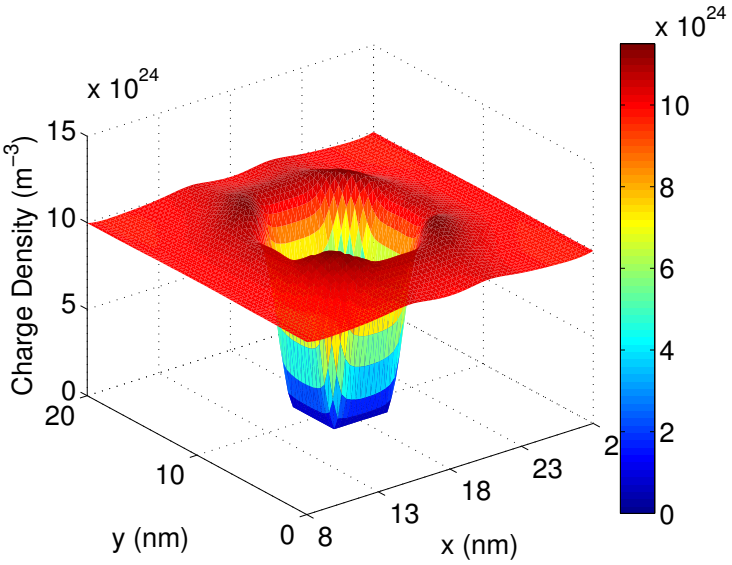

Figure 4.4: The electron density profile within the unit cell.

results in a flow of charge carriers in the material. The direct method to compute the Seebeck coefficient of the material is to calculate the open circuit voltage ΔV caused by a temperature difference ΔT applied at the two ends of the material. By definition, the Seebeck coefficient can then be obtained by $S = -\Delta V/\Delta T$. In this chapter, with conductance of the material calculated as described in Section 4.2.2, the Seebeck coefficient can be computed more conveniently by using an alternative approach [121].

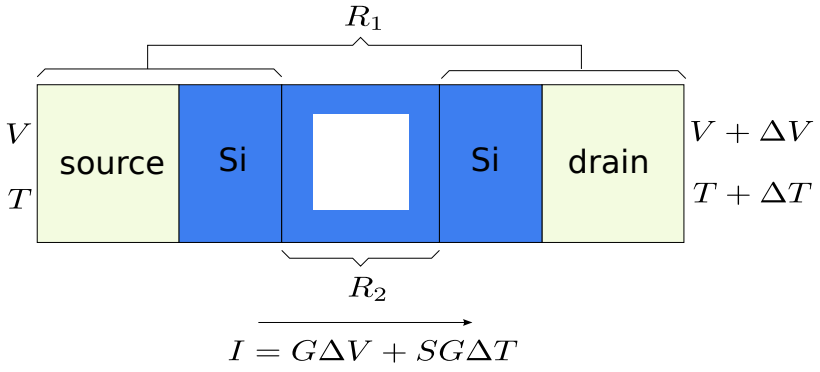

Figure 4.5: Schematic of Seebeck coefficient calculation.

When a temperature and voltage difference, ΔT and ΔV, respectively, are applied between the ends of the source and drain, as shown in Fig. (4.5), the current density can be expressed as [121],

$$I = G\Delta V + SG\Delta T \tag{4.11}$$

Note that G has already been obtained by using the NEGF-Poisson model described in Section 4.2.2. To obtain the S in Eq. (4.11), a temperature difference ΔT is applied across the material while ΔV is kept to be zero. By using the NEGF-Poisson model, the current density I can be calculated, and S can be obtained from $S = I/G\Delta T$. It should be noted that the S obtained is the Seebeck coefficient of the unit cell combined with source, drain and the extra silicon regions. To obtain the Seebeck coefficient of the unit cell itself, further steps are necessary. As shown in Fig. (4.5), the whole simulation domain is divided into two regions: one is composed of source/drain contacts and the extra silicon region (R_1), and the other is the unit cell region (R_2). With the applied $\Delta T \neq 0$, $\Delta V = 0$, and the current continuity conditions, the current density flowing in R_1 and R_2 can be written as,

$$I = S_1 G_1 \Delta T_1 + G_1 \Delta V_1 = S_2 G_2 \Delta T_2 + G_2 \Delta V_2 \tag{4.12}$$

where indexes 1 and 2 denote R_1 and R_2, respectively. In addition, the following equations can be readily obtained,

$$\Delta T = \Delta T_1 + \Delta T_2 \tag{4.13}$$

$$\Delta V = \Delta V_1 + \Delta V_2 = 0 \tag{4.14}$$

Combining Eqs. (4.12-4.14), one can obtain

$$I = \frac{G_1 G_2 (S_1 \Delta T_1 + S_2 \Delta T_2)}{G_1 + G_2} \tag{4.15}$$

Knowing $I = SG\Delta T$, Eq. (4.15) can be rewritten as

$$S = \frac{S_1 \Delta T_1 + S_2 \Delta T_2}{\Delta T} \tag{4.16}$$

Equation (4.16) shows that the overall S for the whole region is the average of S values of its components weighted by the temperature drop in each region. Our calculations show that the temperature drop across the simulation domain is approximately linear, except for the regions immediately left and right to the pore along the heat flux direction. Similar temperature profiles have also been obtained for Si/Ge and Bi_2Te_3/Sb_2Te_3 nanocomposites [127] [128]. Moreover, the temperature difference applied between source and drain contacts in the calculation of the Seebeck coefficient is set to be small ($\Delta T = 2K$). Therefore, a linear distribution of temperature is assumed across the whole domain. However, it should be noted as an approximation. Therefore, in Eq. (4.16), ΔT_1 and ΔT_2 are assumed to be linearly proportional to the length of R_1 and R_2, respectively. Next, by using the the NEGF-Poisson model, an additional simulation is performed on the material structure R_1 shown on the left of Fig. (4.3) with a temperature difference ΔT_1 applied at the two ends and $\Delta V_1 = 0$. The current density I_1 flowing through R_1 is computed from the simulation. Note that the electrical conductance G_1 has already been obtained as discussed in Section 4.2.2. Then S_1 can be calculated from the

following relation

$$I_1 = S_1 G_1 \Delta T_1 \tag{4.17}$$

Finally, the Seebeck coefficient for the unit cell, S_2, can be calculated from Eq. (4.16).

4.2.4 Phonon Thermal Conductivity

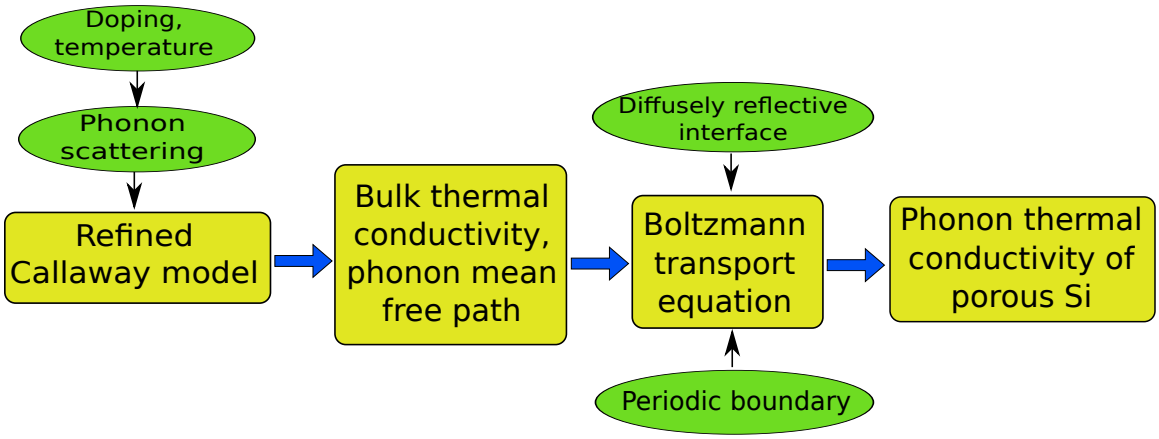

Figure 4.6: Theoretical model and procedure for phonon thermal transport analysis.

In this section, we employ a phonon BTE based approach to compute the phonon thermal conductivity of porous Si, as shown in Fig. (4.6). In this approach, the bulk thermal conductivity of doped Si at various temperatures is computed by a refined Callaway model incorporating various phonon branches and scattering mechanisms. Once the bulk thermal conductivity is computed, the averaged phonon mean free path is calculated by using the kinetic theory. The doping and temperature dependent phonon scattering properties are then incorporated into the BTE to describe the thermal transport in the nanoporous silicon. The diffusive scattering mechanism is adopted for the Si/pore interface and periodic boundary condition is applied to the simulation domain boundary. In the numerical solution of BTE, FVM is used over an unstructured mesh of the domain. Once the solutions are obtained in terms of

the phonon intensity, the thermal conductivity along with heat fluxes and effective temperature profile can be calculated, all of which depend on both doping density and temperature.

The thermal model employed in this chapter is based on a refinement of Callaway's approach [129], which can be characterized by the following: (1) isotropic Debye phonon spectrum with single averaged group velocity per mode is assumed; (2) full Callaway's approach with the correction term k_2 included to account for the fact that phonon normal (N) process plays a role of indirect thermal resistance; (3) relaxation rates τ^{-1} for different phonon scattering mechanisms are empirical, which are dependent on a number of intrinsic factors, such as phonon frequency ω and group velocity v, and extrinsic factors such as doping density n and temperature T; (4) the scattering mechanisms are assumed to be independent of each other and follow Matthiessen's rule; and (5) the phonon thermal conductivity k_{bulk} is calculated by summing the components over all the longitudinal and transverse modes, i.e. [129],

$$k_{bulk} = k_1 + k_2 \tag{4.18}$$

where k_1 and k_2 are defined as,

$$k_1 = \frac{1}{3} \sum_{j=L,T} C_j T^3 \int_0^{\theta_j/T} \frac{\tau_{j,C} x^4 e^x}{(e^x - 1)^2} dx \tag{4.19}$$

$$k_2 = \frac{1}{3} \sum_{j=L,T} C_j T^3 \frac{[\int_0^{\theta_j/T} \frac{\tau_{j,C} x^4 e^x}{\tau_{j,N}(e^x-1)^2} dx]^2}{\int_0^{\theta_j/T} \frac{\tau_{j,C} x^4 e^x}{\tau_{j,N}\tau_{j,R}(e^x-1)^2} dx} \tag{4.20}$$

where $x = (\hbar\omega)/(k_B T)$ is the dimensionless phonon frequency, θ_j/T is the upper limit of dimensionless phonon frequency for the jth mode – longitudinal (L) or transverse

(T), C_j is the phonon specific heat capacity for the j-th mode, expressed by,

$$C_j = \frac{{k_B}^4}{2\pi^2 v_j \hbar^3} \tag{4.21}$$

In Callaway's formulation, $\tau_{j,R}$ contains all the resistive scattering mechanisms. Under the assumption of Matthiessen's rule, it is given by,

$$\tau_{j,R}^{-1} = \tau_{j,U}^{-1} + \tau_{j,I}^{-1} + \tau_{j,B}^{-1} + \tau_{j,e}^{-1} \tag{4.22}$$

where the subscripts U, I, B and e denote phonon-phonon U-process, phonon-impurity, phonon-boundary and phonon-electron interactions, respectively. $\tau_{j,C}$ is the combined relaxation time of $\tau_{j,R}$ and $\tau_{j,N}$ for phonon-phonon N process, which is given by,

$$\tau_{j,C}^{-1} = \tau_{j,R}^{-1} + \tau_{j,N}^{-1} \tag{4.23}$$

In our calculations, common form of U-process and N-process for different phonon modes is adopted [120, 129–131].For N-process,

$$\tau_{T,N}^{-1} = B_{T,N}\omega T^4 \tag{4.24}$$

$$\tau_{L,N}^{-1} = B_{L,N}\omega^2 T^3 \tag{4.25}$$

where $B_{T,N}$ and $B_{L,N}$ represent the strength of scatterings. For U-process, the form of scattering rates for U-process was suggested to be proportional to $T^a e^{(\theta/bT)}$ for both longitudinal and transverse modes [132] as

$$\tau_{T,U}^{-1} = B_{T,U}\omega^2 T e^{(\theta/3T)}) \tag{4.26}$$

$$\tau_{L,U}^{-1} = B_{L,U}\omega^2 T e^{(\theta/3T)} \tag{4.27}$$

The scattering rates due to dopant, Si isotope and other impurities are approximated based on the calculation of scattering rates on point defects as [133],

$$\tau_{j,I}^{-1} = \tau_{j,M}^{-1} + \tau_{j,R}^{-1} \tag{4.28}$$

where $\tau_{j,M}^{-1}$ and $\tau_{j,R}^{-1}$ are the scattering rates due to the substitutional mass of impurity point defects and relative distortion of lattices introduced by impurity atoms, respectively. They are given as,

$$\tau_{j,M}^{-1} = (A_{\delta M} + A_x)\omega^4 \tag{4.29}$$

$$\tau_{j,R}^{-1} = A_R\omega^4 \tag{4.30}$$

where $A_{\delta M}$, A_x and A_R represent the strength of interactions of mass substitution(both dopant and Si isotope atoms), unintentional impurities such as oxygen contamination introduced during fabrication, and lattice distortion, respectively. The analytical form of $A_{\delta M}$ and A_R in Ref. [134] shows that they can be assumed to have a relatively linear dependency on the doping density n. Their values for bulk silicon doped with phosphorus can be found in Table II in Ref. [134]. The scattering rate due to phonon-boundary interaction $\tau_{j,B}^{-1}$ is only included in the thermal conductivity calculation at low temperatures. The boundary scattering effect of the nanoporous Si is treated in the BTE transport model. The scattering rates due to phonon-electron interaction is classified into two scenarios depending on whether the electrons are in non-metallic or metallic state. Non-metallic state electrons are bound to doped or unintentional impurities, whereas metallic state electrons are free electrons in the conduction band. The change from non-metallic state to metallic state occurs when doping density is increased above a critical level,

which is found to be around $3 \times 10^{18} cm^{-3}$ for phosphorus-doped silicon [135] [136]. In this chapter, we focus on heavily phosphorus-doped degenerate silicon (doping density $> 5 \times 10^{18} cm^{-3}$) for thermoelectric energy conversion applications. Consequently, electrons are considered to be in metallic state. In this case, $\tau_{j,e}^{-1}$ can be obtained by using Ziman's phonon-electron scattering rate equation for degenerate semiconductors as [137],

$$\tau_{j,e}^{-1} = \frac{(m_e E_D)^2 k_B T}{2\pi\rho\hbar^4 v_j^2} x_\omega \tag{4.31}$$

where the m_e is the effective mass of electrons, E_D is the deformation potential which is proportional to $\left(N_d^+\right)^{\frac{2}{3}}$ [138], ρ is the mass density of silicon. The parameter values used in our calculations are summarized in Table 4.1.

Table 4.1: Parameters for thermal conductivity calculation of Si.

Threshold θ from phonon dispersion curve [139]	
Transverse	$\theta_T = 240\ K$
Longitudinal	$\theta_L = 586\ K$
Averaged phonon group velocity [139]	
Transverse	$v_T = 5.84 \times 10^3\ m/s$
Longitudinal	$v_L = 8.43 \times 10^3\ m/s$
Three-phonon scattering [139]	
N-process for transverse phonons	$B_{T,N} = 7.1 \times 10^{-13}\ /K^4$
U-process for transverse phonons	$B_{T,U} = 1.0 \times 10^{-19}\ /sK$
N-process for longitudinal phonons	$B_{L,N} = 2.4 \times 10^{-24}\ /sK^3$
U-process for longitudinal phonons	$B_{L,U} = 5.5 \times 10^{-20}\ /sK$
Electronic Scattering [134]	
Effective mass of electron(m_e/m_0	$m_e/m_0 = 0.9, m_0 = 9.1 \times 10^{-31}$
Density	$\rho = 2330\ kg/m^3$

By performing numerical integration over all the phonon modes in Eq. (4.18), the bulk thermal conductivity can be obtained. The averaged phonon mean free path can be calculated using the kinetic theory:

$$\Lambda = \frac{3k_{bulk}}{C^{\alpha}v} \tag{4.32}$$

where v is the sound velocity in Si, $C^{\alpha} = C_T + C_L$ is the acoustic phonon specific heat. Since the optical phonons contribute little to the thermal conductivity for Si due to their small group velocity, they are not taken into consideration. Note that the sound velocity and acoustic phonon specific heat can be calculated by using either lattice dynamics with interatomic potentials [140] or analytical form of summation over the frequency range and phonon modes [141], both of which produce consistent results. In our model, the latter approach is adopted.

After obtaining the bulk mean free path, we solve BTE to obtain the phonon thermal conductivity of nanoporous silicon, and examine the pore size, geometry and boundary condition effects on the thermal conductivity. These effects are considered less frequency-dependent than other scattering mechanism. Furthermore, in this way, such effects are no longer empirical, which are desirable to perform numerical analysis for engineering design purposes. In our analysis, the grey BTE model is adopted, which assumes phonons with an effective group velocity and relaxation rates. For the calculation of cross-plane phonon thermal conductivity, the grey BTE has been demonstrated to be a reasonably good approximation to the frequency-dependent phonon BTE model in the previous works [142] [124]. However, it should be noted that, as a limitation of the grey-BTE model, phonon confinement effect is neglected in the adoption of a single value of relaxation time and group velocity. It has been shown that phonon confinement effect in a free-standing quantum well [143] and

semiconductor nanowires [144] results in modification of phonon dispersion and a reduction in the group velocities and phonon density of states. Thus, the thermal conductivity of nanoporous Si is expected to be further reduced [145], if the phonon confinement effect is properly taken into account.

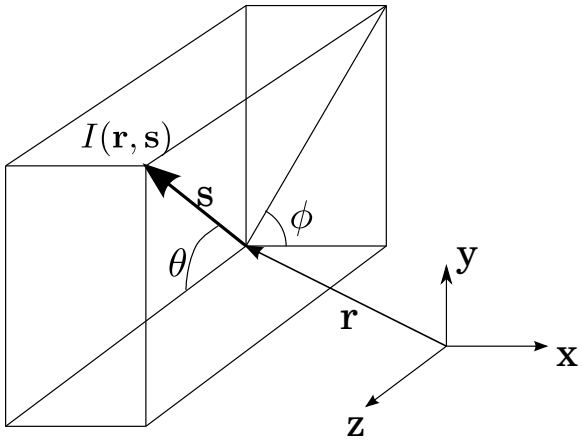

Figure 4.7: Directional phonon intensity.

The governing equation of gray BTE model is given in terms of spatial phonon intensity as [146],

$$\nabla \cdot (I(\boldsymbol{r}, \boldsymbol{s}) \cdot \boldsymbol{s}) = -\frac{I(\boldsymbol{r}, \boldsymbol{s}) - I_0(\boldsymbol{r})}{\Lambda} \tag{4.33}$$

where $I(\boldsymbol{r}, \boldsymbol{s})$ is the total phonon intensity at a spatial position $\boldsymbol{r} = (x, y, z)$ over a path length ds in the direction of unit vector $\boldsymbol{s}$. As shown in Fig. (4.7), $\boldsymbol{s}$ is defined by,

$$\boldsymbol{s} = sin\theta cos\phi \boldsymbol{e}_x + sin\theta sin\phi \boldsymbol{e}_y + cos\theta \boldsymbol{e}_z \tag{4.34}$$

where θ and ϕ are the polar and azimuthal angles, respectively, $\mathbf{e_x}$, $\mathbf{e_y}$ and $\mathbf{e_z}$ is the basis vector set in the Cartesian coordinate system. $I_0(\boldsymbol{r})$ is the averaged equilibrium phonon intensity given by,

$$I_0(\boldsymbol{r}) = \frac{1}{4\pi} \int_0^{2\pi} \int_0^{\pi} I(\boldsymbol{r}, \boldsymbol{s}) sin\theta d\theta d\phi \tag{4.35}$$

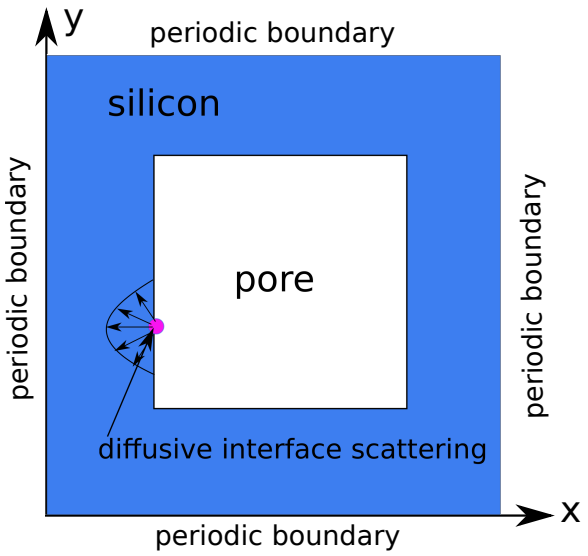

Figure 4.8: Unit cell computational domain for thermal transport analysis.

In this chapter, we adopt the FVM implementation described in Ref. [39] to solve Eq. (4.33).The computational domain is a $2D$ square unit cell shown in Fig. (4.1). Periodic boundary conditions are employed across the outer boundary, and diffusive interface scattering model is employed across the inner porous boundary as shown in Fig. (4.8). Note that, theoretically the effect of surface roughness at the silicon/pore interface on phonon thermal conductivity can be significant for small pore sizes, as shown in Fig. (4.9). However, as discussed in Ref. [127], even one monolayer surface roughness of a silicon lattice would give Ziman's interface specularity parameter$\approx$0, leading to a total diffusive interface condition. For this reason, we adopt a total diffusive phonon scattering condition at the silicon/pore boundary. On the contrary, our results show that the effect of surface roughness on the electron flow is small. This is due to the smaller electron mean free path and the stronger quantum effect over the surface roughness effect when fewer number of subbands conduct [147]. Therefore, the effect of surface roughness on the electrical conductivity is neglected in the simulations. For the top and bottom outer

boundaries, the periodic boundary condition is expressed as,

$$I(x, W, \boldsymbol{s}) = I(x, 0, \boldsymbol{s}), \tag{4.36}$$

for all x and $\boldsymbol{s}$. For the right and left outer boundaries, the periodic boundary condition is expressed as [39],

$$I(0, y, \boldsymbol{s}) - I(L, y, \boldsymbol{s}) = \frac{v_{Si} C_{Si}^{a} \Delta T}{4\pi}, \tag{4.37}$$

where v_{Si} and C_{Si}^{α} are the phonon group velocity and acoustic specific heat of Si, respectively. This additional term on the right hand side of the equation represents an imposed temperature drop ΔT, so that phonon transport can take place along the horizontal direction. The diffusive interface scattering across the inner porous boundary is modeled such that all the directional phonon intensities $I(\boldsymbol{r}, \boldsymbol{s})$ on the inner boundary are reflected and evenly distributed over the solid angles on the Si side, as shown in Fig. (4.8). Further details of the implementation are summarized in Ref. [39]. Once the solution to the BTE is obtained in terms of total phonon intensity $I(x, y, \boldsymbol{s})$. The local effective temperature is calculated as,

$$T(x, y) = \frac{4\pi I_0(x, y)}{C_{Si}^{a} v_{Si}} \tag{4.38}$$

Note that the effective temperature used here represents the local energy density since the local thermal equilibrium condition breaks down in nanostructures. Furthermore, the average temperature at each vertical plane along the horizontal direction is obtained as,

$$\bar{T}(x) = \frac{1}{L} \int_0^L T(x, y) \mathrm{d}y \tag{4.39}$$

The averaged heat flux in the horizontal direction is calculated as,

$$q_x(x,y) = \int_0^{2\pi} \int_0^{\pi} I(x,y,\boldsymbol{s}) sin^2\theta cos\phi d\theta d\phi \tag{4.40}$$

The effective phonon thermal conductivity is calculated by Fourier's Law as,

$$k_p = \frac{\int_0^L q_x(x,y)\mathrm{d}y}{\bar{T}(0) - \bar{T}(L)} \tag{4.41}$$

Following the procedure, we obtain k_p as a function of pore size, porosity, doping density and temperature.

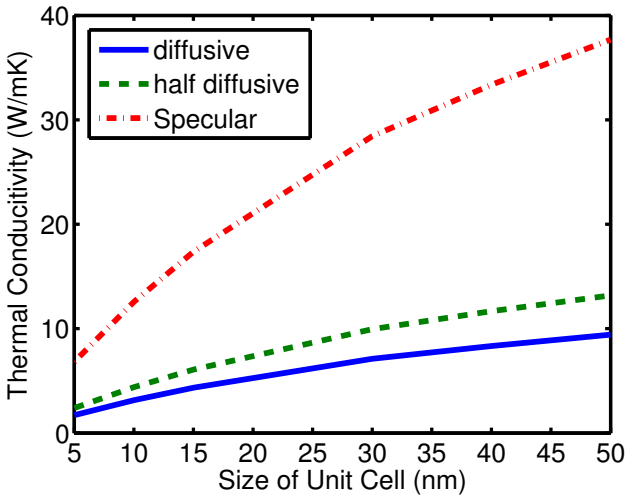

Figure 4.9: Surface roughness effect on thermal conductivity.

4.2.5 Electronic Thermal Conductivity

For semiconductor materials, the thermal conductivity contributed from electrons is ignored since it is quite small compared with that contributed from phonons. However, as the size of the material decreases, its influence cannot be neglected. With the electrical conductivity results for nanoporous Si obtained in Section 4.2.2, the electronic thermal conductivity k_e can be calculated using the

Wiedemann-Franz law,

$$k_e = \sigma L_z T \tag{4.42}$$

For metals, $L_z = 2.45 \times 10^{-8} W\Omega K^{-2}$. For semiconductors, L_z depends on doping density. The doping density dependent L_z used in our calculations are obtained from Ref. [58]. The total thermal conductivity is the sum of phononic thermal conductivity and electronic thermal conductivity.

4.3 Results and Discussions

In this section, by using the model introduced in the previous section, the simulation results for thermoelectric properties of nanoporous silicon are presented. The thermoelectric figure of merit of nanoporous silicon and its bulk nonporous counterpart are compared. Moreover, the effects of doping density, porosity, temperature and the unit cell/pore size are investigated.

4.3.1 Model Validation

As a validation of the electron transport model used in this chapter, we compare our simulation results on the electrical conductivity and Seebeck coefficient of bulk silicon with the results shown in [148] and ab-initio simulation results shown in [149]. In the simulation, the unit cell size is set to be $20nm \times 20nm$, the source (L_s) and drain (L_d) regions are both $3nm$, the length of extra silicon (L_{Si}) region is $5nm$. The mesh sizes in x direction (Δx) and in y direction (Δy) are both $0.5nm$. The doping density for source and drain is set to be $10^{20} cm^{-3}$. For comparison, the doping density of extra silicon and unit cell regions varies from $5 \times 10^{17} cm^{-3}$ to $10^{19} cm^{-3}$. In the calculation of the coupling strength of the Büttiker probes, the mobility of silicon

with different doping densities is obtained from [148–150]. Figs. (4.10) and (4.11) show the calculated resistivity and Seebeck coefficient of bulk silicon with different doping densities in comparison with the experimental data and ab-initio calculation results shown in Refs. [148] and [149], respectively. It is shown that the results match quite well with each other.

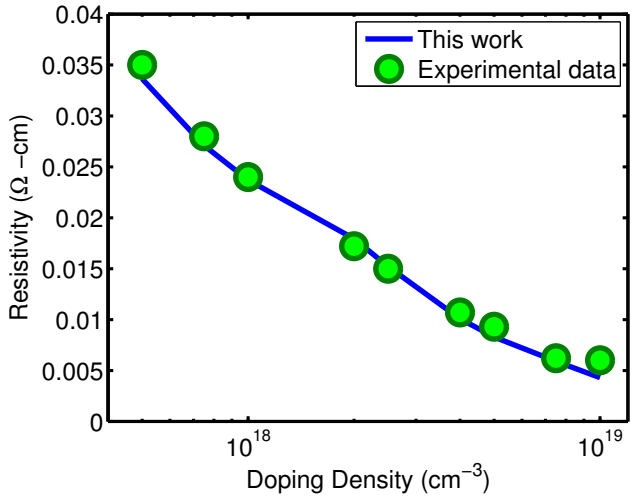

Figure 4.10: Resistivity variation of Si as a function of doping.

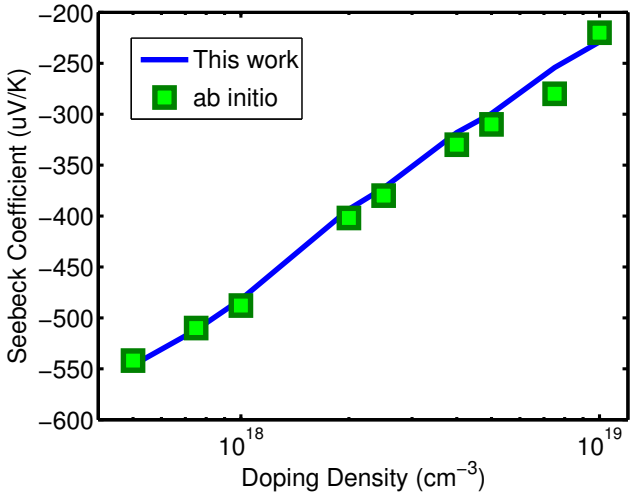

Figure 4.11: Seebeck coefficient variation of Si as a function of doping.

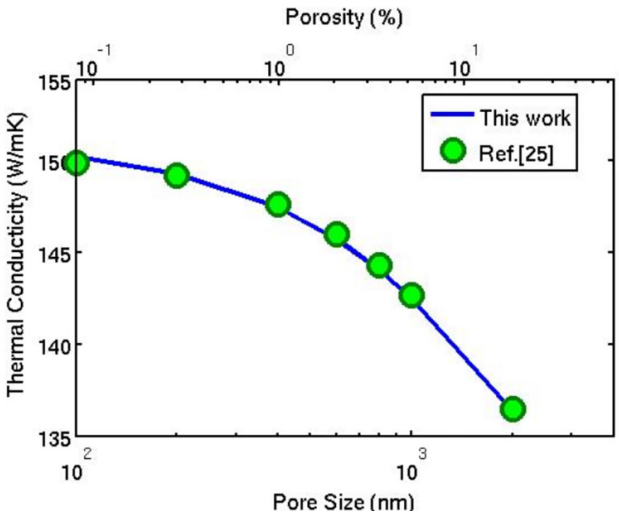

Figure 4.12: Pore size effects on thermal conductivity of multi-pore Si nanostructure.

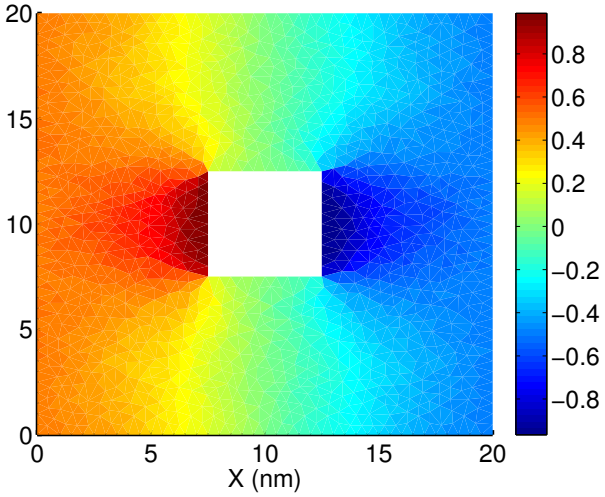

Figure 4.13: Local energy density profile within the unit cell.

The thermal conductivity of intrinsic nanoporous silicon has been calculated previously by using the BTE [124]. By excluding the phonon-dopant-impurity and phonon-electron scatterings in our model, we calculate the thermal conductivity of undoped nanoporous silicon with pore size ranging from $100nm$ to $2000nm$ (porosity from 0.08% to 32%), and compare the results with those presented in Ref. [124]. Fig. (4.12) shows that the results shown in Ref. [124] are reproduced by our calculations. As an example, Fig. (4.13) shows the profile of local energy density

within a unit cell. It is clear that local phonon energy is impeded and trapped near the left and right pore boundaries, resulting in a hot and a cold spot. Thus, phonon thermal conductivity is reduced compared to the bulk thermal conductivity.

4.3.2 Effect of Doping and Porosity

Fig. (4.14) shows the electrical conductivity, Seebeck coefficient, phonon thermal conductivity and figure of merit of nanoporous silicon with different doping densities and porosities at room temperature ($T = 300K$). The results are obtained with a unit cell size of $20nm \times 20nm$ and different porosities are obtained by changing the pore size in the unit cell. As indicated in Fig. (4.14)(a), while the electrical conductivity increases with higher doping density, it decreases with the increase of the porosity. With a doping density of $10^{20}cm^{-3}$, when the porosity increases to 36%, the electrical conductivity is reduced by more than 62% compared to its nonporous counterpart. This reduction in the electrical conductivity is mainly caused by the reduction of media for electron transport and the infinite barrier of the pores. The absolute value of Seebeck coefficient, as shown in Fig. (4.14)(b), decreases with the increase of doing density. As discussed in Refs. [151,152], the Seebeck coefficient mainly depends on the distance from the conduction band edge to the Fermi level in the material. Increase of the doping density narrows this distance, leading to the reduction in the Seebeck coefficient. When pores are introduced in the media, it becomes more difficult for the electrons with low energies to transport within the channel. However, this filtering effect of the nanopore, while increases the absolute value of Seebeck coefficient of porous silicon, is not as significant as the effect of doping. Fig. (4.14)(c) shows the effect of porosity and doping on the thermal conductivity. It is shown that the porosity has a significant effect on the thermal conductivity. When the porosity reaches 36%,

the thermal conductivity is reduced by 94% compared to the bulk value. Note that, while the thermal conductivity of bulk Si shows an appreciable decrease with the increase of doping density, the decrease is much smaller for nanoporous Si. This implies that, for nanoporous Si, phonon scattering at the pore boundary dominates other scattering mechanisms. The figure of merit (ZT) of nanoporous silicon is shown in Fig. (4.14)(d). The ZT is largely enhanced by the inclusion of nanopores. It is clear that the nanopores result in a much larger reduction in the phonon thermal conductivity than the reduction in the electrical conductivity. With doping density near $10^{20}cm^{-3}$ and porosity of 36%, the ZT is improved by 5 times compared with its bulk counterpart. However, as shown in the figure, the ZT starts to decrease with further increase of the doping density. This is due to the increase in the electronic thermal conductivity, k_e, which becomes higher with increasing doping density. When k_e reaches to a level comparable to k_p, the overall thermal conductivity of the material increases rapidly with the doping density, leading to a decrease in ZT.

4.3.3 Temperature Effect

The effect of temperature on the thermoelectric properties of nanoporous silicon is shown in Fig. (4.15). The calculations are performed in the temperature range of 200K to 600K with a porosity $P = 16\%$. For comparison, thermoelectric properties with two different doping densities are computed. It is shown that, when the temperature increases, the electrical conductivity of the material decreases due to stronger electron scattering at higher temperature. For Seebeck coefficient, as temperature increases, more electrons with higher energy contributes to the current flow, leading to an increase in the absolute value of S. For phonon thermal conductivity, at doping level of $10^{20}cm^{-3}$, as temperature increases, the thermal

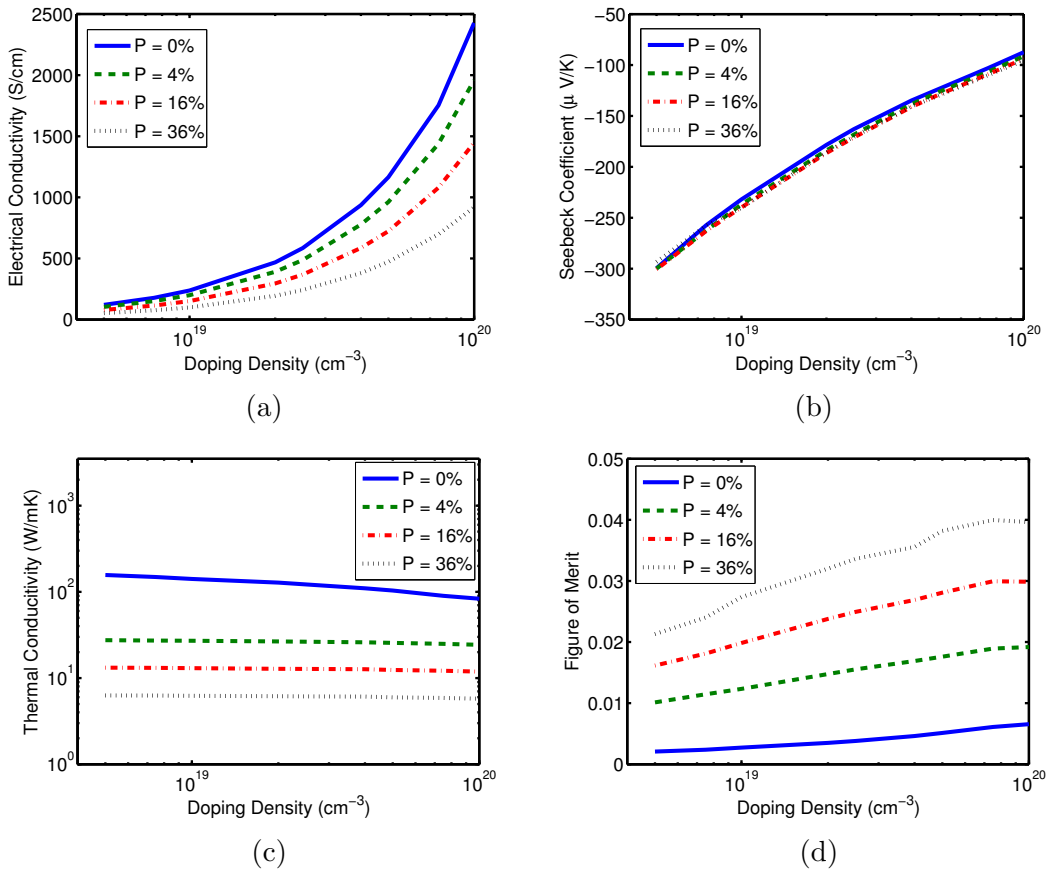

Figure 4.14: The effect of doping and porosity on the thermoelectric properties of nanoporous Si. : (a) electrical conductivity; (b) Seebeck coefficient; (c) phonon thermal conductivity; (d) figure of merit.

conductivity decreases slightly from 12.7 W/mK to 11.4 W/mK. In this temperature range, while the phonon-pore boundary scattering still dominates the overall phonon scattering, the thermal conductivity reduction is mainly due to the stronger phonon-phonon scattering at higher temperature. Finally, the figure of merit, ZT, increases as the temperature becomes higher. As shown in Fig. (4.15), with a doping density of $10^{20}cm^{-3}$, the ZT is increased by 7 times when the temperature changes from $200K$ to $600K$. The variation trend is the same for different doping densities, only the ZT increases more quickly when the doping density is higher.

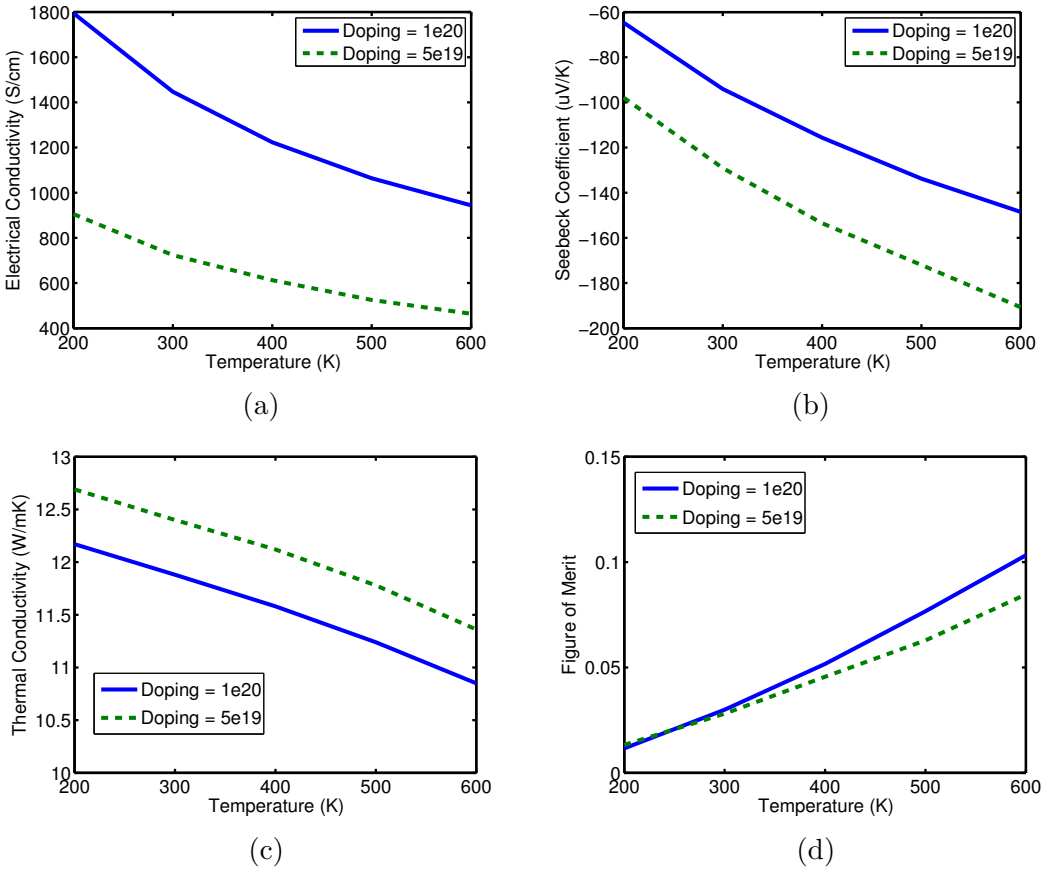

Figure 4.15: The effect of temperature on the thermoelectric property of nanoporous Si.

4.3.4 Size Effect

In this section, the effect of pore size on the thermoelectric properties is investigated. For a given porosity of the material, the size of the pore is proportional to the size of the unit cell. Based on the calculated results in the previous two sections, for an optimal figure of merit, we select doping density of $10^{20}cm^{-3}$ and temperature of $600K$ in the analysis of pore effect on the thermoelectric properties of nanoporous Si. The simulation results are shown in Fig. (4.16). It is shown that, for a given porosity, the electrical conductivity increases with the increase of nanopore size. However, for a given unit cell size, the electrical conductivity

decreases quickly with the increase of nanopore size (i.e. the increase of porosity). Fig. (4.16) shows that, for a given porosity, the absolute value of Seebeck coefficient decreases as the size of unit cell increases. The observed trend can be explained by using the carrier concentration [151]

$$n_{3D} = \frac{M}{L_{eff}} \int_{E_c} D_{2D}(E) F(E - E_f) dE \tag{4.43}$$

where n_{3D} is the doping density in the materials, M is the number of subbands introduced in y direction, L_{eff} is the effective length in y direction, E_c is the conduction band edge and E_f is the Fermi level. From Eq. (4.43), since the $2D$ density of states only depends on the effective mass of the sub-bands, the main factor leading to the change of the Fermi Dirac distribution lies in the ratio between M and L_{eff}. When the unit cell size decreases, with the same porosity, the distance in y direction between two neighboring pores narrows. For instance, when $P = 4\%$, this distance is $4nm$ for a unit cell size of $5nm \times 5nm$ while it is $24nm$ for a unit cell size of $30nm \times 30nm$. As discussed in Ref. [151], the number of sub-bands M in y direction could be reduced to only one when L_{eff} becomes smaller than $10nm$. After M reaches one, further decrease of the distance between two neighboring pores will increase M/L_{eff}. In order to keep n_{3D} the same, the Fermi Dirac function must decrease, suggesting a larger gap between the band edge and Fermi level. As a result, the absolute value of Seebeck coefficient becomes higher while the electrical conductivity decreases. This characteristic may shed a light on the design and optimization of nanoporous semiconductor materials. With the same porosity, the thermal conductivity increases with increasing unit cell size. This result shows that phonon transport is less influenced by the volume fraction of pores, but more by the spacing between the pores which determines the phonon mean free path of the

material. For a given porosity, the distance between the pores increases with the unit cell size, resulting in a larger phonon mean path, and consequently a larger thermal conductivity. Finally, combining the above results, a large increase in the ZT of nanoporous Si compared with its bulk counterpart is obtained when the nanoporous silicon has a large porosity and small pore size. In the current study, the highest figure of merit reaches 0.28 with $P = 36\%$.

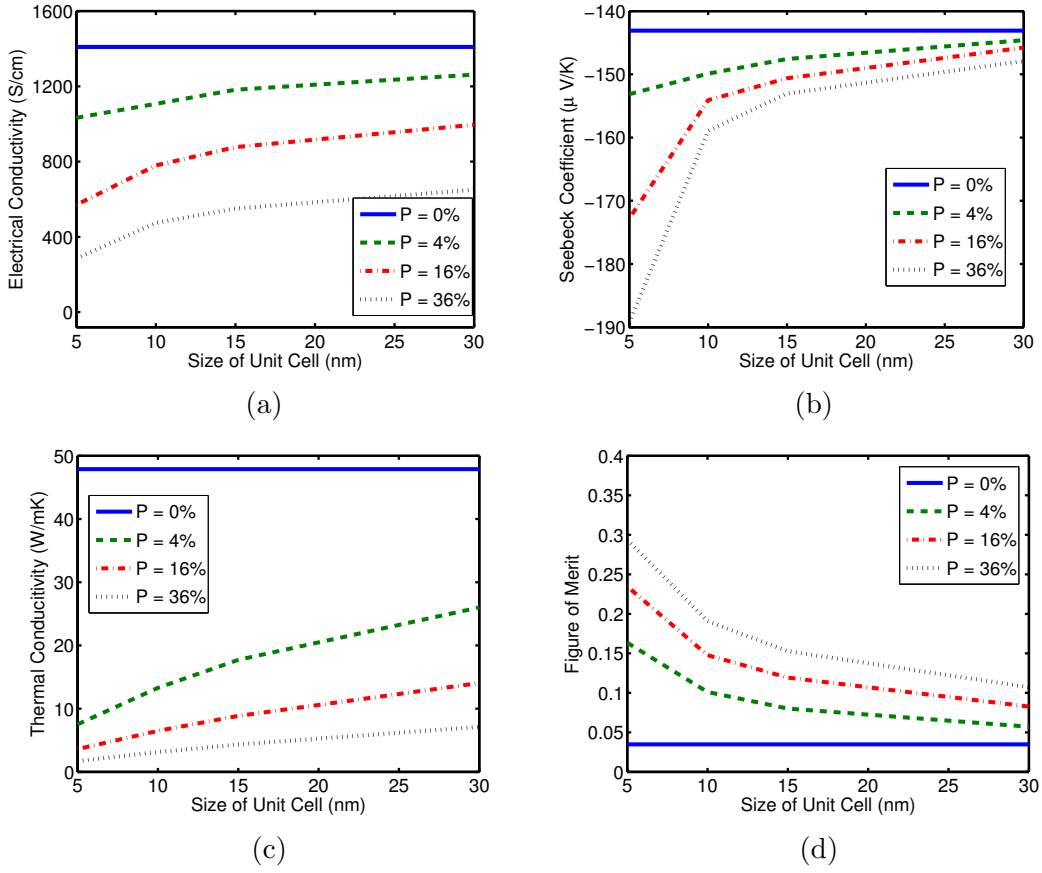

Figure 4.16: The effect of unit cell size on the thermoelectric property of nanoporous Si.

4.4 Summary

In this chapter, thermoelectric properties of nanoporous Si are numerically analyzed. A quantum NEGF-Poisson model is used to numerically calculate the electrical conductivity and Seebeck coefficient of nanoporous Si. Meanwhile, phonon BTE is solved by using the finite volume method to obtain the phonon thermal conductivity of the material. In addition, the thermal conductivity contributed from electrons is considered by using the Wiedemann-Franz law. From the computational analysis, the effects of doping density, porosity, temperature and pore size on the thermoelectric performance of nanoporous Si are systematically investigated. The results show that larger porosity, smaller pore size and higher temperature are all beneficial for improving ZT. In addition, there exists an optimal doping density for ZT. The degradation of electrical conductivity of nanoporous Si due to the inclusion of nanopores is compensated by the large reduction in the phonon thermal conductivity and increase of absolute value of the Seebeck coefficient, resulting in a significantly improved ZT. Results show a ZT of 0.28 can be obtained with doping density of $10^{20} cm^{-3}$, $T = 600K$, $P = 36\%$ and pore size of $3nm \times 3nm$.

CHAPTER 5

ANALYSIS OF BALLISTIC TRANSPORT IN NANOSCALE DEVICES BY USING AN ACCELERATED FINITE ELEMENT CONTACT BLOCK REDUCTION APPROACH

5.1 Introduction

As discussed in Chapter 2, as the size of electronic devices goes down to nanoscale regime, quantum effects such as quantum confinement and tunneling become important. Therefore, quantum-based simulation models are required to obtain a reliable understanding of electronic properties of nanoscale devices such as

quantum dots [153], nano-MOSFETs [113], electron waveguide structures [154], etc. Various computational models [42, 44, 47] have been proposed for computational analysis of such nano-devices. These models can be broadly categorized into two types. The first solves the Schrödinger equation directly on the device domain with open boundary conditions to obtain the density matrix. A well-developed model of this type is the Quantum Transmitting Boundary Method (QTBM) [42, 44], which has been successfully applied to simulate ballistic transport in various devices [155, 156]. However, the difficulty to include scattering mechanisms has barricaded its wide application [44]. The other type is based on Non-equilibrium Green's Function (NEGF) [47], within which a self-energy function is introduced to describe the coupling between the active device region and external carrier reservoirs. It has been shown that various scattering mechanisms can be incorporated in NEGF [114, 157]. However, its application in device simulation is limited by its high computational cost. In the implementation of NEGF model, repeated inversions of a matrix with dimension equal to the system degrees of freedom (DOFs) are required to obtain the retarded Green's function. For systems with very large DOFs, the computation becomes intractable on desktop computers and it is necessary to resort to parallel computing [50] which generally requires significant implementation effort and enormous computational resources. To alleviate this problem, instead of inverting the involved matrix directly, the recursive Green's function method [51] and mode-space Green's function method [52] have been developed. They have been used to analyze many nanoscale systems, such as DG-MOSFETs [51, 52, 158], resonant-tunneling diodes [159], nanowires [6, 160], carbon nanotubes [18, 161], thermoelectric nanomaterials [126, 128], etc. However, while the former is limited to devices with no more than two leads, the latter is only applicable when the device domain and

spatial potential profile are of high symmetry so that the Schrödinger equation is separable in orthogonal directions. To eliminate these limitations, a Contact Block Reduction (CBR) method was developed [54, 162] within the NEGF framework. The method can be used to simulate multi-terminal devices with arbitrary spatial potential profile. By utilizing the Dyson equation, the method obtains the retarded Green's function by carrying out a one-time solution of an eigenvalue problem on the closed device domain and repeated inversions of a small matrix of size equal to the DOFs on the contact interfaces connecting the device domain to external carrier reservoirs. By applying the Neumann boundary conditions on the contact interfaces, only a small percentage of the eigen-pairs is needed to obtain accurate results [54]. The reduction of the number of eigen-pairs reduces the computational cost. Furthermore, by projecting the involved matrices into lead mode space [162], more computational cost can be saved. To include the space charge effect, the Poisson equation is solved self-consistently with the retarded Green's function. Iterations between those two models are carried out until the solution satisfies the self-consistency criterion. Upon convergence, the current flow and electron density can be obtained straightforwardly.

While the CBR/Poisson model has been adopted to investigate electrical transport properties of devices such as nano-FinFET [163] and double-gate MOSFETs [53, 164], the numerical formulation of the model has been restricted to the Finite Difference method (FDM). This limitation impedes its applicability to devices with irregular geometry and/or unstructured mesh. In this chapter, we present a Finite Element formulation for the CBR/Poisson model. The formulation is referred to as the Finite Element Contact Block Reduction (FECBR) approach. The FECBR approach enables NEGF based analysis for devices with arbitrary geometry. Furthermore, in addition to the eigen-pair reduction and lead mode space

projection, we introduce a third level of model order reduction in the FECBR by using a component mode synthesis (CMS) technique developed in Chapter 2 to further enhance the computational efficiency. The FECBR with CMS is referred to as the accelerated FECBR. In this chapter, the accelerated FECBR is used to perform ballistic transport analysis of a DG-MOSFET with taper-shaped extensions and a DG-MOSFET with rough Si/SiO_2 interfaces. For both devices, the electrical transport properties obtained from the accelerated FECBR approach and the associated computational cost are compared with those obtained from the original CBR and direct inversion methods. The performance of the accelerated FECBR in both its accuracy and efficiency is demonstrated.

The rest of the chapter is organized as follows. Section 5.2 presents the theory, computational formulation and implementation of the FECBR approach and its model reduction techniques. In Section 5.3, numerical results and performance comparison for a DG-MOSFET with taper-shaped leads and a DG-MOSFET with Si/SiO_2 interface roughness are presented. Conclusions follow in Section 5.4.

5.2 Method

5.2.1 A review of the CBR method

The CBR method [54, 162] was developed for efficient simulations for ballistic transport analysis in electronic devices. Instead of directly inverting the matrices involved in the NEGF model, the Dyson equation is used to obtain the retarded Green's function which is the key parameter in calculating the electronic transport properties of open quantum systems, such as the transmission function, local density of states, current and electron densities. In the CBR method, the simulation domain

is first discretized into a grid of nodes (or points). The grid nodes are further divided into two groups, namely the contact grid nodes and the device grid nodes. The former contains all the grid nodes on the portion of boundary connecting the device to the external reservoirs (i.e. the leads). The latter includes all the remaining grid nodes. The advantage of the CBR is that it only requires numerical inversion of small matrices with size equal to the number of contact grid nodes in order to obtain the retarded Green's function. The retarded Green's function can be written as [54],

$$\mathbf{G}^R = [(E + j\gamma)\mathbf{I} - \mathbf{H}^0 - \mathbf{\Sigma}]^{-1} \tag{5.1}$$

where E is the energy level, j is the imaginary unit, γ is a very small positive number used to avoid numerical singularity in the calculation, $\mathbf{H}^0$ is the Hamiltonian of the closed (decoupled) system without perturbations from exterior sources, $\mathbf{\Sigma}$ is the self-energy matrix representing the interactions between the closed device system and external reservoirs and $\mathbf{I}$ is an identity matrix. Assuming the total number of grid nodes in the system is N_t, the typical computational complexity of inverting the right-hand-side of Eq. (5.1) is $O(N_t^3)$. As the inversion needs to be computed for each energy level, it becomes extremely inefficient when N_t becomes large. For this reason, in CBR, the retarded Green's function is calculated by using the Dyson equation [54, 162],

$$\mathbf{G}^R = [\mathbf{I} - \mathbf{G}^0\mathbf{\Sigma}]^{-1}\mathbf{G}^0 \tag{5.2}$$

where $\mathbf{G}^0$ can be expressed by the eigen-pairs of the closed system as

$$\mathbf{G}^0 = [(E + j\gamma)\mathbf{I} - \mathbf{H}^0]^{-1} = \sum_{n=1}^{n_t} \frac{|\psi_n\rangle\langle\psi_n|}{E - E_n + j\gamma} \tag{5.3}$$

The latter expression in the above equation is the spectral representation of $\mathbf{G}^0$, where ψ_n is the n_{th} wavefunction, E_n is the n_{th} energy level and n_t is the total number of eigen-pairs (E_n, ψ_n) in the closed system. ψ_n and E_n are the solutions of the following eigenvalue problem,

$$\mathbf{H}^0\psi = E\mathbf{M}\psi \tag{5.4}$$

In Eq. (5.2), $\mathbf{\Sigma}$ has non-zero values only for the contact grid nodes [54]. It can be decomposed into four blocks as

$$\mathbf{\Sigma} = \begin{pmatrix} \mathbf{\Sigma}_c & \mathbf{0} \\ \mathbf{0} & \mathbf{0}_d \end{pmatrix} \tag{5.5}$$

where the subscripts c, d denote the contact and device grid points in the simulation domain, respectively. Note that $\mathbf{\Sigma}_c$ has a dimension of $N_c \times N_c$, where N_c is the total number of contact grid nodes. Similarly, $\mathbf{G}^0$ can be written with four blocks as,

$$\mathbf{G}^0 = \begin{pmatrix} \mathbf{G}^0_c & \mathbf{G}^0_{cd} \\ \mathbf{G}^0_{dc} & \mathbf{G}^0_d \end{pmatrix} \tag{5.6}$$

Denoting $(\mathbf{I} - \mathbf{G}^0\mathbf{\Sigma})$ in Eq. (5.2) as $\mathbf{A}$, one can write the matrix in a four-block form as,

$$\mathbf{A} = \begin{pmatrix} \mathbf{A}_c & \mathbf{A}_{cd} \\ \mathbf{A}_{dc} & \mathbf{A}_d \end{pmatrix} = \begin{pmatrix} \mathbf{I} - \mathbf{G}^0_c\mathbf{\Sigma}_c & \mathbf{0} \\ -\mathbf{G}^0_{dc}\mathbf{\Sigma}_c & \mathbf{I} \end{pmatrix} \tag{5.7}$$

The inverse of matrix $\mathbf{A}$ can be obtained as

$$\mathbf{A}^{-1} = \begin{pmatrix} (\mathbf{I} - \mathbf{G}^0_c\mathbf{\Sigma}_c)^{-1} & \mathbf{0} \\ \mathbf{G}^0_{dc}\mathbf{\Sigma}_c(\mathbf{I} - \mathbf{G}^0_c\mathbf{\Sigma}_c)^{-1} & \mathbf{I} \end{pmatrix} \tag{5.8}$$

Substituting both Eq. (5.8) and Eq. (5.6) into Eq. (5.2), the retarded Green's function $\mathbf{G}^R$ can be obtained as,

$$\mathbf{G}^R = \mathbf{A}^{-1}\mathbf{G}^0 = \begin{bmatrix} \mathbf{A}_c^{-1}\mathbf{G}_c^0 & \mathbf{A}_c^{-1}\mathbf{G}_{cd}^0 \\ \mathbf{G}_{dc}^0\mathbf{\Sigma}_c\mathbf{A}_c^{-1}\mathbf{G}_c^0 + \mathbf{G}_{dc}^0 & \mathbf{G}_{dc}^0\mathbf{\Sigma}_c\mathbf{A}_c^{-1}\mathbf{G}_{cd}^0 + \mathbf{G}_d^0 \end{bmatrix} \tag{5.9}$$

where $\mathbf{A}_c^{-1} = (\mathbf{I} - \mathbf{G}_c^0\mathbf{\Sigma}_c)^{-1}$. Computing the four blocks in Eq. (5.9) only requires an inversion of $\mathbf{A}_c$. Since the size of $\mathbf{A}_c$ is equal to the number of contact grid nodes, N_c, and $N_c \ll N_t$, the computational cost of the inversion reduces from $O(N_t^3)$ to $O(N_c^3)$. After $\mathbf{G}^R$ is obtained, the local density of states, transmission function, electron and current densities can be calculated by following the standard self-consistent CBR/Poisson procedures described in Refs. [54, 162].

5.2.2 Finite Element Contact Block Reduction (FECBR) approach

To our best knowledge, the CBR/Poisson model has only been formulated for numerical analysis using the Finite Difference schemes. A major drawback of the FDM is that it is only suitable for computational domains with simple geometry and structured grid. To extend the application of CBR into device simulations involving irregular geometries and/or unstructured mesh, we develop a Finite Element formulation for the CBR/Poisson model. By following Section 2.2.2, the weak form of the 2D Schrödinger equation can be obtained as in Eq. (2.7). In the following, we illustrate the procedures on how to derive $\mathbf{G}^0$ and $\mathbf{\Sigma}_c$ with Eq. (2.7). First, to obtain $\mathbf{G}^0$, the Hamiltonian $\mathbf{H}^0$ for the closed system needs to be calculated. This could be achieved by applying the Neumann boundary condition $(\nabla\psi \cdot \overrightarrow{n_i}) = 0$ on the contact grids and the Dirichlet boundary condition $\psi = 0$ on the rest of the

boundary nodes to Eq. (2.7). Note that the Neumann boundary condition [54, 162] is the key to guarantee the accuracy of simulations with an incomplete set of eigen-pairs. In FEM, such boundary conditions can be automatically applied by dropping the first term in Eq. (2.7). Therefore, Eq. (2.7) for closed system can be obtained as that in Eq. (2.8). By following the same procedures to approximate the wavefunctions in the domain as those in Section 2.2.2, Eq. (2.11) is obtained and it is used to solve for the eigen-pairs in the closed system. By using those eigen-pairs, $\mathbf{G}^0$ in Eq. (5.3) can be obtained, which can be used to obtain $\mathbf{G}^R$ in Eq. (5.9).

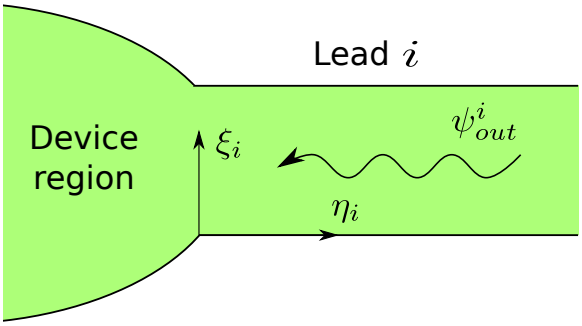

Figure 5.1: Semi-infinite leads connected with device region.

Next, we calculate the self-energy matrix $\mathbf{\Sigma}^i$ by applying open boundary conditions to Eq. (2.7). As shown in Fig. 5.1, at the contact interface between the device region and the i-th lead, the wavefunctions in the lead and device must satisfy,

$$\psi^i_{lead}|_{\eta_i=0} = \psi|_{\eta_i=0} \tag{5.10}$$

$$\nabla\psi^i_{lead}|_{\eta_i=0} = \nabla\psi|_{\eta_i=0} \tag{5.11}$$

where ψ^i_{lead} is the wavefunction in the i-th lead and $\psi|_{\eta_i=0}$ is the wavefunction in the device evaluated at the contact interface. The leads are assumed to be semi-infinite and homogeneous. Consequently, the wavefunction ψ^i_{lead} can be expressed as a linear combination of the products of 1D plane waves in the η_i-direction and localized lead

modes in the ξ_i-direction [165], i.e.,

$$\psi^i_{lead}(\eta_i, \xi_i) = \sum_{m=1}^{m_s} b^i_m \chi^i_m(\xi_i) exp(jk^i_m \eta_i) \tag{5.12}$$

where m_s is the total number of lead modes and k^i_m is the m-th mode wavevector in the i-th lead which can be calculated from $k^i_m = \sqrt{2m^*_{\eta_i}/\hbar^2(E - E^i_m)}$. E^i_m and χ^i_m can be obtained by solving a 1D Schrödinger equation with closed boundary conditions,

$$-\frac{\hbar^2}{2m^*_{\xi_i}} \frac{\partial^2 \chi^i(\xi_i)}{\partial \xi_i^2} + U^i(\xi_i)\chi^i(\xi_i) = E^i \chi^i(\xi_i) \tag{5.13}$$

where U^i is the potential on the contact boundary Γ_i obtained from the solution of the 2D Poisson equation over the device domain. Multiplying both sides of Eq. (5.12) with χ^i_n, we obtain,

$$\langle \chi^i_n(\xi_i) | \psi^i_{lead}(\eta_i, \xi_i) \rangle = b^i_n exp(jk^i_n \eta_i) \tag{5.14}$$

Note that $\langle \chi^i_m(\xi_i) | \chi^i_n(\xi_i) \rangle = \delta_{m,n}$, where $\delta_{m,n}$ is the Kronecker Delta function. Therefore, by using Eq. (5.12) and the above equation, the derivative of ψ^i_{lead} in the normal direction can be obtained as,

$$(\nabla \psi^i_{lead} \cdot \overrightarrow{n_i})|_{\eta_i=0} = \sum_{m=1}^{m_s} jk^i_m \chi^i_m(\xi_i) \langle \chi^i_m(\xi_i) | \psi^i_{out}(0, \xi_i) \rangle \tag{5.15}$$

By using the continuity conditions in Eq. (5.10) and Eq. (5.11) along with the above equation, the first term in Eq. (2.7) for the i_{th} lead can be transformed to be,

$$B = \sum_m -\frac{\hbar^2 jk^i_m}{2m^*_{\eta_i}} \int_{\xi_i} \delta\psi^i(\xi_i)\chi^i_m(\xi_i) \mathrm{d}\xi_i \int_{\xi_i} \chi^i_m(\xi_i)\psi^i(\xi_i) \mathrm{d}\xi_i \tag{5.16}$$

By using the 1D finite element approximation of the wavefunction and test function along the contact interface, Eq. (5.16) can be written in discretized form as,

$$B = \begin{pmatrix} \delta\psi_1^i & \delta\psi_2^i & \cdots & \delta\psi_{n_\xi}^i \end{pmatrix} \mathbf{\Sigma}^i \begin{pmatrix} \psi_1^i \\ \psi_2^i \\ \vdots \\ \psi_{n_\xi}^i \end{pmatrix} \tag{5.17}$$

where ψ_j^i is the wavefunction at the j-th node on the contact interface connecting the i-th lead, n_ξ is the number of nodes on that contact interface, and $\mathbf{\Sigma}^i$ is the self-energy matrix obtained from the finite element discretization which can be written as,

$$\mathbf{\Sigma}^i = (\mathbf{SQ})\mathbf{\Lambda}(\mathbf{SQ})^T \tag{5.18}$$

where $\mathbf{S}$ is assembled from the following element matrices of 1D element along ξ_i,

$$\mathbf{S}^e = \int_{\xi_i^e} (\mathbf{N}^{1D})^T \mathbf{N}^{1D} \mathrm{d}\xi_i^e \tag{5.19}$$

and,

$$\begin{bmatrix} \chi_1^i(\xi_1) & \chi_2^i(\xi_1) & \cdots & \chi_m^i(\xi_1) & \cdots & \chi_{m_s}^i(\xi_1) \\ \chi_1^i(\xi_2) & \chi_2^i(\xi_2) & \cdots & \chi_m^i(\xi_2) & \cdots & \chi_{m_s}^i(\xi_2) \\ \cdots & \cdots & \cdots & \cdots & \cdots & \cdots \\ \chi_1^i(\xi_{m_s}) & \chi_2^i(\xi_{m_s}) & \cdots & \chi_m^i(\xi_{m_s}) & \cdots & \chi_{m_s}^i(\xi_{m_s}) \end{bmatrix} \tag{5.20}$$

$$\mathbf{\Lambda} = -\frac{\hbar^2}{2m_{\eta_i}^*} diag(jk_1^i, \quad jk_2^i, \quad \ldots, \quad jk_m^i, \quad \ldots, \quad jk_{m_s}^i) \tag{5.21}$$

The global self-energy matrix $\mathbf{\Sigma}_c$ is a diagonal assembly of all the $\mathbf{\Sigma}^i$. Once $\mathbf{G}^0$ and $\mathbf{\Sigma}_c$ are computed, the retarded Green's function in Eq. (5.9) can be calculated

straightforwardly. To account for the space charge effect, the Poisson equation, i.e., Eq. (3.24) is solved by FEM self-consistently with CBR in this chapter. The Dirichlet boundary condition is applied on the boundary along gates and the Neumann boundary condition is applied on the rest of the boundary in the domain.

5.2.3 FECBR-modal approach: lead mode space projection

As discussed in Ref. [54], by projecting the involved matrices in real space into lead mode space which is formed by the lead modes, the computational cost can be further reduced by neglecting the decaying lead modes. In the lead mode space, the self-energy matrix is diagonal [54, 162],

$$(\mathbf{\Sigma}^i)_{LM} = -\frac{\hbar^2}{2m^*_{\eta_i}} diag(jk^i_1, \quad jk^i_2, \quad \ldots, \quad jk^i_m, \quad \ldots, \quad jk^i_{m_s}) \tag{5.22}$$

It's proved [166] that the purely real elements in $(\mathbf{\Sigma}^i)_{LM}$ have negligible effect on the calculation of device electrical transport parameters. Those real elements are corresponding to decaying modes from the leads with $E^i_m > E$. The lead modes having $E^i_m < E$ are the propagating modes. The n-th wavefunction in the 2D closed system along the contact interface $\psi_{n,c}$ can be transformed into the lead mode space as,

$$\boldsymbol{\omega}_n = \begin{pmatrix} \omega^{i=1}_{n,m=1} & \ldots & \omega^{i=1}_{n,m=\mu_1} & \ldots & \omega^{i=\lambda}_{n,m=1} & \ldots & \omega^{i=\lambda}_{n,m=\mu_\lambda} \end{pmatrix}^T \tag{5.23}$$

where μ_i is number of propagating modes kept in the i_{th} lead and,

$$\omega^i_{n,m} = \langle \psi^i_{n,c} | \chi^i_m \rangle = \int_{\xi_i} \psi^i_{n,c}(\xi_i) \chi^i_m(\xi_i) \mathrm{d}\xi_i \tag{5.24}$$

To calculate the current, the block $\mathbf{G}_c^0$ in the lead mode space can be transformed as,

$$(\mathbf{G}_c^0)_{LM} = \sum_{n=1}^{\alpha} \frac{\boldsymbol{\omega}_n \boldsymbol{\omega}_n^T}{E - E_n + j\gamma} \tag{5.25}$$

where α is the number of kept eigen-pairs in the 2D closed system. It will be shown in later sections that only a small percentage of all the eigen-pairs needs to be calculated from Eq. (2.11). In the calculation of the electron density, the left column of blocks in $\mathbf{G}^0$ needs to be transformed into a mixed-space (real/lead mode space) representation as [167],

$$(\mathbf{G}_{tc}^0)_{R+LM} = \sum_{n=1}^{\alpha} \frac{\psi_n \omega_n^T}{E - E_n + j\gamma} = \mathbf{\Psi}\mathbf{\Phi}^T \tag{5.26}$$

where $\mathbf{\Psi}$ and $\mathbf{\Phi}$ are

$$\mathbf{\Psi} = (\boldsymbol{\psi}_1, \quad \boldsymbol{\psi}_2, \quad \ldots, \quad \boldsymbol{\psi}_n, \quad \ldots, \quad \boldsymbol{\psi}_\alpha) \tag{5.27}$$

$$\mathbf{\Phi} = \frac{1}{E - E_n + j\gamma} (\boldsymbol{\omega}_1, \quad \boldsymbol{\omega}_2, \quad \ldots, \quad \boldsymbol{\omega}_n, \quad \ldots, \quad \boldsymbol{\omega}_\alpha) \tag{5.28}$$

By using $(\mathbf{\Sigma}^i)_{LM}$, $(\mathbf{G}_c^0)_{LM}$ and $(\mathbf{G}_{tc}^0)_{R+LM}$, the current and electron densities can be obtained [162,166]. Since only propagating modes are kept from the whole set of lead modes and typically the number of propagating modes μ_i is small compared to m_s, the size of involved matrices and associated computation cost is further reduced. Note that, if all the lead modes were kept in the calculation, the results would be identical to those obtained in real space. More details of the lead mode space projection can be found in Ref. [167].

5.2.4 Accelerated FECBR using component mode synthesis (CMS)

By using the lead mode space and keeping a small set of eigen-pairs of the 2D closed system, the computational cost can be reduced significantly in the calculation of the retarded NEGF [54, 162]. However, when the system's degrees of freedom (DOFs) continue to increase, the computational cost of solving the generalized eigenvalue problem in Eq. (5.4) becomes dominant. In Section 2.3, we have introduced component mode synthesis (CMS) approaches for efficient quantum mechanical electrostatic analysis of closed systems. In this chapter, the CMS approaches are employed to accelerate the calculation of Eq. (5.4) in the FECBR approach. To obtain the generalized eigenvalue problem, in FECBR approach, the Neumann boundary condition is applied on the contact grids while the Dirichlet boundary condition is applied on the rest of the boundary nodes. Note that the Neumann boundary condition [54, 162] is the key to guarantee the accuracy of simulations with an incomplete set of eigen-pairs in FECBR. As discussed in Section 2.3, to implement CMS approaches, there are four basic steps [168]: (1) the division of the domain Ω into a set of components, (2) the definition of component basis vectors, (3) the coupling of the components to form a reduced-order global system, and (4) the recovery of the global wave functions. Based on different ways to compose the basis vectors, there are two commonly used CMS approaches, i.e., the fixed-interface CMS and the free-interface CMS. More implementation details can be found in Section 2.3, they are not repeated here. By using the CMS approaches, the required eigen-pairs to obtain $\mathbf{G}^0$ in Eq. (5.3) can be calculated efficiently.

5.3 Results and Discussions

Two examples are shown in this section to demonstrate the performance of the accelerated FECBR approach. In the first example, analysis of ballistic transport in a DG-MOSFET with taper-shaped lead extensions is presented. The second example investigates the effect of Si/SiO_2 interface roughness on the electrical transport properties of a DG-MOSFET with rectangular lead extensions. Note that both cases involve irregular geometries which can only be handled properly using unstructured meshes. For both examples, electrical transport properties including the electron density, potential profile and current density are computed. The accuracy and efficiency of the FECBR, FECBR-modal, accelerated FECBR and the direct inversion approaches are compared. In both examples, the material in the channel and leads is Si. The material parameters used in the calculations are as follows: the permittivity of Si is taken as $11.7\varepsilon_0$, where ε_0 is the permittivity of free space. The electron effective masses are $m_l = 0.92m_0$ and $m_t = 0.19m_0$, where m_l, m_t and m_0 are the longitudinal, transverse and free electron effective mass, respectively. The effective mass and permittivity of SiO_2 are $0.4m_0$ and $3.9\varepsilon_0$, respectively. For both devices, the leads are assumed n-doped and the channel is considered as intrinsic. Therefore, the three pairs of conduction valleys are considered and hole transport is not included. The doping density in the source and drain is set to be 10^{20} cm^{-3}. Source and drain reservoirs are assumed to be in equilibrium condition. The Fermi levels for source and drain are taken as $E_{fs} = 0$ and $E_{fd} = -V_d$, respectively. The x, y and z directions of the simulation domain are assumed to be aligned with crystal directions $\langle 100 \rangle$. The electron transport in [100] direction is considered and assumed to be coherent. When solving the Poisson equation, the gate metal work function is $4.55eV$, the Neumann boundary condition

is applied on the lead boundaries to maintain charge neutrality in the extensions [52].

5.3.1 Example 1: taper-shaped DG-MOSFET

Figure 5.2 shows a DG-MOSFET with taper-shaped lead extensions. The taper-shaped DG-MOSFET was proposed in Ref. [44]. The denotations are as follows: L_c and L_d are the lengths of leads and channel, respectively; H_c and H_d is the widths of leads and channel, respectively; G_t and G_b are the top and bottom gates for the channel, respectively. Note that there is no overlap between gates and lead extensions. The two lead extensions are treated as source and drain reservoirs, respectively. In our simulations, the parameters are taken as: $L_c = L_d = 5$ nm, $H_c = 5$ nm and $H_d = 3$ nm. The SiO_2 thickness t_{ox} is set to be 1 nm. Note that no wavefunction penetration into the dioxide region is considered in this case. To investigate the computational cost as a function of system DOFs, the domain is discretized using different meshes. As an example, the calculated electron density and potential profile of the device are shown in Fig. 5.3 and Fig. 5.4, respectively. The results are obtained using a mesh with 1616 nodes, $V_{ds} = 0.5$ V and $V_{gs} = 0.5$ V. In addition, the IV curves of the device are also obtained using the direction inversion, FECBR and FECBR-modal approaches, the comparison of the results is shown in Figs. 5.5 and 5.6. It is shown that the FECBR and the direct inversion method give identical results while the results from FECBR-modal neglecting the decaying modes from the leads are quite accurate.

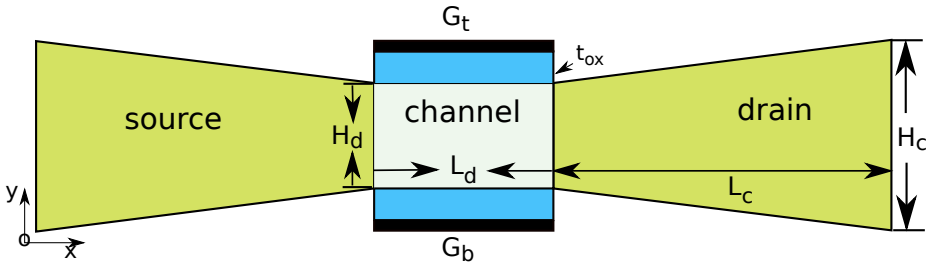

Figure 5.2: DG-MOSFET with taper-shaped lead extensions.

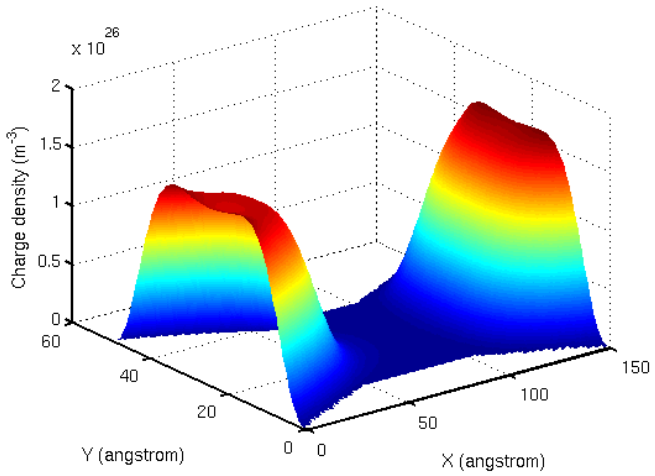

Figure 5.3: Electron density distribution in the DG-MOSFET shown in Fig. 5.2.

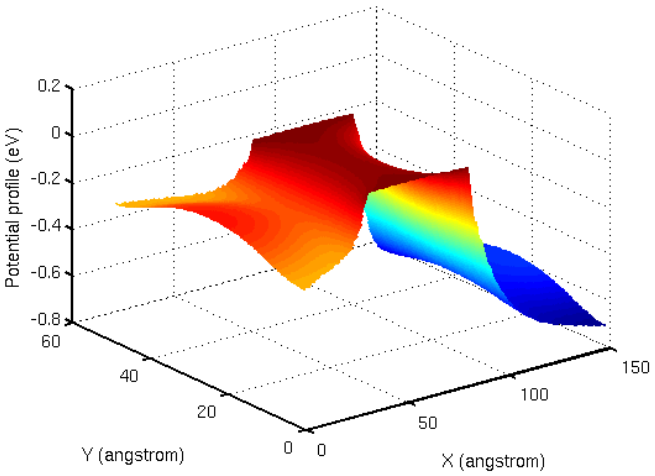

Figure 5.4: Potential profile in the DG-MOSFET shown in Fig. 5.2.

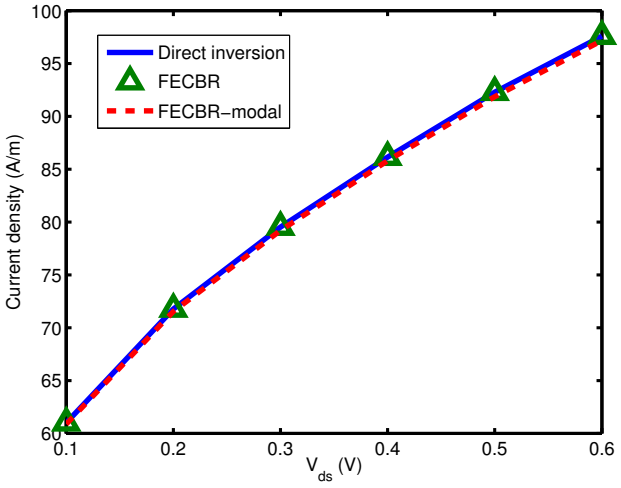

Figure 5.5: IV curve with varying drain voltage.

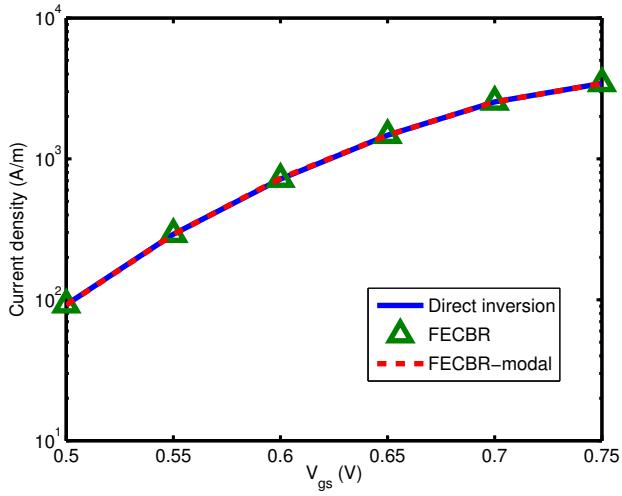

Figure 5.6: IV curve with varying gate voltage.

As indicated previously, one only needs to keep a small percentage of the closed-system eigen-pairs in the retarded Green's function calculation to achieve a reasonable accuracy of the final results, which leads to a significant reduction in computational cost. Figures 5.7 and 5.8 show the computed electron density and potential profiles along the x-direction at $y = 2$ nm, respectively. The results are obtained by using the FECBR-modal approach with $V_{ds} = 0.5$ V, $V_{gs} = 0.5$ V and a mesh with 5332 nodes.

It is shown that the results are still quite accurate when as few as 3% of the eigen-pairs corresponding to the lowest energies are computed from Eq. (2.11). Note that the FECBR-modal approach using 3% of the closed-system eigen-pairs is denoted as FECBR-modal (3%). The result shows that the current densities obtained by using 100% and 3% eigenstates are 94.8 A/m and 95.27 A/m, respectively. The error is about 0.5%. However, by reducing the number of eigen-pairs in the simulation, the computation cost is reduced significantly.

Table 5.1 shows the computational cost comparison of the methods. It is shown that the FECBR approach largely reduces the computational cost by avoiding the direct inversion of the right hand side of Eq. (5.1). The FECBR-modal further speeds up the calculation by neglecting the decaying modes in the leads. The computational cost is reduced further by computing only a small portion of the closed-system eigen-pairs corresponding to the lowest energies. For example, the computational cost of the direct inversion is about 48, 58 and 1495 times of that required by the FECBR, FECBR-modal and FECBR-modal (3%) approaches when the system DOFs is 5332. In addition, as the number of nodes (i.e. DOFs) increases, the CPU time increase rates of the FECBR methods are lower that that of the direct inversion method. Therefore, the computational cost saved by the FECBR and FECBR-modal approaches becomes more significant for larger DOFs. As shown in Table 5.1, when the DOFs increase to 10251, while the direct inversion approach becomes intractable on a desktop PC, the FECBR-modal (3%) can still solve the problems fairly efficiently.

Table 5.1: Comparison of computational cost per Green's function/Poisson iteration.

DOFs / **Methods**	1616	2556	3916	4496	5332	10251
Direct inversion	603.48s	2108.46s	7069.58s	9917.86s	19599.54s	n/a
FECBR	40.98s	78.45s	179.71s	240.13s	410.02s	2387.77s
FECBR-modal	18.28s	57.04s	143.11s	198.87s	340.47s	1728.97s
FECBR-modal (3%)	1.58s	2.8s	5.75s	7.5s	13.11s	53.8s

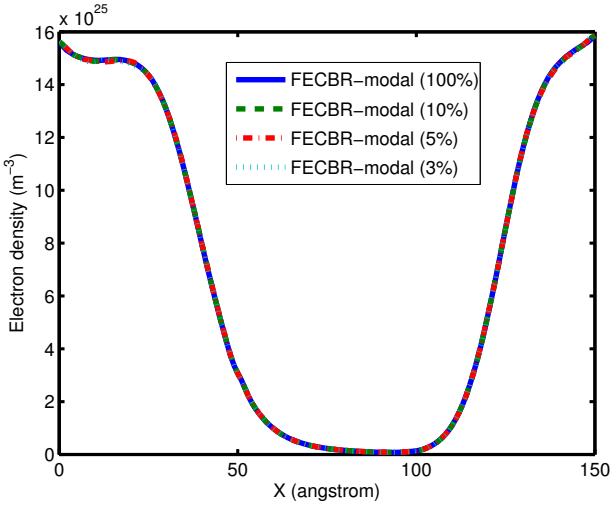

Figure 5.7: Electron density distribution along the x-direction at $y = 2$ nm.

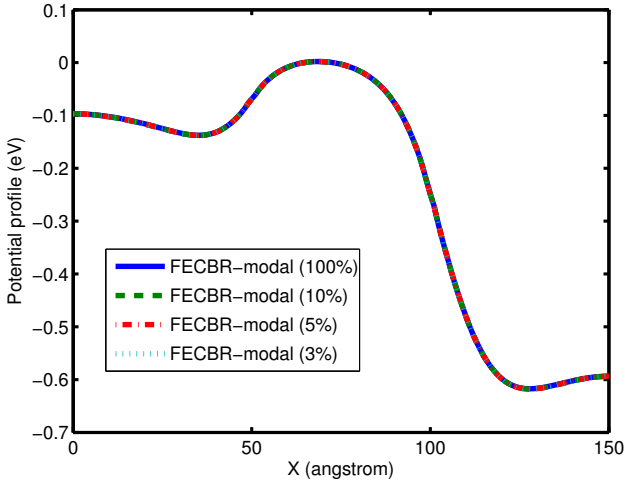

Figure 5.8: Potential profile along the x-direction at $y = 2$ nm.

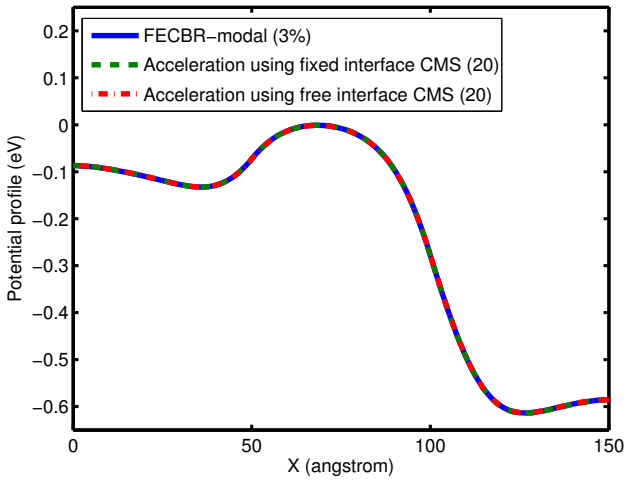

Figure 5.9: Potential profile along the x-direction at $y = 2$ nm.

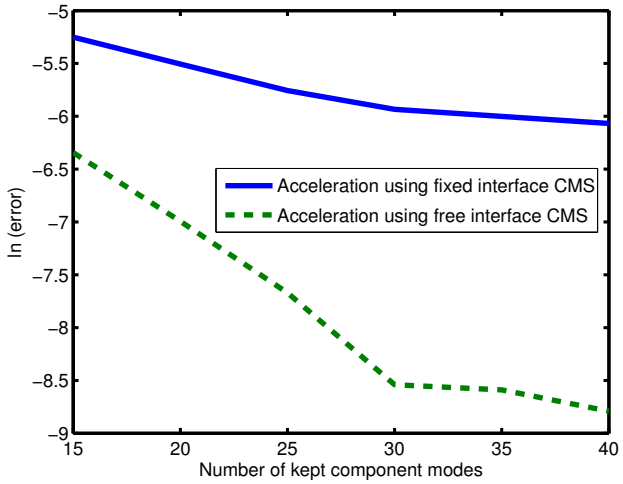

Figure 5.10: Variation of error in electron density with number of retained component modes.

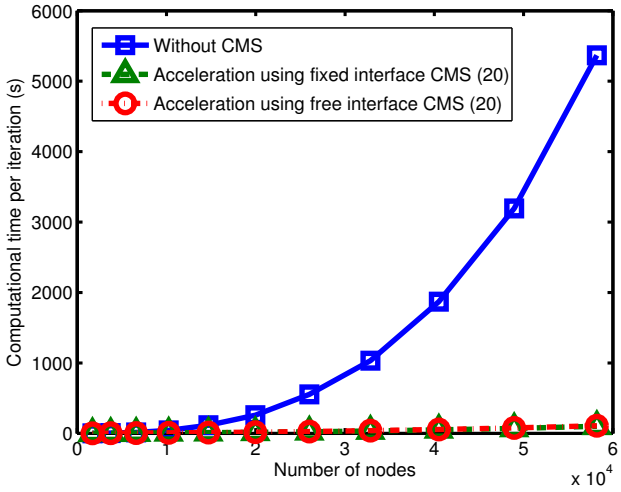

Figure 5.11: Computation cost for eigen-pairs calculation.

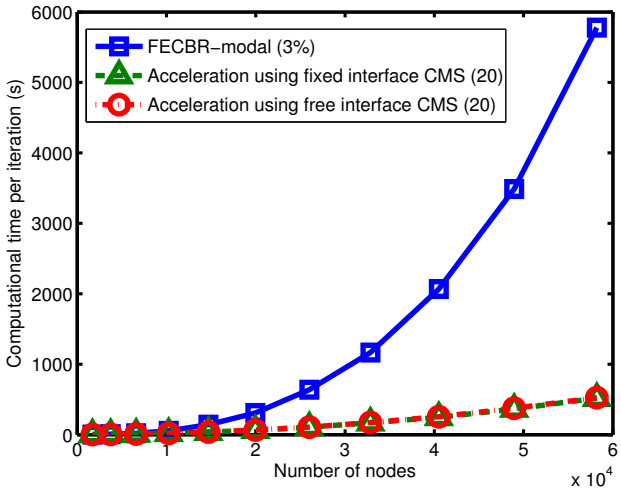

Figure 5.12: Total computation cost per Green's function/Poisson iteration.

When the system DOFs continue to increase, it is observed that the CPU time consumed by solving for the closed-system eigen-pairs (i.e. the solution of Eq. (2.11)) starts to dominate the total computational cost. For example, when DOFs = 5.8201×10^4, the total computational cost for a single Green's function/Poisson iteration is $5777.7s$ in which $5368.2s$ is used for calculating the required eigen-pairs from Eq. (2.11). In such cases, the FECBR-modal approach is accelerated by

incorporating the CMS methods for calculating the required eigen-pairs. In this example, the entire domain is decomposed into 16 components and 3% of the global eigen-pairs are retained to obtain the retarded Green's function. The accuracy of the accelerated FECBR-modal is investigated by using different number of component modes and the results are shown in Fig. 5.9 and Fig. 5.10. The error shown in Fig. 5.10 is evaluated by Eq. (2.48). Figure 5.9 shows the potential profile along the x-direction at $y = 2$ nm with 20 component modes retained in each component. Figure 5.10 shows that, as the number of retained component modes increases, the error of both CMS methods reduces. However, the accelerated FECBR with the free interface CMS has a better convergence property than that of the fixed interface CMS. The explanation can be found in Ref. [168]. Next, the computational cost of the original and accelerated FECBR-modal (3%) are compared. Figure 5.11 shows the computational cost comparison for calculating the required eigen-pairs. Figure 5.12 shows the total time consumed by each Green's function/Poisson iteration. It is evident that the CMS acceleration techniques lead to a large reduction of the computational cost. Specifically, as shown in the figures, with the number of nodes $= 5.8201 \times 10^4$, the CPU time with CMS acceleration is about 1/50 of that used by the standard eigensolver for computing the eigen-pairs. If including all the calculations in the global iteration, the CPU time ratio is less than 1/10. This result also implies that, by using the CMS acceleration, the computational cost of computing the eigen-pairs is still a small portion of the total cost. The results also show that the fixed and free interface CMS acceleration methods offer similar efficiency.

5.3.2 Example 2: DG-MOSFETs with Si/SiO_2 interface roughness

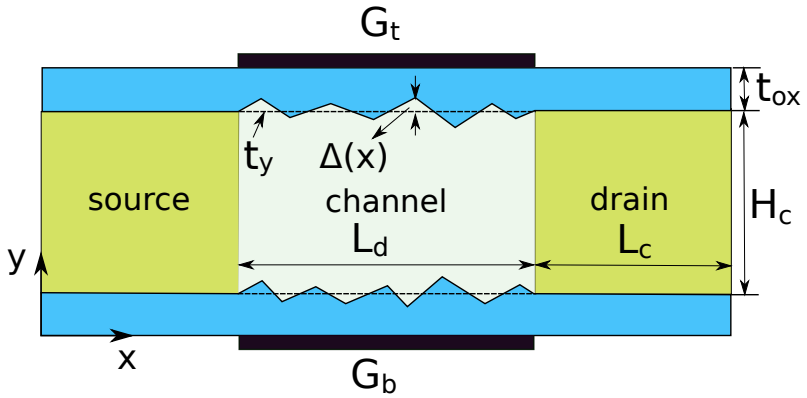

Figure 5.13: DG-MOSFET with Si/SiO_2 interface roughness.

The effect of interface roughness on the performance of planar MOSFETs has been investigated using different approaches including Monte Carlo [169] and mode-space NEGF [170] methods. It is shown that the interface roughness may degrade the electron mobility in the channel and increase gate threshold voltage [169, 170]. In this section, we show that by using the accelerated FECBR approach, the effect of geometrical Si/SiO_2 interface roughness on the electrical transport properties of DG-MOSFETs can be captured properly and efficiently.

The morphology of a rough interface is obtained by following the steps described in Ref. [171, 172]. The interface roughness is assumed to be due to the fluctuation of the SiO_2 thickness from its ideal position t_y as shown in Fig. 5.13. For a given position x, the Si/SiO_2 interface position can be denoted by

$$T_y = t_y + \Delta(r) \tag{5.29}$$

where t_y is the ideal Si dioxide position without roughness and $\Delta(r)$ is the thickness deviations from its ideal position. $\Delta(r)$ can be modeled by the following exponential

autovariance function [171, 172],

$$\langle \Delta(r)\Delta(r-r')\rangle = \Delta_m^2 e^{\sqrt{2}x/L_m} \tag{5.30}$$

where Δ_m is the rms fluctuation, L_m is the correlation length, r is the distance between two sampling points along the interface. Based on the autovariance function, the interface position function T_y can be obtained. More calculation details can be found in Refs. [171, 172]. The generated rough Si/SiO_2 interface is then incorporated into the geometry of the DG-MOSFET. In this example, the parameters shown in Fig. 5.13 are set to be: $L_c = 5$ nm, $L_d = 10$ nm, $H_c = 3$ nm and $t_{ox} = 2$ nm. To better capture the effect of interface roughness, wavefunction penetration into the SiO_2 region is included in the calculation. Three different interface roughness cases are simulated and the parameters are taken from Ref. [172]: roughness I with $\Delta_m = 0.14$ nm, roughness II with $\Delta_m = 0.2$ nm and roughness III with $\Delta_m = 0.28$ nm. L_m is taken as 0.7 nm. As an example, Fig. 5.14 shows a meshed computational domain for interface roughness I. The domain is decomposed into 14 components as shown by the colored regions.

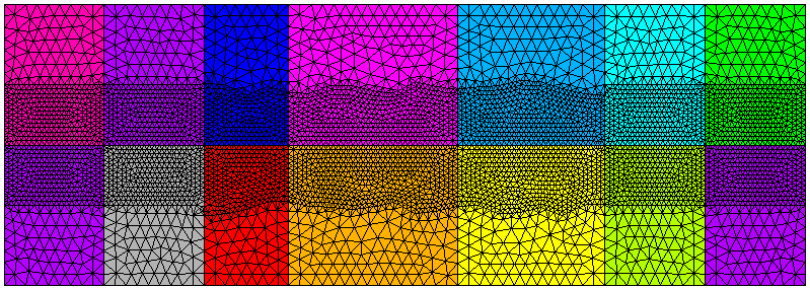

Figure 5.14: Computational domain mesh and component decomposition.

The effect of interface roughness on the current flow in the device is shown in Figs. 5.15 and 5.16. The interface roughness degrades the current density in the device and the degradation becomes more severe as Δ_m increases. This is due to the increase of

threshold voltage and decrease of electron mobility caused by the interface roughness. Similar trend has been observed in another analysis of interface roughness effect on electrical transport in Si nanowires [147].

Next, the performance of the FECBR-modal approaches is studied. Note that all the computational cost results shown in this section is obtained by using interface roughness I. The accuracy of the computed electron density and potential profile along the x-direction at y = 3.5 nm using the unaccelerated FECBR-modal approach with different percentages of kept eigen-pairs is shown in Fig. 5.17 and Fig. 5.18. The results are obtained by using 5164 nodes, $V_{ds} = 0.1$ V and $V_{gs} = 0.65$ V. Similar to Example 1, it is shown that keeping a small percentage of closed-system eigen-pairs is sufficient to achieve a good accuracy in the results. Moreover, with 3% kept eigen-pairs, the CPU time consumed by FECBR-modal is 12.13 s which is 1/1570 of that consumed by the direct inversion method (19046 s).

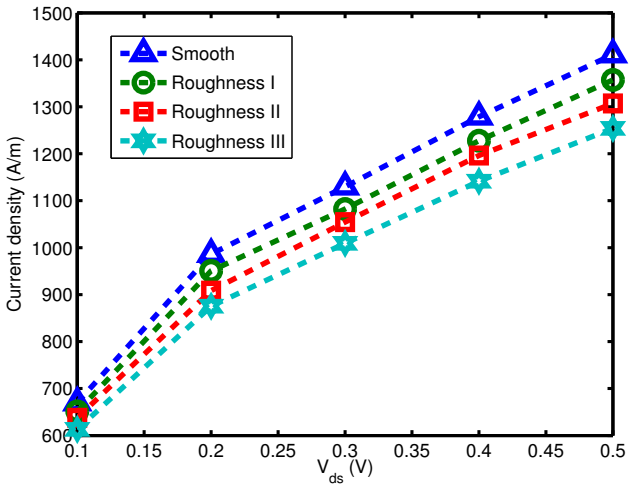

Figure 5.15: Current density as a function of V_{ds}.

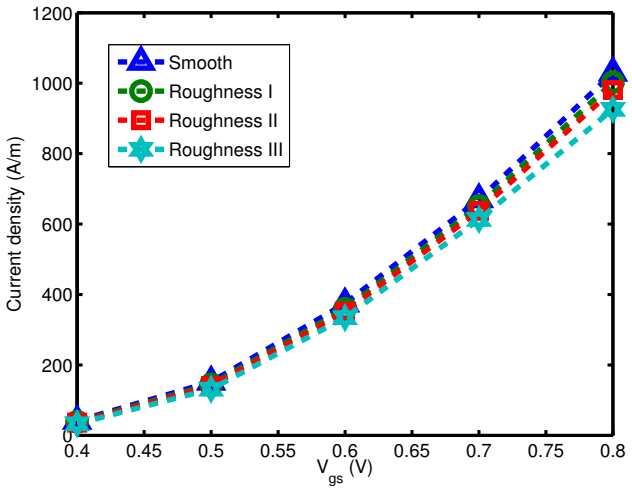

Figure 5.16: Current density as a functions of V_{gs}.

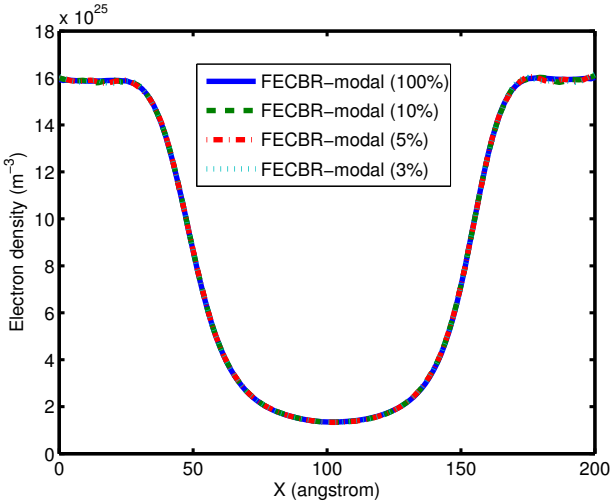

Figure 5.17: Electron density along the x-direction at y = 3.5 nm.

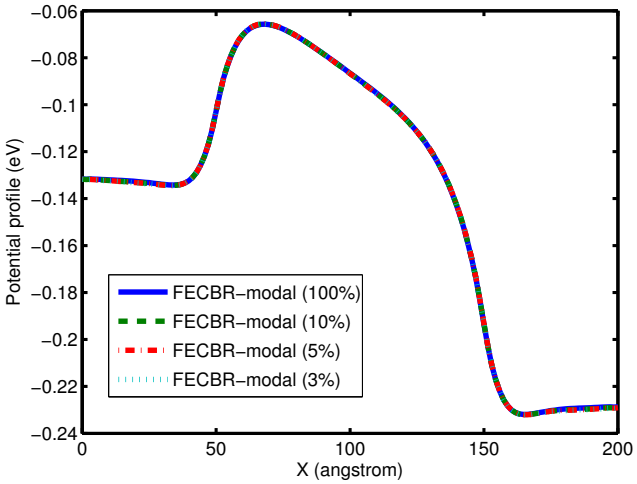

Figure 5.18: Potential profile along the x-direction at y = 3.5 nm.

Finally, the performance of accelerated FECBR-modal is examined by using a fine mesh with a large number of nodes. The domain is decomposed into 14 components as shown in Fig. 5.14 and 3% of the global eigen-pairs are retained in the calculation of the retarded Green's function. As shown in Fig. 5.19 and Fig. 5.20, the accelerated FECBR-modal (3%) provides accurate results compared to the original FECBR-modal approach. The potential profile in Fig. 5.19 is along the x-direction at $y = 3.5$ nm. Once the accuracy is ensured, the computational cost of the unaccelerated and accelerated FECBR-modal approaches are compared for different number of nodes (DOFs). Figure 5.21 shows the computational cost used to solve for the required eigen-pairs in the simulations. Figure 5.22 shows the total CPU time consumed for a single retarded Green's function/Poisson iteration. The computational cost reduction ratio of the accelerated FECBR-modal observed in this case is similar to that shown in Example 1. With a mesh of 53144 nodes, the accelerated FECBR-modal reduces the CPU time of computing the required eigen-pairs by 98% and the total computational cost per iteration by 90%.

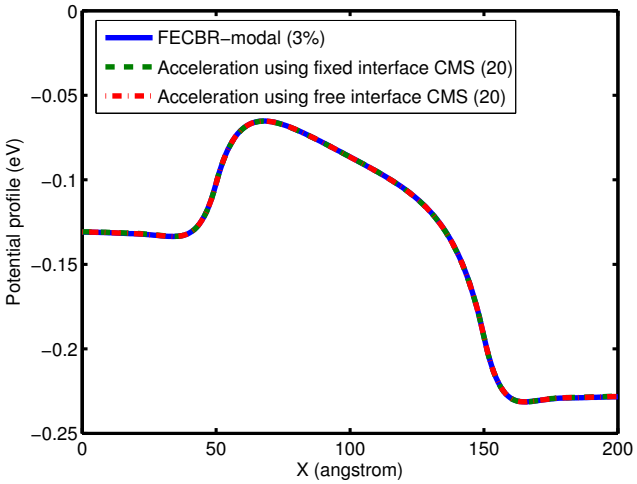

Figure 5.19: Potential profile in the x-direction at $y = 3.5$ nm.

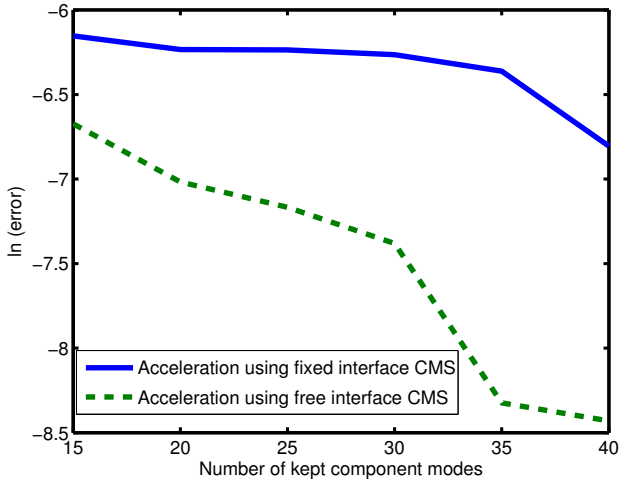

Figure 5.20: Variation of error in electron density with number of kept component modes.

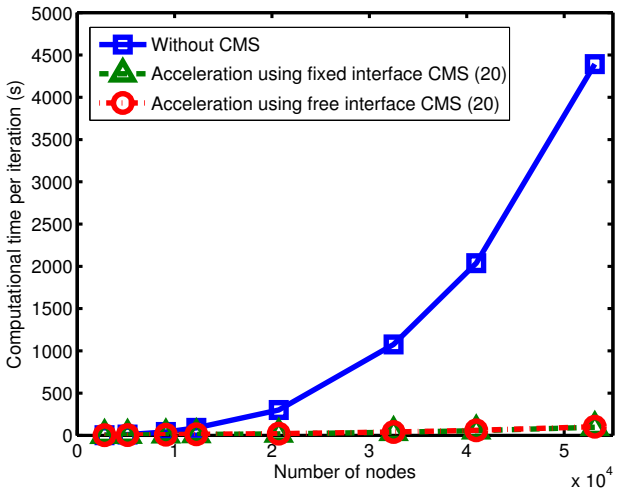

Figure 5.21: Computation cost for eigen-pairs calculation.

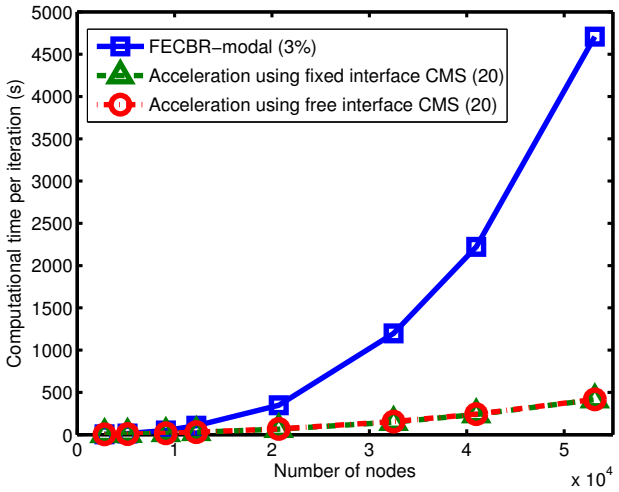

Figure 5.22: Total computation cost per Green's function/Poisson iteration.

5.4 Summary

In this chapter, an accelerated Finite Element Contact Block Reduction (FECBR) approach is developed for computational analysis of ballistic transport in electronic devices. The FECBR approach enables the simulation of electronic devices with irregular geometry using unstructured meshes. The enhanced

computational efficiency of the accelerated FECBR is achieved through three levels of model reduction and acceleration: (1) neglecting the decaying modes in the lead mode space; (2) neglecting high energy eigen-pairs in the closed-system; and (3) employing component mode synthesis techniques in solving for the closed-system eigen-pairs. By using the accelerated FECBR approach, the electrical transport properties of a DG-MOSFET with taper-shaped lead extensions are computed. In addition, the effect of Si/SiO_2 interface roughness on the electrical transport properties of a DG-MOSFET is investigated. The performance of the accelerated FECBR approach is studied for both cases. Our results show that the accelerated FECBR approach provides accurate results with a computational cost orders of magnitude less than that of the direct inversion method. It is demonstrated that the accelerated FECBR method is suitable for computational analysis of nanoscale electronic devices with irregular geometry and very large degrees of freedom.

CHAPTER 6

CONCLUSIONS

In this thesis, the electrostatic and electrical transport analysis in nanomaterials and devices is presented, the performance of currently available models are improved by new proposed algorithms. New numerical models are developed to simulate newly emerged physics in materials with quantum effects, such as the $Si/Si_{1-x}Ge_x$ nanocomposite thin films with mechanical strains and thermoelectric performance of nanoporous Si. Moreover, noval models with better computational performance are developed to investigate device physics in modern nanoscale semiconductor devices, such as DG-MOSFETs, nanowires, FinFETs, etc.

To speed up the electrostatic analysis in contemporary nanoscale structures and devices with arbitrary geometries, two component mode synthesis (CMS) approaches, namely, the fixed interface CMS approach and the free interface CMS approach, are presented and compared for an efficient self-consistent solution of $2D$ Schrödinger-Poisson equations. Numerical calculations show that both CMS approaches can largely reduce the computational cost. The free interface CMS approach can provide significantly more accurate results than the fixed interface CMS approach with the same number of retained wave functions in each component.

However, the fixed interface CMS approach is more efficient than the free interface CMS approach when large degrees of freedom are included in the simulation.

When an external voltage is applied to a nanoscale system, the charge carriers start to transport due to the non-equilibrium state caused by the external perturbations. By developing a numerical electrical transport model based on NEGF, the effect of various externally applied strains on the electrical conductivity of $Si/Si_{1-x}Ge_x$ nanocomposite thin films is studied. A degenerate two-band $k \cdot p$ theory is utilized to calculate the variation of the electronic band structure in the semiconductor nanocomposite thin films as a function of externally applied strains. The strain-dependent electrical conductivity of the material is computed by using a two dimensional NEGF-Poisson model. Numerical results demonstrate that the external strains have a significant influence on the electrical conductivity of the nanocomposite thin films. We show that the electrical conductivity variation can be attributed to combined effects of strain-induced splitting of the conduction band edges and change of band offset, electron quantum confinement, and size of the inclusion material in the thin films.

The non-equilibrium state of a system can be also caused by a temperature difference, by making use of the Seebeck effect, energy conversion between thermal domain and electrical domain can be realized. A numerical model is developed to study the thermoelectric properties of nanoporous silicon. The computational approach combines NEGF-Poisson for electrical transport analysis, a phonon BTE for phonon thermal transport analysis and the Wiedemann-Franz law for calculating the electronic thermal conductivity. The effects of doping density, porosity, temperature and nanopore size on thermoelectric properties of nanoporous silicon are investigated. It is confirmed that nanoporous silicon has significantly higher thermoelectric energy conversion efficiency than its nonporous counterpart.

Specifically, this chapter shows that, with a n-type doping density of $10^{20}cm^{-3}$, a porosity of 36% and nanopore size of $3nm \times 3nm$, the figure of merit ZT can reach 0.28 at $600K$. The results also show that the degradation of electrical conductivity of nanoporous Si due to the inclusion of nanopores is compensated by the large reduction in the phonon thermal conductivity and increase of absolute value of the Seebeck coefficient, resulting in a significantly improved ZT.

As the size of the problem increases, the computation becomes intractable on a single PC with the conventional models for electrical transport analysis, therefore, an accelerated FECBR method coupled with Poisson equation self-consistently is developed to analyze the ballistic transport in nanoscale electronic devices. The results show that, when very large DOFs is included, the efficiency of CBR is largely degraded due to the computational cost consumed by solving for the required eigen-pairs, nevertheless, the accelerated FECBR model can save computational cost significantly. By analyzing ballistic transport analysis in taper-shaped DG-MOSFETs and the effect of interface roughness on the electrical transport properties of DG-MOSFETs, both efficiency and accuracy of the accelerated FECBR are demonstrated. As a result, the accelerated FECBR model could be considered as an efficient algorithm to analyze and simulate ballistic transport in nanoscale devices with arbitrary geometry and large number of DOFs.

BIBLIOGRAPHY

[1] K. L. Ekinci and M. L. Roukes. Nanoelectromechanical systems. *Review of Scientific Instruments*, 76(6), 2005.

[2] Gang Li and N. R. Aluru. Hybrid techniques for electrostatic analysis of nanoelectromechanical systems. *Journal of Applied Physics*, 96(4):2221–2231, 2004.

[3] Yang Xu and N. R. Aluru. Multiscale electrostatic analysis of silicon nanoelectromechanical systems (NEMS) via heterogeneous quantum models. *Phys. Rev. B*, 77:075313, 2008.

[4] J. O. Island, V. Tayari, A. C. McRae, and A. R. Champagne. Few-hundred GHz carbon nanotube nanoelectromechanical systems (NEMS). *Nano Letters*, 12(9):4564–4569, 2012.

[5] H. Khan, D. Mamaluy, and D. Vasileska. Fully 3D self-consistent quantum transport simulation of double-gate and tri-gate 10 nm FinFETs. *Journal of Computational Electronics*, 7(3):346–349, 2008.

[6] Jing Wang, Eric Polizzi, and Mark Lundstrom. A three-dimensional quantum simulation of silicon nanowire transistors with the effective-mass approximation. *Journal of Applied Physics*, 96(4):2192–2203, 2004.

[7] M.H. Lee, S.T. Chang, J.-J. Huang, G.-R. Hu, Y.-S. Huang, and C. C Lee. Analysis and modeling of nano-crystalline silicon TFTs on flexible substrate with mechanical strain. In *Nanoelectronics Conference (INEC), 2010 3rd International*, pages 654–655, 2010.

[8] D. Georgiou, A. Laskarakis, C. Koidis, N. Goktsis, and S. Logothetidis. Growth mechanisms of silicon oxide nano-layers grown onto polymeric substrates for flexible electronics applications. *physica status solidi (c)*, 5(10):3387–3391, 2008.

[9] Chandan Bera, M. Soulier, C. Navone, Guilhem Roux, J. Simon, S. Volz, and Natalio Mingo. Thermoelectric properties of nanostructured $Si_{1-x}Ge_x$ and potential for further improvement. *Journal of Applied Physics*, 108(12), 2010.

[10] A. I. Boukai, Y. Bunimovich, J. Tahir-Kheli, and J. K. Yu. Silicon nanowires as efficient thermoelectric materials. *Nature*, 451:168–171, 2008.

[11] L. Tsakalakos, J. Balch, J. Fronheiser, B. A. Korevaar, O. Sulima, and J. Rand. Silicon nanowire solar cells. *Applied Physics Letters*, 91(23), 2007.

[12] B.J. Landi, S.L. Castro, H.J. Ruf, C.M. Evans, S.G. Bailey, and R.P. Raffaelle. CdSe quantum dot-single wall carbon nanotube complexes for polymeric solar cells. *Solar Energy Materials and Solar Cells*, 87(14):733 – 746, 2005.

[13] Massimiliano Di Ventra James E. Hughes Jr and Stephane Evoy. *Introduction to Nanoscale Science and Technology*. Springer, Berlin, 2004.

[14] D.J. Frank, R.H. Dennard, E. Nowak, P.M. Solomon, Yuan Taur, and Hen-Sum Philip Wong. Device scaling limits of Si MOSFETs and their application dependencies. *Proceedings of the IEEE*, 89(3):259–288, 2001.

[15] W. Haensch, E.J. Nowak, R.H. Dennard, P.M. Solomon, A. Bryant, O.H. Dokumaci, A. Kumar, X. Wang, J.B. Johnson, and M.V. Fischetti. Silicon CMOS devices beyond scaling. *IBM Journal of Research and Development*, 50(4.5):339–361, 2006.

[16] G.E. Moore. Progress in digital integrated electronics. In *Electron Devices Meeting, 1975 International*, volume 21, pages 11–13, 1975.

[17] Tejas Krishnamohan, Z. Krivokapic, K. Uchida, Yoshio Nishi, and K.C. Saraswat. High-mobility ultrathin strained Ge MOSFETs on bulk and SOI with low band-to-band tunneling leakage: experiments. *Electron Devices, IEEE Transactions on*, 53(5):990–999, 2006.

[18] Jing Guo, Supriyo Datta, M.P. Anantram, and Mark Lundstrom. Atomistic simulation of carbon nanotube field-effect transistors using Non-Equilibrium Green′s Function formalism. *Journal of Computational Electronics*, 3(3-4):373–377, 2004.

[19] G. Mahan, B. Sales, and J. Sharp. Thermoelectric materials: New approaches to an old problem. *Physics Today*, 50(3):42–47, 1997.

[20] F. J. DiSalvo. Thermoelectric cooling and power generation. *Science*, 285(5428):703–706, 1999.

[21] L. E. Bell. Cooling, heating, generating power, and recovering waste heat with thermoelectric systems. *Science*, 321(5895):1457–1461, 2008.

[22] G. Chen, M. S. Dresselhaus, G. Dresselhaus, J. P. Fleurial, and T. Caillat. Recent developments in thermoelectric materials. *International Materials Reviews*, 48(1):45–66, 2003.

[23] J. R. Szczech, J. M. Higgins, and S Jin. Enhancement of the thermoelectric properties in nanoscale and nanostructured materials. *J. Mater. Chem.*, 21:4037–4055, 2011.

[24] R. Venkatasubramanian, E. Siivola, T. Colpitts, and B. O'Quinn. Thin-film thermoelectric devices with high room-temperature figures of merit. *Nature*, 413:0028–0836, 2001.

[25] T. C. Harman, P. J. Taylor, M. P. Walsh, and B. E. LaForge. Quantum dot superlattice thermoelectric materials and devices. *Science*, 297(5590):2229–2232, 2002.

[26] Y. Hasegawa, Y. Murata, D. Nakamura, T. Komine, T. Taguchi, and S. Nakamura. Mobility estimation in microsized bismuth wire arrays. *Journal of Applied Physics*, 105(10):103715, 2009.

[27] Jin-Wu Jiang, Jian-Sheng Wang, and Baowen Li. A nonequilibrium Green′s function study of thermoelectric properties in single-walled carbon nanotubes. *Journal of Applied Physics*, 109(1), 2011.

[28] Yijian Ouyang and Jing Guo. A theoretical study on thermoelectric properties of graphene nanoribbons. *Applied Physics Letters*, 94(26), 2009.

[29] D. Vasileska, D. Mamaluy, H. R. Khan, K. Raleva, and S. M. Goodnick. Semiconductor device modeling. *Journal of Computational and Theoretical Nanoscience*, 5(6):999–1030, 2008.

[30] J. Su, P. Olivo, and B. Ricc. Self−consistent solution of the poisson and Schrödinger equations in accumulated semiconductor−insulator interfaces. *Journal of Applied Physics*, 70(1):337–345, 1991.

[31] IH. Tan, G. L. Snider, L. D. Chang, and E. L. Hu. A self−consistent solution of Schrödinger−Poisson equations using a nonuniform mesh. *Journal of Applied Physics*, 68(8):4071–4076, 1990.

[32] Thomas Kerkhoven, Albert T. Galick, Umberto Ravaioli, John H. Arends, and Youcef Saad. Efficient numerical simulation of electron states in quantum wires. *Journal of Applied Physics*, 68(7):3461–3469, 1990.

[33] A. Godoy, A. Ruiz-Gallardo, C. Sampedro, and F. Gmiz. Quantum-mechanical effects in multiple-gate mosfets. *Journal of Computational Electronics*, 6(1-3):145–148, 2007.

[34] F.M. Li, G.-W. Hsieh, and et al. Zinc oxide nanostructures and high electron mobility nanocomposite thin film transistors. *Electron Devices, IEEE Transactions on*, 55(11):3001–3011, 2008.

[35] M.S. Dresselhaus, G. Chen, M.Y. Tang, R.G. Yang, H. Lee, D.Z. Wang, Z.F. Ren, J.-P. Fleurial, and P. Gogna. New directions for low-dimensional thermoelectric materials. *Advanced Materials*, 19(8):1043–1053, 2007.

[36] Hao-Chih Yuan, M.M. Kelly, D.E. Savage, M.G. Lagally, George K. Celler, and Zhenqiang Ma. Thermally processed high-mobility mos thin-film transistors on transferable single-crystal elastically strain-sharing $Si/SiGe/Si$ nanomembranes. *Electron Devices, IEEE Transactions on*, 55(3):810–815, 2008.

[37] Jun Zhou, Xiaobo Li, Gang Chen, and Ronggui Yang. Semiclassical model for thermoelectric transport in nanocomposites. *Phys. Rev. B*, 82:115308, 2010.

[38] A. Popescu, L. M. Woods, J. Martin, and G. S. Nolas. Model of transport properties of thermoelectric nanocomposite materials. *Phys. Rev. B*, 79:205302, 2009.

[39] Y. Xu and G. Li. Strain effect analysis on phonon thermal conductivity of two-dimensional nanocomposites. *Journal of Applied Physics*, 106(11), 2009.

[40] R. Landauer. Electrical transport in open and closed systems. *Zeitschrift für Physik B Condensed Matter*, 68(2-3):217–228, 1987.

[41] M. Büttiker. Symmetry of electrical conduction. *IBM Journal of Research and Development*, 32(3):317, 1988.

[42] Craig S. Lent and David J. Kirkner. The quantum transmitting boundary method. *Journal of Applied Physics*, 67(10):6353–6359, 1990.

[43] J. N. Schulman and Yia-Chung Chang. Reduced hamiltonian method for solving the tight-binding model of interfaces. *Phys. Rev. B*, 27:2346–2354, 1983.

[44] S. E. Laux, A. Kumar, and M. V. Fischetti. Analysis of quantum ballistic electron transport in ultrasmall silicon devices including space-charge and geometric effects. *Journal of Applied Physics*, 95(10):5545–5582, 2004.

[45] D. Z. Y. Ting, E. T. Yu, and T. C. McGill. Multiband treatment of quantum transport in interband tunnel devices. *Phys. Rev. B*, 45:3583–3592, 1992.

[46] E. Polizzi, N. Ben Abdallah, O. Vanbsien, and D. Lippens. Space lateral transfer and negative differential conductance regimes in quantum waveguide junctions. *Journal of Applied Physics*, 87(12):8700–8706, 2000.

[47] Supriyo Datta. Nanoscale device modeling: the Green′s function method. *Superlattices and Microstructures*, 28(4):253 – 278, 2000.

[48] M. Büttiker. Four-terminal phase-coherent conductance. *Phys. Rev. Lett.*, 57:1761–1764, 1986.

[49] S. Datta. *Electronic Transport in Mesoscopic Systems*. Cambridge University Press, Cambridge, 1997.

[50] Eric Polizzi and Ahmed Sameh. Parallel algorithms for large-scale nanoelectronics simulations using NESSIE. *Journal of Computational Electronics*, 3(3-4):363–366, 2004.

[51] A. Svizhenko, M. P. Anantram, T. R. Govindan, B. Biegel, and R. Venugopal. Two-dimensional quantum mechanical modeling of nanotransistors. *Journal of Applied Physics*, 91(4):2343–2354, 2002.

[52] Zhibin Ren, R. Venugopal, S. Goasguen, Supriyo Datta, and M.S. LUNDSTROM. nanoMOS 2.5: A two-dimensional simulator for quantum transport in double-gate MOSFETs. *Electron Devices, IEEE Transactions on*, 50(9):1914–1925, 2003.

[53] Yasser M. Sabry, Tarek M. Abdolkader, and Wael F. Farouk. Simulation of quantum transport in double-gate MOSFETs using the non-equilibrium Green′s function formalism in real-space: A comparison of four methods. *International Journal of Numerical Modelling: Electronic Networks, Devices and Fields*, 24(4):322–334, 2011.

[54] D. Mamaluy, D. Vasileska, M. Sabathil, T. Zibold, and P. Vogl. Contact block reduction method for ballistic transport and carrier densities of open nanostructures. *Phys. Rev. B*, 71:245321, 2005.

[55] K. Uchida, Tejas Krishnamohan, K.C. Saraswat, and Yoshio Nishi. Physical mechanisms of electron mobility enhancement in uniaxial stressed MOSFETs and impact of uniaxial stress engineering in ballistic regime. In *Electron Devices Meeting, 2005. IEDM Technical Digest. IEEE International*, pages 129–132, 2005.

[56] T. Maegawa, T. Yamauchi, T. Hara, H. Tsuchiya, and Matsuto Ogawa. Strain effects on electronic bandstructures in nanoscaled silicon: From bulk to nanowire. *Electron Devices, IEEE Transactions on*, 56(4):553–559, 2009.

[57] L. T. Canham, W. Y. Leong, M. I. J. Beale, T. I. Cox, and L. Taylor. Efficient visible electroluminescence from highly porous silicon under cathodic bias. *Applied Physics Letters*, 61(21):2563–2565, 1992.

[58] A. J. Minnich, M. S. Dresselhaus, Z. F. Ren, and G. Chen. Bulk nanostructured thermoelectric materials: current research and future prospects. *Energy & Environmental Science*, 2:466–479, 2009.

[59] H.-S.P. Wong, D.J. Frank, and P.M. Solomon. Device design considerations for double-gate, ground-plane, and single-gated ultra-thin SOI MOSFET's at the 25 nm channel length generation. In *Electron Devices Meeting, 1998. IEDM '98. Technical Digest., International*, pages 407–410, 1998.

[60] Y. Omura, K. Kurihara, Y. Takahashi, T. Ishiyama, Y. Nakajima, and K. Izumi. 50-nm channel nMOSFET/SIMOX with an ultrathin 2- or 6-nm thick silicon layer and their significant features of operations. *Electron Device Letters, IEEE*, 18(5):190–193, 1997.

[61] Jong-Tae Park and J. Colinge. Multiple-gate SOI MOSFETs: device design guidelines. *Electron Devices, IEEE Transactions on*, 49(12):2222–2229, 2002.

[62] Sayed Hasan, Jing Wang, and Mark Lundstrom. Device design and manufacturing issues for 10 nm-scale MOSFETs: a computational study. *Solid-State Electronics*, 48(6):867 – 875, 2004.

[63] J.A. López-Villanueva, I. Melchor, F. Gmiz, J. Banqueri, and J.A. Jimnez-Tejada. A model for the quantized accumulation layer in metal-insulator-semiconductor structures. *Solid-State Electronics*, 38(1):203 – 210, 1995.

[64] Yasuyuki Ohkura. Quantum effects in Si n-MOS inversion layer at high substrate concentration. *Solid-State Electronics*, 33(12):1581 – 1585, 1990.

[65] Tomasz Janik and B. Majkusiak. Analysis of the MOS transistor based on the self-consistent solution to the Schrödinger and Poisson equations and on the local mobility model. *Electron Devices, IEEE Transactions on*, 45(6):1263–1271, 1998.

[66] Zhi Tang, Yang Xu, Gang Li, and N. R. Aluru. Physical models for coupled electromechanical analysis of silicon nanoelectromechanical systems. *Journal of Applied Physics*, 97(11), 2005.

[67] U. Ravaioli, B. Winstead, C. Wordelman, and A. Kepkep. Monte Carlo simulation for ultra-small MOS devices. *Superlattices and Microstructures*, 27(23):137 – 145, 2000.

[68] Frank Stern. Self-consistent results for n-type Si inversion layers. *Phys. Rev. B*, 5:4891–4899, 1972.

[69] A. Trellakis, A. T. Galick, A. Pacelli, and U. Ravaioli. Iteration scheme for the solution of the two-dimensional Schrödinger-Poisson equations in quantum structures. *Journal of Applied Physics*, 81(12):7880–7884, 1997.

[70] A. Trellakis and U. Ravaioli. Computational issues in the simulation of semiconductor quantum wires. *Computer Methods in Applied Mechanics and Engineering*, 181(4):437 – 449, 2000.

[71] F.J.G. Ruiz, A. Godoy, F. Gamiz, C. Sampedro, and L. Donetti. A comprehensive study of the corner effects in Pi-Gate MOSFETs including quantum effects. *Electron Devices, IEEE Transactions on*, 54(12):3369–3377, 2007.

[72] Jean-Pierre Colinge. Quantum-wire effects in trigate SOI MOSFETs. *Solid-State Electronics*, 51(9):1153 – 1160, 2007.

[73] F.J.G. Ruiz, I.M. Tienda-Luna, A. Godoy, L. Donetti, and F. Gamiz. Equivalent oxide thickness of trigate SOI MOSFETs with high-k insulators. *Electron Devices, IEEE Transactions on*, 56(11):2711–2719, 2009.

[74] Xiaohui Tang, X. Baie, J. Colinge, C. Gustin, and Vincent Bayot. Two-dimensional self-consistent simulation of a triangular p-channel SOI nano-flash memory device. *Electron Devices, IEEE Transactions on*, 49(8):1420–1426, 2002.

[75] J. Colinge, J.C. Alderman, Weize Xiong, and C.R. Cleavelin. Quantum-mechanical effects in trigate SOI MOSFETs. *Electron Devices, IEEE Transactions on*, 53(5):1131–1136, 2006.

[76] Mincheol Shin. Three-dimensional quantum simulation of multigate nanowire field effect transistors. *Mathematics and Computers in Simulation*, 79(4):1060 – 1070, 2008.

[77] R Craig and M Bampton. Coupling of substructures for dynamic analysis. *AIAA Journal*, 6(7):1313, 1968.

[78] KyungWon Min, Takeru Igusa, and Jan D. Achenbach. Frequency window method for forced vibration of structures with connected substructures. *The Journal of the Acoustical Society of America*, 92(5):2726–2733, 1992.

[79] Wen-Hwa Shyu, Jianmin Gu, Gregory M. Hulbert, and Zheng-Dong Ma. On the use of multiple quasi-static mode compensation sets for component mode synthesis of complex structures. *Finite Elements in Analysis and Design*, 35(2):119 – 140, 2000.

[80] Wen-Hwa Shyu, Zheng-Dong Ma, and Gregory M. Hulbert. A new component mode synthesis method: Quasi-static mode compensation. *Finite Elements in Analysis and Design*, 24(4):271 – 281, 1997.

[81] Damijan Markovic, K. C. Park, and Adnan Ibrahimbegovic. Reduction of substructural interface degrees of freedom in flexibility-based component mode synthesis. *International Journal for Numerical Methods in Engineering*, 70(2):163–180, 2007.

[82] R. CRAIG and C.-J. CHANG. Free-interface methods of substructure coupling for dynamic analysis. *AIAA Journal*, 14(11):1633–1635, 1976.

[83] Michel A. Tournour, Noureddine Atalla, Olivier Chiello, and Franck Sgard. Validation, performance, convergence and application of free interface component mode synthesis. *Computers and Structures*, 79(2021):1861 – 1876, 2001.

[84] P Koutsovasilis and M Beitelschmidt. Model order reduction of finite element models: improved component mode synthesis. *Mathematical and Computer Modelling of Dynamical Systems*, 16(1):57–73, 2010.

[85] R-R Craig and A-J Kurdila. *Fundamentals of Structural Dynamics*. John Wiley and Sons, New york, 2006.

[86] R.R. Craig. Coupling of substructures for dynamic analysis: an overview. In *In: Structures, Structural Dynamics and Material Conference, AIAA*, page 1573, 2000.

[87] Daniel J. Rixen. A dual craigbampton method for dynamic substructuring. *Journal of Computational and Applied Mathematics*, 168(12):383 – 391, 2004.

[88] G. Li. A multilevel component mode synthesis approach for the calculation of the phonon density of states of nanocomposite structures. *Computational Mechanics*, 42(4):593–606, 2008.

[89] N. R. Aluru and Gang Li. Finite cloud method: a true meshless technique based on a fixed reproducing kernel approximation. *International Journal for Numerical Methods in Engineering*, 50(10):2373–2410, 2001.

[90] Y. Ezzahri, G. Zeng, K. Fukutani, Z. Bian, and A. Shakouri. A comparison of thin film microrefrigerators based on Si/SiGe superlattice and bulk SiGe. *Microelectronics Journal*, 39(7):981 – 991, 2008.

[91] X. W. Wang, H. Lee, Y. C. Lan, G. H. Zhu, G. Joshi, D. Z. Wang, J. Yang, A. J. Muto, M. Y. Tang, J. Klatsky, S. Song, M. S. Dresselhaus, G. Chen, and Z. F. Ren. Enhanced thermoelectric figure of merit in nanostructured n-type silicon germanium bulk alloy. *Applied Physics Letters*, 93(19), 2008.

[92] B. Zhang, J. He, X. Ji, Terry M. Tritt, and Amar Kumbhar. Controlled two-dimensional coated nanostructures for bulk thermoelectric composites. *Applied Physics Letters*, 89(16), 2006.

[93] Shin ichi Takagi, T. Mizuno, T. Tezuka, N. Sugiyama, S. Nakaharai, T. Numata, J. Koga, and K. Uchida. Sub-band structure engineering for advanced CMOS channels. *Solid-State Electronics*, 49(5):684 – 694, 2005.

[94] I. Lauer and D.A. Antoniadis. Enhancement of electron mobility in ultrathin-body silicon-on-insulator MOSFETs with uniaxial strain. *Electron Device Letters, IEEE*, 26(5):314–316, 2005.

[95] K. Uchida, R. Zednik, Ching-Huang Lu, H. Jagannathan, J. McVittie, Paul C. McIntyre, and Yoshio Nishi. Experimental study of biaxial and uniaxial strain effects on carrier mobility in bulk and ultrathin-body SOI MOSFETs. In *Electron Devices Meeting, 2004. IEDM Technical Digest. IEEE International*, pages 229–232, 2004.

[96] R. People and J. C. Bean. Band alignments of coherently strained Ge_xSi_{1-x}/Si heterostructures on <001> Ge_ySi_{1-y} substrates. *Applied Physics Letters*, 48(8):538–540, 1986.

[97] Shouting Huang and Li Yang. Strain engineering of band offsets in Si/Ge core-shell nanowires. *Applied Physics Letters*, 98(9), 2011.

[98] Chris G. Van de Walle. Band lineups and deformation potentials in the model-solid theory. *Phys. Rev. B*, 39:1871–1883, 1989.

[99] R. People. Indirect band gap and band alignment for coherently strained Si_xGe_{1-x} bulk alloys on germanium (001) substrates. *Phys. Rev. B*, 34:2508–2510, 1986.

[100] Lifeng Liu, G.S. Lee, and A.H. Marshak. Band discontinuities of Si/Ge heterostructures. *Solid-State Electronics*, 37(3):421 – 425, 1994.

[101] Ingrid M. Graz, Darryl P. J. Cotton, and Stphanie P. Lacour. Extended cyclic uniaxial loading of stretchable gold thin-films on elastomeric substrates. *Applied Physics Letters*, 94(7), 2009.

[102] Stergios Logothetidis. Flexible organic electronic devices: Materials, process and applications. *Materials Science and Engineering: B*, 152(13):96–104, 2008.

[103] Shelley A Scott and Max G Lagally. Elastically strain-sharing nanomembranes: flexible and transferable strained silicon and silicon-germanium alloys. *Journal of Physics D: Applied Physics*, 40(4):R75, 2007.

[104] I. Balslev. Influence of uniaxial stress on the indirect absorption edge in silicon and germanium. *Phys. Rev.*, 143:636–647, 1966.

[105] E. Ungersboeck, S. Dhar, G. Karlowatz, V. Sverdlov, H. Kosina, and S. Selberherr. The effect of general strain on the band structure and electron mobility of silicon. *Electron Devices, IEEE Transactions on*, 54(9):2183–2190, 2007.

[106] S. E. Thompson Y. Sun and T. Nishida. *Strain effect in semiconductors: Theory and Device Applications*. Springer Science + Business Media, Berlin, 2010.

[107] A. Bulusu and D.G. Walker. Quantum modeling of thermoelectric properties of $Si/Ge/Si$ superlattices. *Electron Devices, IEEE Transactions on*, 55(1):423–429, 2008.

[108] P. S. Damle, A. W. Ghosh, and S. Datta. Unified description of molecular conduction: from molecules to metallic wires. *Phys. Rev. B*, 64:201403, 2001.

[109] S. L. Rumyantsev M. E. Levinshtein and M. S. Shur. *Properties of Advanced semiconductor materials: GaN, ALN, InN, BN, SiC, SiGe*. John Wiley and Sons, New york, 2001.

[110] Th. Vogelsang and K. R. Hofmann. Electron transport in strained Si layers on $Si_{1-x}Ge_x$ substrates. *Applied Physics Letters*, 63(2):186–188, 1993.

[111] Chris G. Van de Walle and Richard M. Martin. Theoretical calculations of heterojunction discontinuities in the Si/Ge system. *Phys. Rev. B*, 34:5621–5634, 1986.

[112] M. V. Fischetti and S. E. Laux. Band structure, deformation potentials, and carrier mobility in strained Si, Ge, and SiGe alloys. *Journal of Applied Physics*, 80(4):2234–2252, 1996.

[113] R. Venugopal, Z. Ren, S. Datta, M. S. Lundstrom, and D. Jovanovic. Simulating quantum transport in nanoscale transistors: Real versus mode-space approaches. *Journal of Applied Physics*, 92(7):3730–3739, 2002.

[114] R. Venugopal, M. Paulsson, S. Goasguen, S. Datta, and M. S. Lundstrom. A simple quantum mechanical treatment of scattering in nanoscale transistors. *Journal of Applied Physics*, 93(9):5613–5625, 2003.

[115] D. Y. Chung, T. Hogan, P. Brazis, M. Rocci-Lane, C. R. Kannewurf, and et al. Csbi(4)te(6): A high-performance thermoelectric material for low-temperature applications alloy. *Science*, 287(5455):1024–1027, 2000.

[116] L. Shi, D. Yao, G. Zhang, and B. Li. Size dependent thermoelectric properties of silicon nanowires. *Applied Physics Letters*, 95(6):063102, 2009.

[117] A. J. Minnich, H. Lee, X. W. Wang, G. Joshi, M. S. Dresselhaus, Z. F. Ren, G. Chen, and D. Vashaee. Modeling study of thermoelectric $SiGe$ nanocomposites. *Physical Review B*, 80:155327, 2009.

[118] J. Tang, H. Wang, D. Lee, M. Fardy, Z. Huo, T. Russell, and P. Yang. Holey silicon as an efficient thermoelectric material. *Nano Letters*, 10(10):4279–4283, 2010.

[119] J. Lee, G. A. Galli, and J. C. Grossman. Nanoporous Si as an efficient thermoelectric material. *Nano Letters*, 8(11):3750–3754, 2008.

[120] M. Kazan, S. Pereira, J. Coutinho, M. R. Correia, and P. Masri. Role of optical phonon in Ge thermal conductivity. *Applied Physics Letters*, 92(21), 2008.

[121] R. Kim and M. S. Lundstrom. Computational study of the seebeck coefficient of one-dimensional composite nano-structures. *Journal of Applied Physics*, 110(3):034511, 2011.

[122] S. V. J. Narumanchi, J. Y. Murthy, and C. H. Amon. Boltzmann transport equation-based thermal modeling approaches for hotspots in microelectronics. *Heat and Mass Transfer*, 42:478–491, 2006.

[123] A. J. H. McGaughey and M. Kaviany. Erratum: Quantitative validation of the Boltzmann transport equation phonon thermal conductivity model under the single-mode relaxation time approximation. *Phys. Rev. B*, 79:189901, 2009.

[124] S. Li, H. Chu, and W. Yan. Numerical study of phonon radiative transfer in porous nanostructures. *International Journal of Heat and Mass Transfer*, 51(1516):3924 – 3931, 2008.

[125] A. Rahman and M. S. Lundstrom. A compact scattering model for the nanoscale double-gate MOSFET. *IEEE Transactions on, Electron Devices*, 49(3):481 – 489, 2002.

[126] H. Li, Y. Xu, Y. Xu, and G. Li. Strain effect analysis on the electrical conductivity of $Si/Si_{1-x}Ge_x$ nanocomposite thin films. *Solid-State Electronics*, 85(0):64 – 73, 2013.

[127] R. Yang and G. Chen. Thermal conductivity modeling of periodic two-dimensional nanocomposites. *Physical Review B*, 69:195316, 2004.

[128] A. Pattamatta and C. K. Madnia. Modeling heat transfer in $Bi_2Te_3 - Sb_2Te_3$ nanostructures. *International Journal of Heat and Mass Transfer*, 52:860–869, 2009.

[129] D. T. Morelli, J. P. Heremans, and G. A. Slack. Estimation of the isotope effect on the lattice thermal conductivity of group IV and group III-V semiconductors. *Phys. Rev. B*, 66:195304, 2002.

[130] M. Asen-Palmer and et al. Thermal conductivity of germanium crystals with different isotopic compositions. *Phys. Rev. B*, 56:9431–9447, 1997.

[131] M. Kazan, G. Guisbiers, S. Pereira, M. R. Correia, P. Masri, A. Bruyant, S. Volz, and P. Royer. Thermal conductivity of silicon bulk and nanowires: Effects of isotopic composition, phonon confinement, and surface roughness. *Journal of Applied Physics*, 107(8), 2010.

[132] Glen A. Slack and S. Galginaitis. Thermal conductivity and phonon scattering by magnetic impurities in CdTe. *Phys. Rev.*, 133:A253–A268, 1964.

[133] P. G. Klemens. The scattering of low-frequency lattice waves by static imperfections. *Proceedings of the Physical Society. Section A*, 68(12):1113, 1955.

[134] M. Asheghi, K. Kurabayashi, R. Kasnavi, and K. E. Goodson. Thermal conduction in doped single-crystal silicon films. *Journal of Applied Physics*, 91(8):5079–5088, 2002.

[135] K. Suzuki and N. Mikoshiba. Effects of uniaxial stress and magnetic field on the low-temperature thermal conductivity of p-type Ge and Si. *Journal of the Physical Society of Japan*, 31(1):44–53, 1971.

[136] R. Berman. *Thermal conduction in solids*. Oxford studies in physics. Clarendon Press, 1976.

[137] J. M. Ziman. The effect of free electrons on lattice conduction. *Philosophical Magazine*, 1:191, 1955.

[138] J.M. Ziman. *Electrons and Phonons: The Theory of Transport Phenomena in Solids*. Oxford Classic Texts in the Physical Sciences. Clarendon Press, 2001.

[139] M. G. Holland. Analysis of lattice thermal conductivity. *Physical Review*, 132:2461–2471, 1963.

[140] H. Zhao, Z. Tang, G. Li, and N. R. Aluru. Quasiharmonic models for the calculation of thermodynamic properties of crystalline silicon under strain. *Journal of Applied Physics*, 99(6):064314, 2006.

[141] G. Chen. Size and interface effects on thermal conductivity of superlattices and periodic thin-film structures. *Journal of Heat Transfer*, 119(2):220–229, 1997.

[142] G. Chen. Thermal conductivity and ballistic-phonon transport in the cross-plane direction of superlattices. *Physical Review B*, 57:14958–14973, 1998.

[143] Alexander Balandin and Kang L. Wang. Significant decrease of the lattice thermal conductivity due to phonon confinement in a free-standing semiconductor quantum well. *Phys. Rev. B*, 58:1544–1549, 1998.

[144] Jie Zou and Alexander Balandin. Phonon heat conduction in a semiconductor nanowire. *Journal of Applied Physics*, 89(5):2932–2938, 2001.

[145] David Song and Gang Chen. Thermal conductivity of periodic microporous silicon films. *Applied Physics Letters*, 84(5):687–689, 2004.

[146] A. Majumdar. Microscale heat conduction in dielectric thin films. *Journal of Heat Transfer*, 115(1):7–16, 1993.

[147] Jing Wang, Eric Polizzi, Avik Ghosh, Supriyo Datta, and Mark Lundstrom. Theoretical investigation of surface roughness scattering in silicon nanowire transistors. *Applied Physics Letters*, 87(4), 2005.

[148] S. M. Sze. *Physics of Semiconductor Devices*. Wiley-Interscience publication. John Wiley & Sons, 1981.

[149] Z. Wang, S. Wang, S. Obukhov, N. Vast, J. Sjakste, V. Tyuterev, and N. Mingo. Thermoelectric transport properties of silicon: Toward an ab initio approach. *Physical Review B*, 83(20):1–5, 2011.

[150] N. D. Arora, J. R. Hauser, and D. J. Roulston. Electron and hole mobilities in silicon as a function of concentration and temperature. *IEEE Transactions on, Electron Devices*, 29(2):292–295, 1982.

[151] N. Neophytou, , and H. Kosina. On the interplay between electrical conductivity and seebeck coefficient in ultra-narrow silicon nanowires. *Journal of Electronic Materials*, 41(6):1305–1311, 2012.

[152] N Neophytou and H Kosina. Effects of confinement and orientation on the thermoelectric power factor of silicon nanowires. *Physical Review B*, 83:245305, 2011.

[153] W. Z. Shangguan, T. C. Au Yeung, Y. B. Yu, and C. H. Kam. Quantum transport in a one-dimensional quantum dot array. *Phys. Rev. B*, 63:235323, 2001.

[154] Stefan Rotter, Jian-Zhi Tang, Ludger Wirtz, Johannes Trost, and Joachim Burgdörfer. Modular recursive Green's function method for ballistic quantum transport. *Phys. Rev. B*, 62:1950–1960, 2000.

[155] Y. X. Liu, D. Z. Y. Ting, and T. C. McGill. Efficient, numerically stable multiband k·p treatment of quantum transport in semiconductor heterostructures. *Phys. Rev. B*, 54:5675–5683, 1996.

[156] E. Polizzi and N. Ben Abdallah. Self-consistent three-dimensional models for quantum ballistic transport in open systems. *Phys. Rev. B*, 66:245301, 2002.

[157] R. Venugopal, S. Goasguen, S. Datta, and M. S. Lundstrom. Quantum mechanical analysis of channel access geometry and series resistance in nanoscale transistors. *Journal of Applied Physics*, 95(1):292–305, 2004.

[158] Haiyan Jiang, Sihong Shao, Wei Cai, and Pingwen Zhang. Boundary treatments in non-equilibrium Greens function (NEGF) methods for quantum transport in nano-MOSFETs. *Journal of Computational Physics*, 227(13):6553 – 6573, 2008.

[159] Gerhard Klimeck, Roger Lake, R. Chris Bowen, William R. Frensley, and Ted S. Moise. Quantum device simulation with a generalized tunneling formula. *Applied Physics Letters*, 67(17):2539–2541, 1995.

[160] Marc Bescond, Jean-Luc Autran, Nicolas Cavassilas, Daniela Munteanu, and Michel Lannoo. Treatment of point defects in nanowire MOSFETs using the Nonequilibrium Green's function formalism. *Journal of Computational Electronics*, 3(3-4):393–396, 2004.

[161] Neophytos Neophytou, Shaikh Ahmed, and Gerhard Klimeck. Non-equilibrium Greens function (NEGF) simulation of metallic carbon nanotubes including vacancy defects. *Journal of Computational Electronics*, 6(1-3):317–320, 2007.

[162] D. Mamaluy, M. Sabathil, and P. Vogl. Efficient method for the calculation of ballistic quantum transport. *Journal of Applied Physics*, 93(8):4628–4633, 2003.

[163] H.R. Khan, D. Mamaluy, and D. Vasileska. Quantum transport simulation of experimentally fabricated nano-FinFET. *Electron Devices, IEEE Transactions on*, 54(4):784–796, 2007.

[164] Hao Wang, Gaofeng Wang, Sheng Chang, and Qijun Huang. High-order element effects of the Green's function in quantum transport simulation of nanoscale devices. *Electron Devices, IEEE Transactions on*, 56(12):3106–3114, 2009.

[165] Eric Polizzi and Supriyo Datta. Multidimensional nanoscale device modeling: the finite element method applied to the non-equilibrium Green's function formalism. In *Nanotechnology, 2003. IEEE-NANO 2003. 2003 Third IEEE Conference on*, volume 1, pages 40–43 vol.2, 2003.

[166] Matthias Sabathil. *opto-electronic and quantum transport properties of semiconductor nanostructures*. PhD thesis, Technische Universität München, September 2004.

[167] Stefan Birner, Christoph Schindler, Peter Greck, Matthias Sabathil, and Peter Vogl. Ballistic quantum transport using the contact block reduction (CBR) method. *Journal of Computational Electronics*, 8(3-4):267–286, 2009.

[168] H. Li and G. Li. Component mode synthesis approaches for quantum mechanical electrostatic analysis of nanoscale devices. *Journal of Computational Electronics*, 10(3):300–313, 2011.

[169] J.R. Watling, L. Yang, M. Borii, R.C.W. Wilkins, A. Asenov, J.R. Barker, and S. Roy. The impact of interface roughness scattering and degeneracy in relaxed and strained Si n-channel MOSFETs. *Solid-State Electronics*, 48(8):1337 – 1346, 2004.

[170] James Fonseca and Savas Kaya. Accurate treatment of interface roughness in nanoscale DG MOSFETs using non-equilibrium Green's functions. *Solid-State Electronics*, 48(1011):1843 – 1847, 2004.

[171] Eric I. Thorsos. The validity of the Kirchhoff approximation for rough surface scattering using a Gaussian roughness spectrum. *The Journal of the Acoustical Society of America*, 83(1):78–92, 1988.

[172] S. M. Goodnick, D. K. Ferry, C. W. Wilmsen, Z. Liliental, D. Fathy, and O. L. Krivanek. Surface roughness at the Si(100)-SiO_2 interface. *Phys. Rev. B*, 32:8171–8186, 1985.